January 2015

# Incorporation of Mission Design Constraints in Floquet Mode and Hamiltonian Structure-Preserving Orbital Maintenance Control Strategies for Libration Point Orbits

Kiarash Tajdaran
*Purdue University*

*Graduate School Form 30*
*Updated 1/15/2015*

**PURDUE UNIVERSITY**
**GRADUATE SCHOOL**
**Thesis/Dissertation Acceptance**

This is to certify that the thesis/dissertation prepared

By Kiarash Tajdaran

Entitled

Incorporation of Mission Design Constraints in Floquet Mode and Hamiltonian Structure-Preserving Orbital Maintenance Control Strategies for Libration Point Orbit

For the degree of Master of Science in Aeronautics and Astronautics

Is approved by the final examining committee:

Dr. Kathleen C. Howell
Co-chair

Dr. Martin Corless
Co-chair

Dr. James Longuski
Co-chair

To the best of my knowledge and as understood by the student in the Thesis/Dissertation Agreement, Publication Delay, and Certification Disclaimer (Graduate School Form 32), this thesis/dissertation adheres to the provisions of Purdue University's "Policy of Integrity in Research" and the use of copyright material.

Approved by Major Professor(s): Dr. Kathleen C. Howell

Approved by: Dr. Tom Shih 12/09/2015
Head of the Departmental Graduate Program Date

# INCORPORATION OF MISSION DESIGN CONSTRAINTS IN FLOQUET MODE AND HAMILTONIAN STRUCTURE-PRESERVING ORBITAL MAINTENANCE STRATEGIES FOR LIBRATION POINT ORBITS

A Thesis

Submitted to the Faculty

of

Purdue University

by

Kiarash Tajdaran

In Partial Fulfillment of the

Requirements for the Degree

of

Master of Science in Aeronautics and Astronautics

December 2015

Purdue University

West Lafayette, Indiana

"*We're made of star stuff. We are a way for the cosmos to know itself.*" – Carl Sagan

For my Parents

# ACKNOWLEDGEMENTS

For the unconditional love and support they have given me, I must first thank my family. Mom and dad, you have given up so much to make sure that I can pursue my dreams. You have always told that the sky's the limit for me and I can achieve anything through hard work and determination. Your faith in me and your support of my decisions are a source of inspiration, encouragement and love. To my twin brother, Kasra, I am very lucky that I had the chance to grow up with you. I have always looked up to you and learned from you. To my sister, Kiana, I love you and am so glad to have you in my life. Thank you so much for your love and encouragement.

My special thanks must go to my advisor, Professor Kathleen C. Howell. This research would not have been possible without your unconditional guidance, support, and patience. I am extremely thankful for giving me the opportunity to join your amazing research group and pursue my passion in the field of astrodynamics. Thank you for constantly challenging me and inspiring me to become a better researcher. I would also like to thank Professor Martin J. Corless and Professor James Longuski. I highly enjoyed learning from you, and I am grateful for your advice and guidance on this research.

Additionally, I'd like to express my gratitude to all the members of my research group. Thank you all for listening to my weekly presentations and providing me with feedbacks and suggestions. I have never met a more dedicated and talented group of people. It has been my privilege to work with each and every one of you. Lastly, I must thank Purdue Graduate School and the School of Aeronautics and Astronautics for providing me with funding to pursue my graduate studies here at Purdue University.

TABLE OF CONTENTS

Page

Page

# LIST OF TABLES

Table Page

Table Page

# LIST OF FIGURES

Figure Page



Appendix Figure

Appendix Figure Page

# ABSTRACT

Tajdaran, Kiarash. MSAA., Purdue University, December 2015. Incorporation of Mission Design Constraints in Floquet Mode and Hamiltonian Structure-Preserving Orbital Maintenance Strategies for Libration Point Orbits. Major Professor: Kathleen C. Howell.

Libration point orbits are, in general, inherently unstable. Without the presence of corrective maneuvers a spacecraft will diverge from the vicinity of such trajectories. In this research effort, two orbital maintenance control strategies are studied: the impulsive Floquet Mode (FM) controller and the continuous Hamiltonian Structure-Preserving (HSP) controller. These two controllers are further developed to incorporate real-world mission design constraints. The FM controller is modified to accommodate feasible maneuver directions that are constrained to a plane or a line. This controller is shown to be applicable for orbital station-keeping of spin stabilized spacecraft that are only equipped with either tangential thrusters or axial thrusters. The HSP controller is extended for application to general three-dimensional hyperbolic libration point orbits, and then discretized to account for the minimum time required for orbit determination and/or scientific operations. Both controllers are applied to an unstable $L_1$ halo orbit in the Sun-Earth/Moon system. The performances of these controllers are examined under the impacts of the spacecraft's operation errors and mission design constraints. Simulation results suggest that the FM controller is capable of maintaining the motion of the spacecraft in the vicinity of the desired reference trajectory for the duration of the simulation, while satisfying all mission design constraints. The discrete-time MHSP controller proves to be able to improve the stability of the nominal trajectory by reducing the value of the unstable Poincare exponent of the reference orbit.

# 1. INTRODUCTION

Libration point orbits in multi-body systems are increasingly being employed in space missions as they provide unique mission opportunities in a variety of space applications such as space weather, deep space observation platforms, and communication networks to facilitate missions in the solar system and beyond. Space missions around libration point orbits started with the launch of the third International Sun-Earth Explorer (ISEE–3) spacecraft in August 1978; one of the pioneers in studying solar winds and space weather. From November 1978 to June 1982, ISEE-3 completed 4 orbits around a quasi-periodic halo orbit in the vicinity of the Sun-Earth $L_1$ libration point. This accomplishment made ISEE-3 the first spacecraft to be stationed in a libration point orbit [1]. Since ISEE-3, other space missions such as SOHO [2], ACE [3], Genesis [4], and MAP [5] are successful examples of missions operated in the vicinity of libration point orbits. Scheduled to be launched within this decade is the James Webb Space Telescope (JWST), which will be stationed in the vicinity of the Sun-Earth $L_2$ libration point for the purpose of deep space observations [6].

Despite the broad range of applications for libration point orbits, these trajectories are, generally, unstable. Thus, an orbiting spacecraft diverges from its desired trajectory even under small perturbations. To incorporate libration point trajectories in space missions, orbital maintenance strategies must be developed to compute and execute corrective maneuvers with a high level of accuracy. In this research investigation, impulsive as well as continuous orbital maintenance strategies are studied that exploit the naturally existing dynamical structures inherent in multi-body regimes to maintain the motion of the spacecraft in the vicinity of the nominal trajectory. However, previously developed orbital maintenance strategies in these dynamical environments do not accommodate mission

constraints, such as feasible spacecraft maneuver directions, minimum thrust level, or orbital determination time constraints. In this investigation, orbital maintenance strategies are examined and further developed that incorporate and satisfy a variety of mission design constraints. Results from this research investigation offer a step forward in developing the next generation of spacecraft control systems to accommodate increasingly complex space missions.

## 1.1. Problem Definition

In the traditional mission designs a two-body problem was often adopted which considers motion of two gravitational, centrobaric bodies. This model results in the familiar conic sections of Keplerian motion. In the Two-Body Problem (2BP) the effects of the gravitational fields of any additional bodies are then added to the model as perturbations to the conic solutions.

A more general formulation of the problem is the Three-Body Problem (3BP) which incorporates the gravitational interaction of a third body. The 3BP, unlike the 2BP does not have an analytical solution for the differential equations governing the motion, however, the 3BP provides valuable insights into the qualitative nature of solutions in this system. In order to make the analysis of the 3BP more tractable, a number of simplifying assumptions are considered. The first assumption is that the gravitational effect of the third mass is negligible on the motion of the other two masses. For instance, in the case of Sun-planet-spacecraft system the gravitational effect of the spacecraft is negligible. This permits a two-body solution for the motion of the two primary bodies such as the Sun and the planet in the Sun-planet-spacecraft system. This reduced model is denoted as the Restricted Three-Body Problem (R3BP). The problem is further simplified by containing the two primary bodies to move in circular orbits about their center of mass. The resulting simplified model is labelled Circular Restricted Three-Body Problem (CR3BP), which still does not possess an analytical solution, but particular solutions can be determined.

The CR3BP has five equilibrium points denoted as the Lagrange or libration points which mark the locations in the plane of motion of the two primaries where all forces acting

on the infinitesimal third mass are balanced. Three of the libration points lie along the line connecting the two primary bodies, denoted as “collinear solutions”. The other two points form equilateral triangles with the two primary bodies in the primary plane of motion. The equilateral libration points are also denoted as “triangular solutions”. Moreover, the existence of libration points implies the existence of periodic and quasi-periodic solutions in the vicinity of libration points.

Libration point orbits create a variety of unique mission opportunities, however, the majority of these trajectories are categorized as unstable orbits, meaning that even small perturbations will cause the spacecraft to deviate from the “nominal” trajectory. Therefore, implementation of orbital station-keeping strategies that do not interfere with the scientific requirements and mission design constraints of the spacecraft is necessary. Numerous aspects of a mission design can directly influence the success of a station-keeping strategy. One important aspect is the sensitivity of scientific instruments on-board the spacecraft. Often corrective maneuvers can vitiate or interrupt the scientific measurements. Therefore, a suitable station-keeping strategy must be capable of handling the added constraint of a required minimum time between each maneuver, or a feasible maneuver direction to ensure the success of the science mission. Additionally, the propulsion system on-board a spacecraft has thresholds for maximum and minimum thrust levels. Orbital determination time constraints and the accuracy level of the obtained states are also important aspects of mission constraints, which should be taken into account when implementing a station-keeping strategy.

## 1.2. Pervious Contributions

### 1.2.1. A Brief History of Multibody Dynamics

The first formulation of the n-Body Problem was inspired by Sir Isaac Newton’s Universal Law of Gravitation published in his *Principia* in 1687 [7]. In his work, Newton derived a geometrical solution to the relative 2BP. Johann Bernoulli, in 1710, demonstrated that the solution to the 2BP is described by conic sections. Later in 1772, Leonhard Euler, a student of Bernoulli, introduced a rotating frame to the 3BP in an attempt to understand

the motion of the Moon in the Sun-Earth-Moon 3BP. Simultaneously, Josef Louis Lagrange derived an analytical solution to the restricted Sun-Jupiter 3BP that led to the identification of the five equilibrium points, known as the Lagrange or libration points [8].

Approximately fifty years later, in 1836, Carl Gustav Jacobi recognized a constant of integration associated with the rotating frame formulation of the 3BP, which was later named after him the Jacobi Constant [9]. In 1897, Heinrich Burns proved the non-existence of any other constant of integral in 3BP. Two years later, Jules Henri Poincare' also proved that the R3BP is not integrable by showing that an algebraic constant of integral does not exist in this problem [8]. However, further computational progress beyond this point was hindered for over half a century due to the lack of computing powers and high speed computers. Fortunately, with the technological advancements in the mid-1900s, extensive numerical investigations into the 3BP were made possible. In 1966, Victor G. Szebehely made a significant contribution to the 3BP by revisiting the derivation of the problem and providing details on the particular solutions with extensive numerical results. In light of the new technological advancements and the needed improvements in numerical methods over the past 50 years, research in Multi-Body Dynamics and its application in mission design has given rise to a new generation of research efforts.

### 1.2.2. Libration Point Orbits

In the early 1900's, before the advancements in high speed computers, Forest Moulton and Henry Plummer found analytical and numerical solutions for the two dimensional periodic orbits about the collinear libration points. In the 1960's, with the advent of high speed computing techniques, John Breakwell pioneered a new wave of investigations into motion in the vicinity of libtation points. Breakwell and his student Robert Farquhar, in the late 1960's, discovered the key concept for periodic out-of-plane trajectories in the vicinity of the Earth-Moon $L_2$ libration point. For the first time, Farquhar named these trajectories "halo" orbits. Later, Breakwell and Farquhar introduced higher order approximations to numerically produce halo orbits, and predicted the existence of natural

periodic solutions in the CR3BP. Ground breaking discoveries by Breakwell and Farquhar spurred new research efforts in the R3BP and its modern mission design applications [10].

### 1.2.3. Libration Point Orbit Station-Keeping

Libration point orbits are, in general, inherently unstable, which makes the implementation of a station-keeping strategy necessary to maintain the nominal trajectory. Breakwell and Farquhar et al examined the station-keeping issue of unstable halo orbits for the first time. In 1970's, they proposed the use of collinear libration point orbits for lunar communications in the Earth-Moon system, and they studied the associated station-keeping strategies and fuel costs [10]. Later, in 1980's Gomez [11] and Simo et al [12] exploited the Invariant Manifolds Theory and Floquet Modes to design an impulsive station-keeping control law to maintain motion relative to unstable libration point orbits. Howell and Pernika [13] developed the impulsive Target Point station-keeping control law, which was then further modified by Gordon [14]. Both strategies, Floquet Mode control law and Target Point control law, were compared by Keeter and Howell [15]. Moreover, in the early 2000's, Scheeres et al [16] proposed a continuous Hamiltonian-Structure Preserving (HSP) controller. This low thrust station-keeping strategy exploits the instantaneous stable and unstable manifolds of the trajectory to achieve local stability in the sense of Lyapunov. HSP control law was then extended for solar sail applications by M. Xu et al [17], and Soldini et al [18]. In her work, Soldini conducted a qualitative as well as quantitative comparison between the continuous HSP control law and the impulsive Floquet Mode control law. Soldini also extended the HSP control law to stabilize motion relative to planar libration orbits with complex and conjugate instantaneous eigenvalues. The HSP control law originally proposed by Scheeres could only control planar trajectories with instantaneous eigenvalues that are couples of real and pure imaginary.

## 1.3. Present Work

The main objective of this investigation is the incorporation of mission design constraints in orbital station-keeping strategies that utilize the natural dynamical structures

around a nominal trajectory. Specifically, two orbital station-keeping control laws, the impulsive Floquet Mode (FM) control law and the continuous Hamiltonian Structure-Preserving (HSP) control law, are examined and modified to incorporate real-world mission design constraints. Both of these controllers exploit the knowledge obtained from the invariant manifold theory regarding the phase space around libration point orbits, and implement corrective maneuvers that aim to maintain the spacecraft in the vicinity of a nominal libration point orbit. These controllers are then applied for station-keeping around an unstable libration point orbit in the Sun-Earth/Moon system and their performances are examined under the impacts of the spacecraft's operation errors and mission design constraints

This analysis is organized as follows:

- Chapter 2: Fundamental Background
  In this chapter, the equations of motion of a spacecraft in the CR3BP are derived. Libration points in the CR3BP are identified, and differential corrections algorithm to compute libration point orbits are developed. Lastly, invariant manifold theory and the characteristics of the phase space in the vicinity of libration point orbits are discussed.

- Chapter 3: Orbital Station-Keeping Simulation Algorithm
  Orbital station-keeping control problem and the goal that must be achieved by the control strategies are defined. Nominal libration point orbit, as well as mission design constraints and operation errors that are used in the simulation algorithm are introduced. In this investigation, the operation errors are simulated as random perturbations. Therefore, Monte Carlo simulation is conducted to take the average of the total station-keeping costs.

- Chapter 4: Impulsive Floquet Mode (FM) Station-Keeping Strategy
  Mathematical formulation for the FM control strategy is presented. This controller is then modified to incorporate feasible maneuver direction constraints. The

modified FM controller is applied for station-keeping of a spin-stabilized spacecraft equipped with only axial thrusters or tangential thrusters.

- Chapter 5: Continuous Hamiltonian Structure-Preserving (HSP) Station-Keeping Strategy

  Mathematical formulation for the HSP controller, originally developed by Shceeres [16], is presented. A list of limitations of this controller is compiled. The HSP controller is then modified to overcome the identified limitations. Lastly, the proposed modified controller is applied for station-keeping around the nominal orbit selected in chapter 3.

- Chapter 5: Summary and Recommendations

  The results of this research investigation are summarized, and potential future research areas are discussed.

# 2. FUNDAMENTAL BACKGROUND

The purpose of this chapter is to provide the ground base and fundamental background required to understand the formulation and analysis of the orbital station-keeping strategies presented in this research effort. This chapter begins with the formulation of the CR3BP: its assumptions, equations of motions, and particular solutions. Next, differential corrections algorithm and numerical techniques are introduced to compute baseline libration point orbits for station-keeping simulations. Finally, the invariant manifolds and the natural characteristics of the phase space around a liberation point orbit in the CR3BP are introduced.

## 2.1. The Circular Restricted Three-Body (CR3BP) Problem

The CR3BP governs the motion of a spacecraft under the gravitational influence of two larger primary bodies. While no close form, analytical solution has been found for this problem, the CR3BP provides valuable qualitative insights as well as numerical solutions for the spacecraft's trajectory under the gravitational attraction of the primary bodies and the external maneuver forces applied by thrusters on-board the spacecraft.

### 2.1.1. Assumptions

The general 3BP concerns three masses that are gravitationally interacting with each other. Figure 1 shows the three masses in the inertial frame. There are three simplifying assumptions to the 3BP that allows the CR3BP. First, the mass of the particle of interest $P_3$, that is $m_3$, is negligible compared to the two primary bodies $P_1$ and $P_2$, that is $m_1$ and $m_2$, respectively. This means that the motion of the spacecraft does not influence the motion

of either $P_1$ or $P_2$. Moreover, the two primaries represent a two-body system, hence the movement of $P_1$ and $P_2$ is planner. Lastly, $P_1$ and $P_2$ move in a circular orbit, with a constant angular velocity equal to the mean motion of the two primaries.

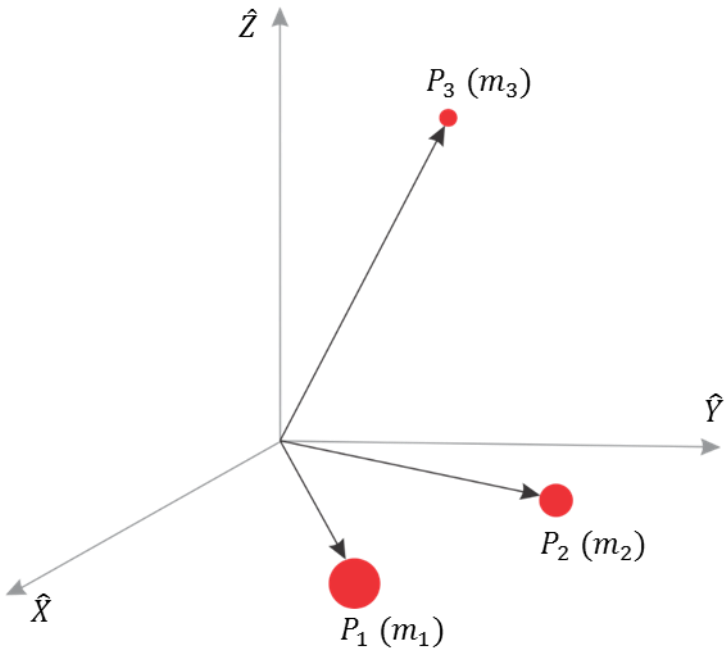


*Figure 2.1. General Three-Body Problem*

In this research effort, the dynamical system under investigation is the Sun-Earth/Moon system. In this system the larger primary ($P_1$) is the Sun, and the smaller primary ($P_2$) is the Earth-Moon barycenter.

### 2.1.2. Geometry

To formulate the mathematical expression for the motion of the spacecraft it is necessary to define two reference frames. The first reference frame is the inertially-fixed coordinate frame, *I*, located at the barycenter of the Sun and Earth/Moon system (*B*). This frame has unit vectors defined as $\hat{X} - \hat{Y} - \hat{Z}$, where the $\hat{Z}$ axis is parallel to the angular momentum vector of the two primaries. The second reference frame is the rotating frame, *R*, also located at *B*, with unit vectors $\hat{x} - \hat{y} - \hat{z}$. In this frame the $\hat{z}$ axis is also parallel to

the angular momentum vector of the primaries. The $\hat{x}$ axis connects the two primaries and is directed from the larger primary toward the smaller primary. The geometry of these two frames is illustrated in figure 2.2. The position of the spacecraft is described by vector $\vec{r}$, and the positions of the two primaries is defined by vectors $\vec{r}_1$ and $\vec{r}_2$, respectively. The relative position vectors $\vec{d}_1$ and $\vec{d}_2$ describe the position of the spacecraft relative to the two primaries $P_1$ and $P_2$, respectively. Moreover, the rotating frame is oriented relative to the inertial frame with angle $\theta$ which has an angular velocity $\omega$. This angular velocity is equivalent to the mean motion of the Sun-Earth/Moon system given by:

$$\omega = \sqrt{G(m_1 + m_2)/r_{12}^3} \tag{2.4}$$

Where G is the gravitational constant, and $r_{12} = r_1 + r_2$.

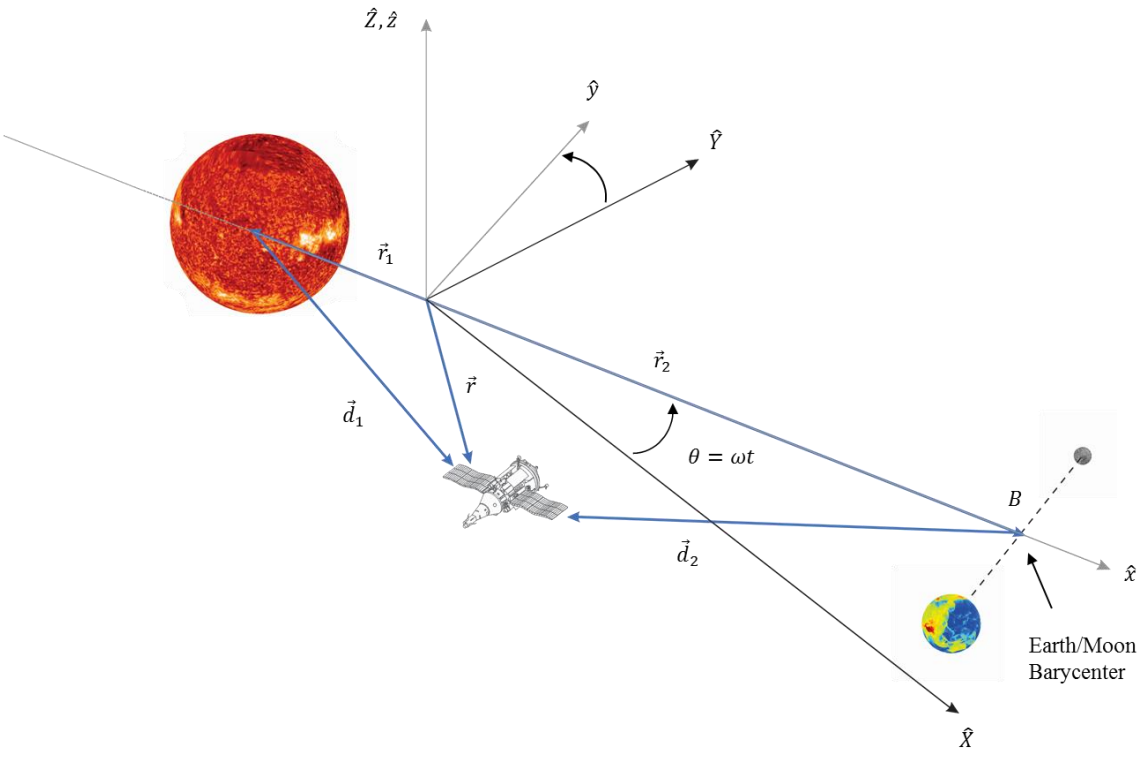


*Figure 2.2. Geometry of the Circular Restricted Three-Body Problem (CR3BP)*

### 2.1.3. Equations of Motion

The differential equations in the circular restricted three-body problem are the mathematical expressions describing the motion of the infinitesimal mass $P_3$ or the spacecraft. The most dominant forces acting on the spacecraft are the gravitational forces exerted from the two primaries. Given the Newton's Law of Gravity, these forces can be represented in the following form,

$$\vec{f}_1 = -\frac{Gm_1}{d_1^3}\vec{d}_1 \tag{2.2}$$

$$\vec{f}_2 = -\frac{Gm_2}{d_2^3}\vec{d}_2 \tag{2.3}$$

From Newton's Second Law, the general expression for motion of the spacecraft can be written as,

$$\ddot{\vec{r}} = {}^{I}\frac{d^2}{dt^2}\vec{r} = \sum \vec{f} = \vec{f}_1 + \vec{f}_2 = -\frac{Gm_1}{d_1^3}\vec{d}_1 - \frac{Gm_2}{d_2^3}\vec{d}_2 \tag{2.4}$$

To simplify and generalize the solution of this equation, it is useful to non-dimensionalize the system of equations by employing quantities that are characteristic of the system. The characteristic quantities are chosen based on the three most basic dimensions which are length, mass and time. The choice of these three parameters, will result in characteristic quantities that are either constant or would cause other values to become constant.

The characteristic length is defined to be the distance between the two primaries. This distance is constant as the primaries are in circular motion about their barycenter. Therefore the characteristic length is written as,

$$L^* = r_1 + r_2 \tag{2.5}$$

The characteristic mass is evaluated as the sum of the mass of the two primaries, that is,

$$M^* = m_1 + m_2 \tag{2.6}$$

Lastly, the characteristic time, $\tau^*$, is defined such that the non-dimensional gravitational constant, $\tilde{G}$, is unity. This is done by noting that $G$ has units of $km^3/kgs^2$. Therefore, the non-dimensional gravitational constant, $\tilde{G}$, should be,

$$\tilde{G} = 1 = \frac{GM^*\tau^{*2}}{L^{*3}} \tag{2.7}$$

This yields that the characteristic time is formulated as,

$$\tau^* = \sqrt{\frac{L^{*3}}{GM^*}} \tag{2.8}$$

From the choice of the characteristic mass, length and time, it also follows that the non-dimensional mean motion is equal to unity. Based on a conic definition, the dimensional mean motion is given by,

$$n = \sqrt{\frac{GM^*}{L^{*3}}} \tag{2.9}$$

Using the characteristic time, $\tau^*$, it follows that the non-dimensional mean motion, $N^*$, is written as,

$$N^* = n\tau^* = \sqrt{GM^*/L^{*3}}\,\tau^* = 1 \tag{2.10}$$

As a consequence of a unity non-dimensional mean motion, the non-dimensional orbital period associated with the motion of the two primaries about their barycenter is $2\pi$ in non-dimensional time units. By incorporating the characteristic quantities into equation (2.4), the non-dimensional equations of motion is written as follows,

$$\ddot{\vec{\rho}} = \frac{{}^{I}d^2}{d\tau^{*2}}\vec{\rho} = -\frac{(1-\mu)}{\overline{d_1}^3}\overrightarrow{d_1} - \frac{\mu}{\overline{d_2}^3}\overrightarrow{d_2} \tag{2.11}$$

Where $\vec{\rho} = \frac{\vec{r}}{L^*}$ is the non-dimensional position vector of the spacecraft, $\overline{d_1} = \frac{d1}{L^*}$, $\overline{d_2} = \frac{d2}{L^*}$, $\mu = \frac{m_2}{M^*}$, and $1 - \mu = \frac{m_1}{M^*}$.

Much insight into the motion of the spacecraft is obtained by expressing the vector equations of motion, given in (2.11), in the scalar form. The position vector of the spacecraft in terms of non-dimensional components in the rotating frame is given by,

$$\vec{\rho} = x\hat{x} + y\hat{y} + z\hat{z} \tag{2.12}$$

The acceleration of the spacecraft in non-dimensional units is derived using the basic kinematic equations, as the time derivative of the position vector is taken in the rotating frame R with respect to the inertial frame I. Hence, the velocity of the spacecraft in the rotating frame is obtained as follows,

$$\frac{{}^{I}d}{d\tau^*}\vec{\rho} = \frac{{}^{R}d}{d\tau^*}\vec{\rho} + {}^{I}\vec{\omega}^{R} \times \vec{\rho} \tag{2.13}$$

Where $\frac{{}^{I}d}{d\tau^*}$ is the derivative with respect to non-dimensional time $\tau^*$, as viewed by an inertial observer and expressed in terms of rotating frame coordinates. $\frac{{}^{R}d}{d\tau^*}$ is the time derivative as viewed by an observer in the rotating frame. ${}^{I}\vec{\omega}^{R}$ is the angular acceleration of the rotating frame with respect to the inertial frame and is given by,

$${}^{I}\vec{\omega}^{R} = N^*\hat{z} = \hat{z} \tag{2.14}$$

By substituting for $\vec{\rho}$ and ${}^{I}\vec{\omega}^{R}$ into equation (2.13), the velocity of the spacecraft expressed in the rotating frame with respect to an inertial observer is as follows,

$$ {}^{I}\frac{d}{dt}\,\vec{\rho} = \dot{\vec{\rho}} = (\dot{x} - y)\hat{x} + (\dot{y} - x)\hat{y} + (\dot{z})\hat{z} \tag{2.15} $$

Next, the kinematic expansion for the inertial acceleration is written as,

$$ {}^{I}\frac{d}{dt}\,\dot{\vec{\rho}} = {}^{R}\frac{d}{dt}\,\dot{\vec{\rho}} + {}^{I}\vec{\omega}^{R} \times \dot{\vec{\rho}} \tag{2.16} $$

By substituting for $\vec{\rho}$ and ${}^{I}\vec{\omega}^{R}$ into equation (2.15), the acceleration of the spacecraft expressed in the rotating frame with respect to an inertial observer is as follows,

$$ \ddot{\vec{\rho}} = (\ddot{x} - 2\dot{y} - x)\hat{x} + (\ddot{y} + 2\dot{x} - y)\hat{y} + \ddot{z}\hat{z} \tag{2.17} $$

Next, the non-dimensionalized positions of the primaries with respect to the barycenter are,

$$ \vec{\rho}_1 = \frac{\vec{r}_1}{L^*} = -\frac{m_2}{m_1 + m_2}\hat{x} = -\mu\hat{x} \tag{2.18} $$

$$ \vec{\rho}_2 = \frac{\vec{r}_2}{L^*} = \frac{m_1}{m_1 + m_2}\hat{x} = (1 - \mu)\hat{x} \tag{2.19} $$

Hence, the non-dimensionalized position vectors of the spacecraft with respect to the primary bodies are written as,

$$ \overrightarrow{\overrightarrow{d_1}} = \vec{\rho} - \vec{\rho}_1 = (x + \mu)\hat{x} + y\hat{y} + z\hat{z} \tag{2.20} $$

$$ \overrightarrow{\overrightarrow{d_2}} = \vec{\rho} - \vec{\rho}_2 = (x - (1 - \mu))\hat{x} + y\hat{y} + z\hat{z} \tag{2.21} $$

By substituting equations (2.17), (2.20), and (2.21) into equation (2.11), the scalar from of the second order differential equations of motion for an infinitesimal mass in the CR3BP is given by:

$$\ddot{x} - 2\dot{y} - x = -\frac{(1-\mu)(x+\mu)}{\overline{d_1}^3} - \frac{\mu\big(x-(1-\mu)\big)}{\overline{d_2}^3} \tag{2.22}$$

$$\ddot{y} + 2\dot{x} - y = -\frac{(1-\mu)y}{\overline{d_1}^3} - \frac{\mu y}{\overline{d_2}^3} \tag{2.23}$$

$$\ddot{z} = -\frac{(1-\mu)z}{\overline{d_1}^3} - \frac{\mu z}{\overline{d_2}^3} \tag{2.24}$$

Where $\overline{d_1} = \sqrt{(x+\mu)^2 + y^2 + z^2}$ and $\overline{d_2} = \sqrt{\big(x-(1-\mu)\big)^2 + y^2 + z^2}$.

A pseudo-potential function, $U^*$, is introduced that allows a more compact formulation of the equations of motion,

$$U^* = \frac{1-\mu}{\overline{d_1}} + \frac{\mu}{\overline{d_2}} + \frac{1}{2}(x^2 + y^2) \tag{2.25}$$

Therefore, the equations of motion given in (2.22), (2.23), and (2.23) can be written more concisely as,

$$\ddot{x} - 2\dot{y} = \frac{\partial U^*}{\partial x} \tag{2.26}$$

$$\ddot{y} + 2\dot{x} = \frac{\partial U^*}{\partial y} \tag{2.27}$$

$$\ddot{z} = \frac{\partial U^*}{\partial z} \tag{2.28}$$

Equations (2.26), (2.27), and (2.28) comprise the equations of motion of a spacecraft in the CR3BP described in terms of rotating coordinates relative to barycenter of the primary bodies. These equations do not possess a close form analytical solution, however particular solutions can be determined.

### 2.1.4. Libration Points

The libration points are the equilibrium solutions to the equations of motion given in (2.26)-(2.28). These are in fact the equilibrium points of the CR3BP within the context of the rotating reference frame. These libration points are invariant solutions to the equations of motion, as they will appear constant relative to the rotating reference frame. Therefore, at the libration points the velocity and acceleration of the spacecraft is zero. The following equations govern the locations of the equilibrium points in the CR3BP,

$$x_{eq} - \frac{(1-\mu)(x_{eq}+\mu)}{\overline{d_{1_{eq}}}^3} - \frac{\mu\left(x_{eq}-(1-\mu)\right)}{\overline{d_{2_{eu}}}^3} = 0 \tag{2.29}$$

$$y_{eq} - \frac{(1-\mu)y_{eq}}{\overline{d_{1_{eq}}}^3} - \frac{\mu y_{eq}}{\overline{d_{2_{eq}}}^3} = 0 \tag{2.30}$$

$$-\frac{(1-\mu)z_{eq}}{\overline{d_{1_{eq}}}^3} - \frac{\mu z_{eq}}{\overline{d_{2_{eq}}}^3} = 0 \tag{2.31}$$

Where $x_{eq}, y_{eq},$ and $z_{eq}$ correspond to the position coordinates of the equilibrium points. The solution to equation (2.31) is $z_{eq} = 0$, which indicates that all the equilibrium points lie in the plane of motion of the two primaries. By inspection, two sets of solutions exist for equation (2.30): $y_{eq} = 0$, and $y_{eq} = \pm\frac{\sqrt{3}}{2}$ (when $\overline{d_{1_{eq}}} = \overline{d_{2_{eq}}}$). These two sets of solutions correspond to the collinear libration points and the triangular libration points, respectively.

Starting with the collinear solution, by substituting $y_{eq} = z_{eq} = 0$ into equation (2.29), the following equation is produced which governs the solution for $x_{eq}$,

$$x_{eq} - \frac{(1-\mu)(x_{eq}+\mu)}{|x_{eq}+\mu|^3} - \frac{\mu\left(x_{eq}-(1-\mu)\right)}{|x_{eq}-1+\mu|^3} = 0 \tag{2.32}$$

This non-linear quintic equation possesses three real solutions, which can be solved iteratively using a Newton-Raphson's method. These three solutions are the three collinear libration points in the CR3BP, denoted as $L_1$, $L_2$, and $L_3$. By conviction, $L_1$ is located between the two primaries, $L_2$ is located to the right of $P_2$, and $L_3$ is located to the left of $P_1$.

The triangular libration points are found by setting $\overline{d_{1_{eq}}} = \overline{d_{2_{eq}}}$ in equation (2.29) and (2.30). The coordinates for these points are given by $x_{eq} = \frac{1}{2} - \mu$, and $y_{eq} = \pm\frac{\sqrt{3}}{2}$. These two point, which are conventionally named $L_4$ and $L_5$, form equilateral triangles with the two primaries. Figure 1.3 illustrates the locations of the libration points with respect to the primaries.

## 2.2. Computation of Periodic Halo Libration Point Orbits

In the CR3BP infinitely many periodic solutions exist. These periodic trajectories are important tools in understanding the dynamical environment since the equations of motion in the CR3BP do not possess a closed form analytical solution. Halo orbits are one type of periodic orbits which are of particular interest due to their three-dimensional and symmetric trajectories that can facilitate a variety of space applications such as space observatory and the Geostorm warning mission as well as space platforms for communication networks. In this study, halo orbits will be used as baseline trajectories for station-keeping.

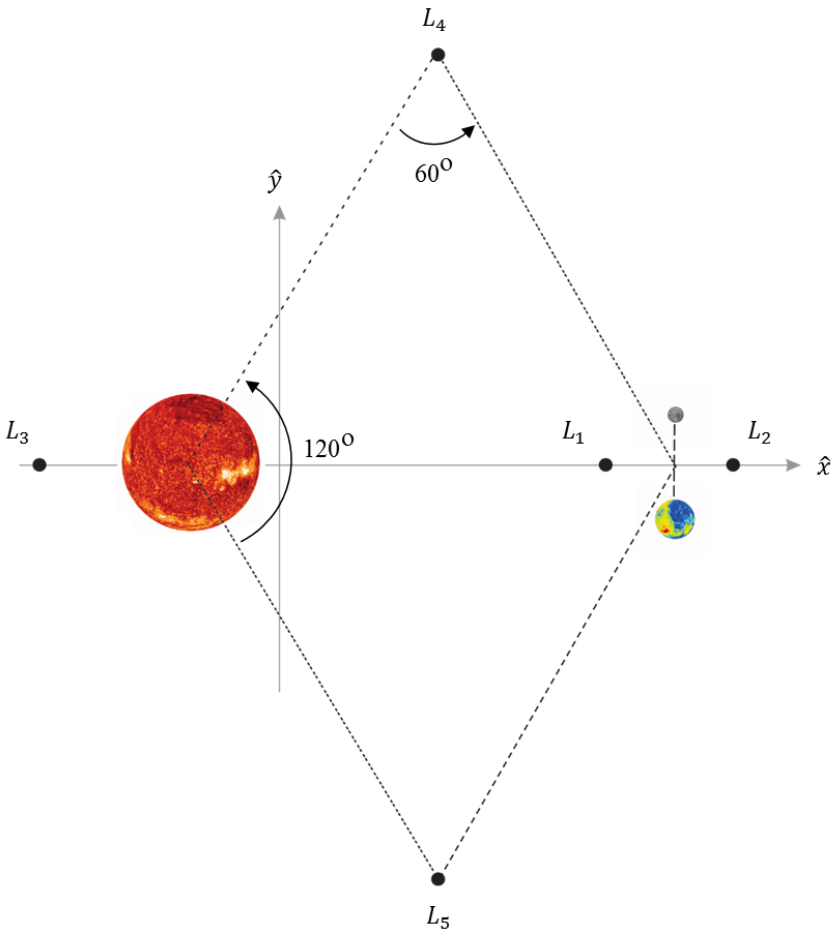


*Figure 2.3. Libration Points in the CR3BP*

There are many different methods available for computation of periodic halo orbits. The technique used in this work is based on a numerical targeting scheme which utilizes differential corrections. This algorithm was originally developed by Breakwell, and Brown [10], and was later expanded by Farquhar [23] and Howell [24].

### 2.2.1. Linearized Variational Equations of Motion

Targeting schemes are frequently based on the linearized variational equations relative to a reference trajectory in the non-linear system. A first order Taylor series approximation of the non-linear equations of motion (in (2.26)-(2.28)) about a reference trajectory results in the linear variational equations of motion as follows,

$$\delta\dot{\vec{X}}(t) = A(t)\delta\vec{X}(t) \tag{2.33}$$

Where $\delta\vec{X}(t) = \vec{X}(t) - \vec{X}_{ref}(t) = \left[\delta x\ \delta y\ \delta z\ \delta\dot{x}\ \delta\dot{y}\ \delta\dot{z}\right]^T$, denotes the state error vector relative to a reference trajectory $\vec{X}_{ref}(t)$. In this study, the reference trajectory is a periodic halo orbit. Therefore $A(t)$ is a time-varying matrix which is expressed as,

$$A(t) = \begin{bmatrix} 0 & 0 & 0 & 1 & 0 & 0 \\ 0 & 0 & 0 & 0 & 1 & 0 \\ 0 & 0 & 0 & 0 & 0 & 1 \\ U^*_{xx} & U^*_{xy} & U^*_{xz} & 0 & 2 & 0 \\ U^*_{yx} & U^*_{yy} & U^*_{yz} & -2 & 0 & 0 \\ U^*_{zx} & U^*_{zy} & U^*_{zz} & 0 & 0 & 0 \end{bmatrix} = \begin{bmatrix} 0 & I \\ U^*_{RR} & 2K \end{bmatrix} \tag{2.34}$$

Where $K = \begin{bmatrix} 0 & 1 & 0 \\ -1 & 0 & 0 \\ 0 & 0 & 0 \end{bmatrix}$, $U^*_{RR} = \begin{bmatrix} U^*_{xx} & U^*_{xy} & U^*{}_{xz} \\ U^*_{xy} & U^*_{yy} & U^*{}_{yz} \\ U^*_{xz} & U^*_{yz} & U^*_{zz} \end{bmatrix}$, and $U^*_{mn} = \frac{\partial}{\partial m}\left(\frac{\partial U^*(t)}{\partial n}\right)$.

The general solution to the linear variational equation in (2.33), is given by $\Phi(t, t_0)$, the State Transition Matrix (STM),

$$\delta\vec{X}(t) = \Phi(t, t_0)\ \delta\vec{X}(t_0) \tag{2.35}$$

Where $\Phi(t, t_0)$ has the following form,

$$\Phi(t, t_0) = \begin{bmatrix} \frac{\partial x(t)}{\partial x(t_0)} & \frac{\partial x(t)}{\partial y(t_0)} & \frac{\partial x(t)}{\partial z(t_0)} & \frac{\partial x(t)}{\partial \dot{x}(t_0)} & \frac{\partial x(t)}{\partial \dot{y}(t_0)} & \frac{\partial x(t)}{\partial \dot{z}(t_0)} \\ \frac{\partial x(t)}{\partial y(t_0)} & \frac{\partial x(t)}{\partial y(t_0)} & \frac{\partial x(t)}{\partial z(t_0)} & \frac{\partial x(t)}{\partial \dot{x}(t_0)} & \frac{\partial x(t)}{\partial \dot{y}(t_0)} & \frac{\partial x(t)}{\partial \dot{z}(t_0)} \\ \frac{\partial x(t)}{\partial z(t_0)} & \frac{\partial x(t)}{\partial y(t_0)} & \frac{\partial x(t)}{\partial z(t_0)} & \frac{\partial x(t)}{\partial \dot{x}(t_0)} & \frac{\partial x(t)}{\partial \dot{y}(t_0)} & \frac{\partial x(t)}{\partial \dot{z}(t_0)} \\ \frac{\partial \dot{x}(t)}{\partial x(t_0)} & \frac{\partial \dot{x}(t)}{\partial y(t_0)} & \frac{\partial \dot{x}(t)}{\partial z(t_0)} & \frac{\partial \dot{x}(t)}{\partial \dot{x}(t_0)} & \frac{\partial \dot{x}(t)}{\partial \dot{y}(t_0)} & \frac{\partial \dot{x}(t)}{\partial \dot{z}(t_0)} \\ \frac{\partial \dot{y}(t)}{\partial x(t_0)} & \frac{\partial \dot{y}(t)}{\partial y(t_0)} & \frac{\partial \dot{y}(t)}{\partial z(t_0)} & \frac{\partial \dot{y}(t)}{\partial \dot{x}(t_0)} & \frac{\partial \dot{y}(t)}{\partial \dot{y}(t_0)} & \frac{\partial \dot{y}(t)}{\partial \dot{z}(t_0)} \\ \frac{\partial \dot{z}(t)}{\partial x(t_0)} & \frac{\partial \dot{z}(t)}{\partial y(t_0)} & \frac{\partial \dot{z}(t)}{\partial z(t_0)} & \frac{\partial \dot{z}(t)}{\partial \dot{x}(t_0)} & \frac{\partial \dot{z}(t)}{\partial \dot{y}(t_0)} & \frac{\partial \dot{z}(t)}{\partial \dot{z}(t_0)} \end{bmatrix} \tag{2.36}$$

Evident from equation (2.35), STM offers a linear predication for the variation of the final state at time $t$, i.e. $\delta\vec{X}(t)$, under the impact of an initial perturbation from the reference path, i.e. $\delta\vec{X}(t_0)$. By substituting $\Phi(t,t_0)$ into equation (2.33), the following differential equation is derived,

$$\dot{\Phi}(t,t_0) = A(t)\Phi(t,t_0) \tag{2.37}$$

With the initial condition,

$$\Phi(t_0,t_0) = I_{6\times6} \tag{2.38}$$

The STM can be solved numerically by simultaneously integrating equation (2.37) with the equations of motion in (2.26)-(2.28), which would result in integration of a total of 42 differential equations.

### 2.2.2. Differential Corrections Algorithm for Halo Orbits

Halo orbits in the CR3BP are symmetric about the $\hat{x}-\hat{z}$ plane, which means that they cross the $\hat{x}-\hat{z}$ plane perpendicularly such that the velocity components at the crossings in the $\hat{x}$ and $\hat{z}$ directions are zero. This natural feature of the halo orbits can be utilized to formulate a differential corrections process. First, an initial guess, $\vec{X}(t_0)$, for the differential corrections algorithm needs to be chosen. This initial guess will be located in the $\hat{x}-\hat{z}$ plane, and has an initial velocity perpendicular to the $\hat{x}-\hat{z}$ plane. Therefore, $\vec{X}(t_0)$ may take the following form,

$$\vec{X}(t_0) = [x_0\ 0\ z_0\ 0\ \dot{y}_0\ 0]^T \tag{2.39}$$

In general, if the initial guess in (2.39) is propagated forward in time, it may not create a second perpendicular crossing in the $\hat{x}-\hat{z}$ plane. Therefore a differential corrections

algorithm needs to be employed to vary the initial guess such that the second $\hat{x} - \hat{z}$ crossing also becomes perpendicular.

The variational equations of motion given in (2.35) approximate state variations over a fixed time interval. These equations can be augmented to incorporate time variations as well,

$$\delta\vec{X}(t_f) = \Phi(t_f, t_0)\,\delta\vec{X}(t_0) + \dot{\vec{X}}(t)\delta t \tag{2.40}$$

Where $t_f$ is half the orbital period when the $\hat{x} - \hat{z}$ perpendicular crossing occurs. Next, the variational equations in (2.40) can be written in scalar form as follows,

$$\delta x_f = \phi_{11}\delta x_0 + \phi_{12}\delta y_0 + \phi_{13}\delta z_0 + \phi_{14}\delta\dot{x}_0 + \phi_{15}\delta\dot{y}_0 + \phi_{16}\delta\dot{z}_0 + \dot{x}\delta t \tag{2.41}$$

$$\delta y_f = \phi_{21}\delta x_0 + \phi_{22}\delta y_0 + \phi_{23}\delta z_0 + \phi_{24}\delta\dot{x}_0 + \phi_{25}\delta\dot{y}_0 + \phi_{26}\delta\dot{z}_0 + \dot{y}\delta t \tag{2.42}$$

$$\delta z_f = \phi_{31}\delta x_0 + \phi_{32}\delta y_0 + \phi_{33}\delta z_0 + \phi_{34}\delta\dot{x}_0 + \phi_{35}\delta\dot{z}_0 + \phi_{36}\delta\dot{z}_0 + \dot{z}\delta t \tag{2.43}$$

$$\delta\dot{x}_f = \phi_{41}\delta x_0 + \phi_{42}\delta y_0 + \phi_{43}\delta z_0 + \phi_{44}\delta\dot{x}_0 + \phi_{45}\delta\dot{y}_0 + \phi_{46}\delta\dot{z}_0 + \ddot{x}\delta t \tag{2.44}$$

$$\delta\dot{y}_f = \phi_{51}\delta x_0 + \phi_{52}\delta y_0 + \phi_{53}\delta z_0 + \phi_{54}\delta\dot{x}_0 + \phi_{55}\delta\dot{y}_0 + \phi_{56}\delta\dot{z}_0 + \ddot{y}\delta t \tag{2.45}$$

$$\delta\dot{z}_f = \phi_{61}\delta x_0 + \phi_{62}\delta y_0 + \phi_{63}\delta z_0 + \phi_{64}\delta\dot{x}_0 + \phi_{65}\delta\dot{y}_0 + \phi_{66}\delta\dot{z}_0 + \ddot{z}\delta t \tag{2.46}$$

A differential corrections algorithm can be formulated by either fixing $x_0$, or $z_0$. If it is desired to fix $x_0$, then $\delta x_0 = \delta x_f = 0$ in (2.41)-(2.42). Hence, the scalar variational equations can be written as,

$$0 = \phi_{23}\delta z_0 + \phi_{25}\delta\dot{y}_0 + \dot{y}\delta t \tag{2.47}$$

$$\delta\dot{x}_f = \phi_{43}\delta z_0 + \phi_{45}\delta\dot{y}_0 + \ddot{x}\delta t \tag{2.48}$$

$$\delta\dot{z}_f = \phi_{63}\delta z_0 + \phi_{65}\delta\dot{y}_0 + \ddot{z}\delta t \tag{2.49}$$

From (2.47), $\delta t$ can be express as,

$$\delta t = -\frac{1}{\dot{y}}[\phi_{23}\delta z_0 + \phi_{25}\delta \dot{y}_0] \tag{2.50}$$

By plugging equation (2.50) into equations (2.48) and (2.49), they can be written in matrix form as follows,

$$\begin{bmatrix}\delta \dot{x}_f \\ \delta \dot{z}_f\end{bmatrix} = \left[\begin{bmatrix}\phi_{43} & \phi_{45} \\ \phi_{63} & \phi_{63}\end{bmatrix} - \frac{1}{\dot{y}}\begin{bmatrix}\ddot{x} \\ \ddot{z}\end{bmatrix}\begin{bmatrix}\phi_{23} & \phi_{25}\end{bmatrix}\right]\begin{bmatrix}\delta z_0 \\ \delta \dot{y}_0\end{bmatrix} \tag{2.51}$$

Therefore, the differential corrections update equation for a symmetric periodic halo orbit with a fixed $x_0$ is given by:

$$\begin{bmatrix}\delta z_0 \\ \delta \dot{y}_0\end{bmatrix} = \left[\begin{bmatrix}\phi_{43} & \phi_{45} \\ \phi_{63} & \phi_{63}\end{bmatrix} - \frac{1}{\dot{y}}\begin{bmatrix}\ddot{x} \\ \ddot{z}\end{bmatrix}\begin{bmatrix}\phi_{23} & \phi_{25}\end{bmatrix}\right]^{-1}\begin{bmatrix}\delta \dot{x}_f \\ \delta \dot{z}_f\end{bmatrix} \tag{2.52}$$

By using equation (2.52) and (2.50), the initial states $z_0$, $\dot{y}_0$, and half the orbital period $t_f$ are updated iteratively until $\delta \dot{x}_f < \epsilon$ and $\delta \dot{z}_f < \epsilon$, where $\epsilon$ is a small numerical tolerance

Alternatively, if it is desired to fix $z_0$, then $\delta z_0 = \delta z_f = 0$ in (2.41)-(2.42). Hence, the scalar variational equations can be written as,

$$0 = \phi_{21}\delta x_0 + \phi_{25}\delta \dot{y}_0 + \dot{y}\delta t \tag{2.53}$$

$$\delta \dot{x}_f = \phi_{41}\delta x_0 + \phi_{45}\delta \dot{y}_0 + \ddot{x}\delta t \tag{2.54}$$

$$\delta \dot{z}_f = \phi_{61}\delta x_0 + \phi_{65}\delta \dot{y}_0 + \ddot{z}\delta t \tag{2.55}$$

From (2.53), $\delta t$ can be express as,

$$\delta t = -\frac{1}{\dot{y}}[\phi_{21}\delta x_0 + \phi_{25}\delta \dot{y}_0] \tag{2.56}$$

By plugging equation (2.56) into equations (2.54) and (2.55), they can be written in matrix form as follows,

$$\begin{bmatrix}\delta\dot{x}_f\\ \delta\dot{z}_f\end{bmatrix} = \left[\begin{bmatrix}\phi_{41} & \phi_{45}\\ \phi_{61} & \phi_{63}\end{bmatrix} - \frac{1}{\dot{y}}\begin{bmatrix}\ddot{x}\\ \ddot{z}\end{bmatrix}\begin{bmatrix}\phi_{21} & \phi_{25}\end{bmatrix}\right]\begin{bmatrix}\delta x_0\\ \delta\dot{y}_0\end{bmatrix} \tag{2.57}$$

Therefore, the differential corrections update equation for a symmetric periodic halo orbit with a fixed $z_0$ is given by:

$$\begin{bmatrix}\delta x_0\\ \delta\dot{y}_0\end{bmatrix} = \left[\begin{bmatrix}\phi_{41} & \phi_{45}\\ \phi_{61} & \phi_{63}\end{bmatrix} - \frac{1}{\dot{y}}\begin{bmatrix}\ddot{x}\\ \ddot{z}\end{bmatrix}\begin{bmatrix}\phi_{21} & \phi_{25}\end{bmatrix}\right]^{-1}\begin{bmatrix}\delta\dot{x}_f\\ \delta\dot{z}_f\end{bmatrix} \tag{2.58}$$

By using equation (2.58) and (2.56), the initial states $x_0$, $\dot{y}_0$ and half the orbital period $t_f$ are updated iteratively until $\delta\dot{x}_f < \epsilon$ and $\delta\dot{z}_f < \epsilon$. A full periodic halo orbit can then be obtained by propagating the corrected initial guess over the period $T = 2t_f$.

### 2.2.3. Numerical Example: $L_1$ and $L_2$ Halo Families

By using the differential corrections algorithms developed in the previous section, a single periodic halo orbit can be generated from a given initial condition. To create a family of halo orbits, a continuation scheme needs to be employed to predict an initial guess for the next orbit in the family. For the fixed $x_0$ differential corrections scheme in (2.52), the initial guess for the neighbouring halo orbit is obtained by,

$$\begin{bmatrix}x_0\\ y_0\\ z_0\\ \dot{x}_0\\ \dot{y}_0\\ \dot{z}_0\end{bmatrix}^{n+1} = \begin{bmatrix}x_0\\ y_0\\ z_0\\ \dot{x}_0\\ \dot{y}_0\\ \dot{z}_0\end{bmatrix}^{n} + \begin{bmatrix}\Delta x_0\\ 0\\ 0\\ 0\\ 0\\ 0\end{bmatrix} \tag{2.59}$$

Where $\left[x_0\ y_0\ z_0\ \dot{x}_0\ \dot{y}_0\ \dot{z}_0\right]^{n^T}$ is the initial condition from a previously converged orbit, and $\Delta x_0$ is a step size. This continuation scheme is also denoted as a single parameter continuation scheme since only one of the states is updated to predict the next initial guess. This initial guess is then corrected using the differential corrections algorithm in (2.52) to generate the next halo orbit in the family. Alternatively, for the fixed $z_0$ differential corrections scheme in (2.58), the initial guess for the neighbouring halo orbit is obtained by,

$$\begin{bmatrix} x_0 \\ y_0 \\ z_0 \\ \dot{x}_0 \\ \dot{y}_0 \\ \dot{z}_0 \end{bmatrix}^{n+1} = \begin{bmatrix} x_0 \\ y_0 \\ z_0 \\ \dot{x}_0 \\ \dot{y}_0 \\ \dot{z}_0 \end{bmatrix}^{n} + \begin{bmatrix} 0 \\ 0 \\ \Delta z_0 \\ 0 \\ 0 \\ 0 \end{bmatrix} \tag{2.60}$$

Next, a methodology needs to be established to choose a suitable correction and continuation scheme from either the fixed $x_0$ or the fixed $z_0$ schemes. This methodology is based on the fact that the developed differential corrections algorithms are essentially multi-dimensional sloped based, Newton-Raphson schemes. Therefore, in regions where $x_0$ is changing more rapidly than $z_0$, i.e.,

$$|x_0^{n+1} - x_0^n| > |z_0^{n+1} - z_0^n| \tag{2.61}$$

a fixed $x_0$ correction and continuation scheme should be used to avoid running into a singularity. When (2.61) fails to be true, that is when $z_0$ is changing more rapidly than $x_0$, the correction and continuation scheme is then switched to a fixed $z_0$ scheme. Figure 2.4 illustrates the generated $L_1$ and $L_2$ halo families in the Sun-Earth/Moon system. As can be seen in figure 2.4, members of each family come in pairs that are reflection of each other relative to the $\hat{x} - \hat{y}$ plane. Those member with the maximum out-of-plane excursion above the $\hat{x} - \hat{y}$ plane are known as the "northern" halo orbits, and those orbit with maximum out-of-plane excursion below the $\hat{x} - \hat{y}$ plane are known as the "southern" halo orbit

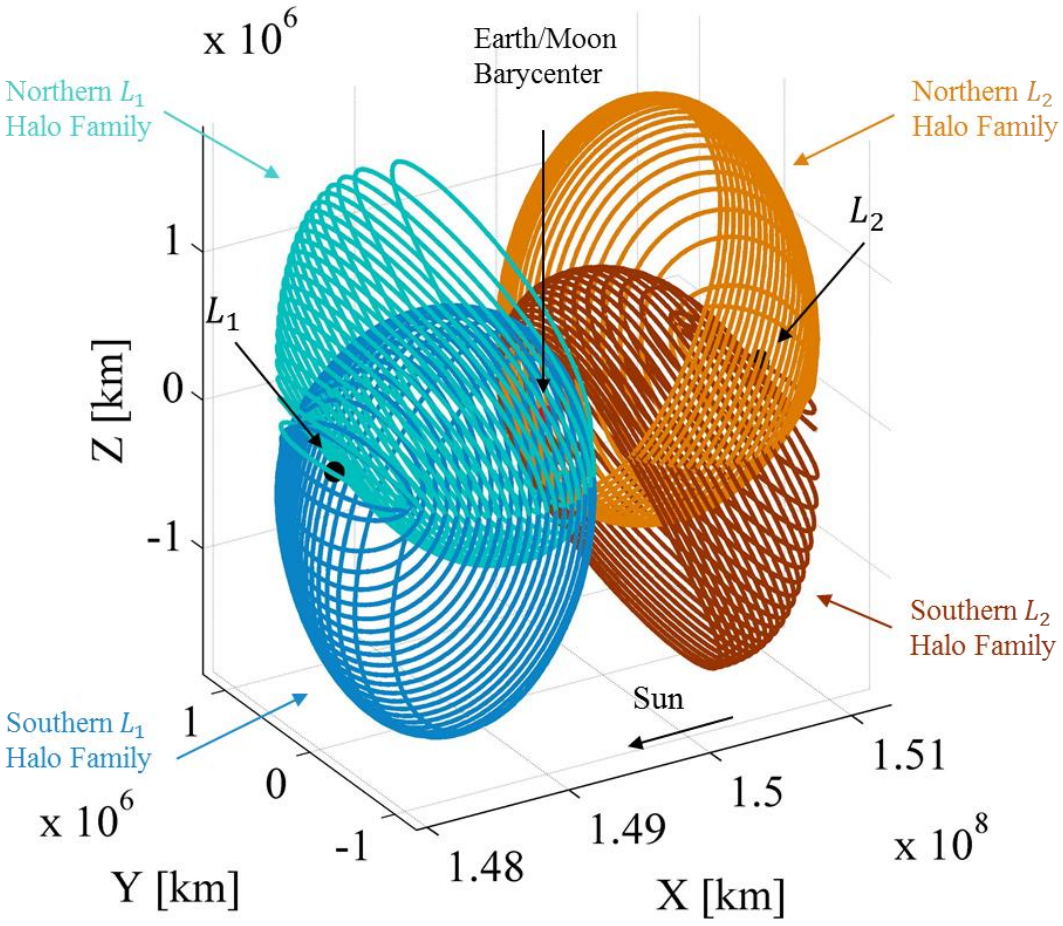


*Figure 2.4. $L_1$ and $L_2$ Halo Families in the Sun-Earth/Moon*

## 2.3. Global Invariant Manifolds

The dynamical flow of the phase space in the vicinity of a periodic orbit in the CR3BP can be characterized by unique sets of trajectories, known as the invariant manifolds. The trajectories on an invariant manifold create surfaces that share similar stability properties. These surfaces are invariant in the six-dimensional phase space in a sense that a trajectory on an invariant manifold must remain on that manifold for all past and future times. In general, three types of invariant manifolds exist in the vicinity of a periodic orbit: stable, unstable, and center manifolds.

### 2.3.1. Stable and Unstable Manifolds

Stable and unstable manifolds are formally defined for a fixed point in a diffeomorphism. A diffeomorphism is a ono-to-one and on-to map which is both invertible and differentiable. A fixed point or invariant point is defined as a point $\vec{x}^*$ that repeatedly maps on to itself. Therefore a periodic orbit is a fixed point under a diffeomorphism. Stable and unstable manifolds for a fixed point $\vec{x}^*$ are defined as follows [26],

**Definition 2.1.** *The local stable manifold $W_{loc}^S$ of a fixed point $\vec{x}^*$ is the set of all $\vec{x}$ in the neighborhood of $\vec{x}^*$that approaches $\vec{x}^*$ as $j \to \infty$.*

**Definition 2.2.** *The local unstable manifold $W_{loc}^U$ of a fixed point $\vec{x}^*$ is the set of all $\vec{x}$ in the neighborhood of $\vec{x}^*$that departs $\vec{x}^*$ as $j \to \infty$.*

In definitions 2.1 and 2.2, $j$ indicates the number of iterations on the map. The global stable manifold $W^S$ associated with the local stable manifold $W_{loc}^S$ is obtained by propagating points in $W_{loc}^S$ forward in time. Similarly, the global unstable manifold $W^U$ is obtained by propagating points in $W_{loc}^U$ backward in time.

A relationship exists between the local invariant manifolds and the subspace of the monodramy matrix. This relationship can be exploited to numerically approximate and determine the invariant manifolds around a periodic orbit. In general, the eigenspace of the

monodromy matrix is expressed as follows. The eigenvalues and the associated eigenvectors of the monodromy matrix are denoted as $\epsilon_i$ and $\vec{v}_i$, respectively. Let $n_S$ be the number of stable eigenvalues $\epsilon_{S,i}$ with $||\epsilon_{S,i}|| < 1$, $n_U$ be the number of unstable eigenvalues $\epsilon_{U,i}$ with $||\epsilon_{U,i}|| > 1$, $n_C$ be the number of center eigenvalues $\epsilon_{C,i}$ with $||\epsilon_{C,i}|| = 1$, and, $\vec{v}_{S,i}$, $\vec{v}_{U,i}$, $\vec{v}_{C,i}$ be the associated eigenvectors. Then, the subspaces of the monodromy matrix are defined as,

$$E^S = span\{\vec{v}_{S,i}\}_{i=1}^{n_S} \tag{2.62}$$

$$E^U = span\{\vec{v}_{U,i}\}_{i=1}^{n_U} \tag{2.63}$$

$$E^C = span\{\vec{v}_{C,i}\}_{i=1}^{n_C} \tag{2.64}$$

Where $E^S$, $E^U$, and $E^C$ are the stable, unstable, and center subspaces, respectively. For the halo orbits of interest in this study, $n_S$ and $n_U$ are equal to one, and $n_C$ is equal to four. From the four eigenvalues in the center subspace, two of them are exactly equal to one, and the remaining two are on the unitary circle and are complex conjugates of each other.

Next, according to the Stable Manifold Theorem [27], the local stable and unstable manifolds, $W_{loc}^S$ and $W_{loc}^U$, are tangent to the stable and unstable subspaces, $E^S$ and $E^U$, at the fix point, and have the same dimensions $n_S$ and $n_U$. In other words, $E^S$ and $E^U$ are local linear approximations for $W_{loc}^S$ and $W_{loc}^U$, respectively. This relationship can be used to numerically approximate the local stable and unstable manifolds for any point along a periodic orbit by perturbing the states in the directions of the stable an unstable eigenvectors, $\vec{v}_{S,i}$ and $\vec{v}_{U,i}$.[28]. Additionally, stable and unstable manifolds are unique, meaning that a manifold does not intersects itself or another manifold of the same type [27]. Figure 2.5 shows the stable and unstable manifolds for a southern $L_1$ halo orbit in the Sun-Earth/Moon system. The blue trajectories which are approaching the halo orbit are located on the stable manifold. The red trajectories which are departing from the halo orbit are located on the unstable manifold.

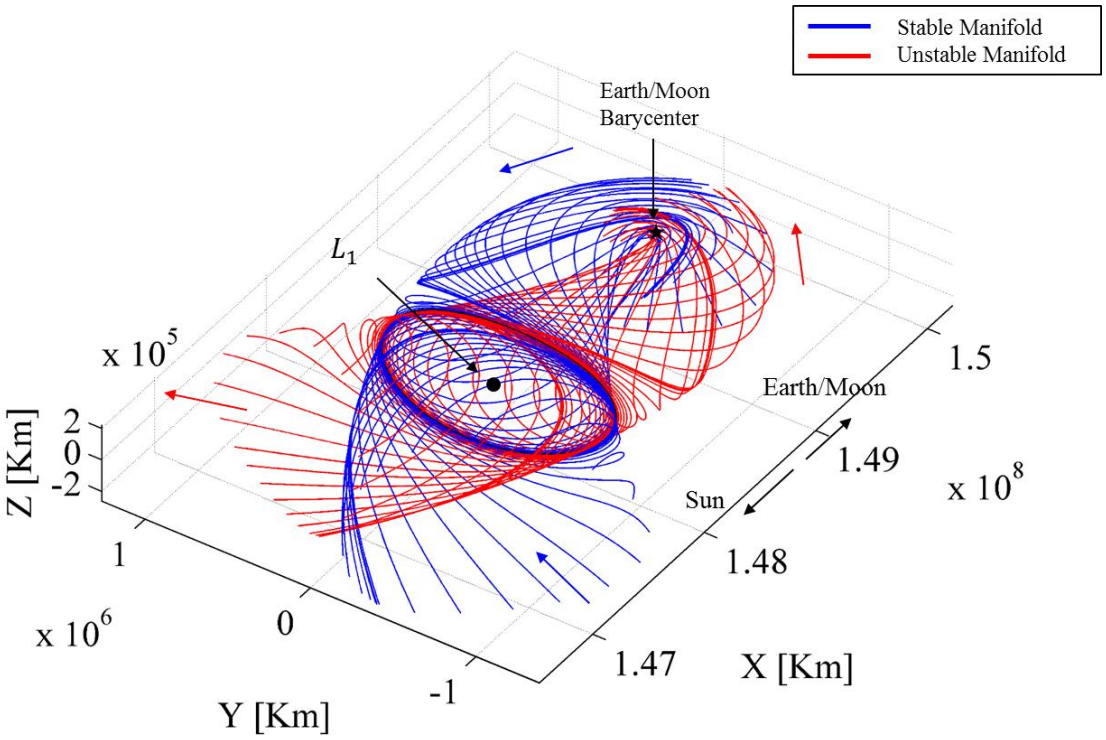


*Figure 2.5. Stable and Unstable Manifolds around an $L_1$ Halo Orbit*

### 2.3.2. Center Manifold and Floquet Analysis

The center manifold of a fixed point under a diffeomorphism is defined as follows,

**Definition 2.3.** *The local center manifold $W_{loc}^{C}$ of a fixed point $\vec{x}^*$ is the set of all $\vec{x}$ in the neighborhood of $\vec{x}^*$that neither approaches nor departs $\vec{x}^*$ as $j \to \infty$, rather it stays in the bounded vicinity of $\vec{x}^*$.*

Based on definition 2.3, the center manifold comprises bounded motions relative to the periodic orbit such as quasi-periodic solutions. Similar to the stable and unstable manifolds, the center manifold is also related to the subspace of the monodramy matrix. According to the Center Manifold Theorem [27], the local center manifold, $W_{loc}^{C}$, is tangent to the center subspace, $E^C$, and have the same dimension $n_C$. However, the center manifold is not necessarily unique [27]. The global center manifold $W^C$ associated with the local stable manifold $W_{loc}^{C}$ is also obtained by propagating points in $W_{loc}^{C}$ forward or backward in time.

The natural characteristic of the phase space near a periodic orbit can be further analyzed through Floquet theory [29]:

**Theorem 2.1.** *The fundamental solution matrix $\phi(t, t_0)$ for the time varying T-periodic system (2.33) can be decomposed as follows,*

$$\Phi(t, 0) = E(t)e^{Jt}E^{-1}(0) \qquad (2.65)$$

*Where $E(t)$ is non-singular, differentiable, and T-periodic matrix. $J$ is a constant diagonal matrix. Furthermore, $E(0)$ is the matrix of eigenvecotrs of the monodromy matrix, $\Phi(T, 0)$.*

The matrix $J$ in equation (2.65) is related to the eigenvalues of the monodromy matrix as follows,

$$\Phi(T, 0) = E(T)e^{Jt}E^{-1}(0) \qquad (2.66)$$

Since $E(t)$ is a T-periodic matrix, then $E(T) = E(0)$. Therefore, from (2.66), $E(T)$ contains the eigenvectors of the monodrmy matrix and $e^{Jt}$ contains the eigenvalues of the monodromy matrix. The diagonal entries of $J$ are known as the Poincare exponents and have a general complex form as $e_j^* = a_j + ib_j$. The eigenvalues of the monodromy matrix, $\epsilon_j$, and the Poincare exponents, $e_j^*$, are related as follows,

$$\epsilon_j = \exp(e_j^* T) \tag{2.67}$$

Therefore, the Poincare exponents provide stability information about the associated periodic orbit. This stability information is summarized in table 2.1, which also is also compared with the stability information provided by the eigenvalues of the monodromy matrix.

*Table 2.1. Stability Information Provided by the Poincare Exponents and the Eigenvalues of the Monodromy Matrix*

| | *Poincare Exponents* $e_j^* = a_j + ib_j$ | *Eigenvalues of* $\Phi(T, 0)$ $\epsilon_j = \exp(e_j^* T)$ |
|---|---|---|
| Unstable | $a_j > 0$ | $\|\|\epsilon_j\|\| > 1$ |
| Stable | $a_j < 0$ | $\|\|\epsilon_j\|\| < 1$ |
| Center | $a_j = 0$ | $\|\|\epsilon_j\|\| = 1$ |

# 3. ORBITAL STATION-KEEPING SIMULATION ALGORITHM

A numerical simulation algorithm is employed to compute the spacecraft's trajectory under the influence of the Sun-Earth/Moon gravitational force model in the CR3BP. The simulation algorithm allows implementation of station-keeping control strategies that aim to maintain the motion of the spacecraft in the vicinity of a nominal trajectory. In this investigation the performances of orbital station-keeping control laws are examined under the impacts of the spacecraft's operation errors and design constraints. This simulation algorithm also provides groundwork for implementation of additional perturbations such as the solar radiation pressure and additional attracting bodies for future investigations. In this chapter, the orbital station-keeping control problem is elaborated. The nominal orbit as well as mission design constraints and operation errors that are used for this investigation are introduced.

## 3.1. Definition of the Orbital Station-Keeping Problem

In general, libration point orbits are inherently unstable and without the presence of corrective maneuvers a spacecraft will diverge from the vicinity of such orbits. Other perturbations such as an initial orbital injection error, spacecraft's state tracking errors and maneuver execution errors will result in a faster divergence of the spacecraft. Consequently, orbital station-keeping strategies must be implemented to maintain the spacecraft's trajectory in the vicinity of a desired nominal path. In this study, the "vicinity" of the nominal trajectory is defined as a torus of 10,000 km around the reference path. The performances of station-keeping strategies are examined through a numerical simulation that computes the station-keeping's fuel consumption, and the spacecraft's trajectory in the gravitational environment of the CR3BP in the Sun-Earth/Moon system. As one of the

primary objectives of this investigation, for more realistic station-keeping simulations, perturbations caused by operation errors as well as maneuver restrictions caused by mission design constraints are included in the simulation algorithm. The details on the mission operation errors and design constraints are elaborated in section 3.3 and 3.4, respectively.

## 3.2. Nominal Orbit

For this investigation, the nominal orbit is selected to be an $L_1$ halo orbit in the Sun-Earth/Moon system. This orbit is similar to the nominal trajectory used in ISEE-3 and SOHO missions. Keeter [15] and Marchand [21] also studied similar trajectories in their investigation which would provide a reference point for comparison of station-keeping performance results. $L_1$ halo orbits have extensive applications for solar observatories, space weather, and Geostorm warning missions. Out of plane excursion of these orbits also allows for a continuous communication between the spacecraft and the Earth. Figure 3.1 illustrates the nominal halo orbit used in this investigation. This plot includes the three projections of the nominal trajectory in $\hat{x} - \hat{y}$, $\hat{x} - \hat{z}$, and $\hat{y} - \hat{z}$ planes. This nominal orbit is one of the "southern" members of the $L_1$ halo family as the majority of the trajectory is below the plane of primary motion. Additionally, the maximum out of plane excursion amplitude, $A_z$, for this orbit is approximately equal to 223,992 km and the period of this orbit is approximately 5 months and 27 days. For this investigation, the station-keeping duration is chosen to be 10 periods of the nominal trajectory which is approximately 5 years.

## 3.3. Mission Operation Errors

Upon arrival to a target location in the nominal orbit a maneuver is executed to "inject" the spacecraft into the nominal trajectory. This orbital injection maneuver adjusts the position and velocity of the spacecraft to match those of the nominal orbit. However, errors

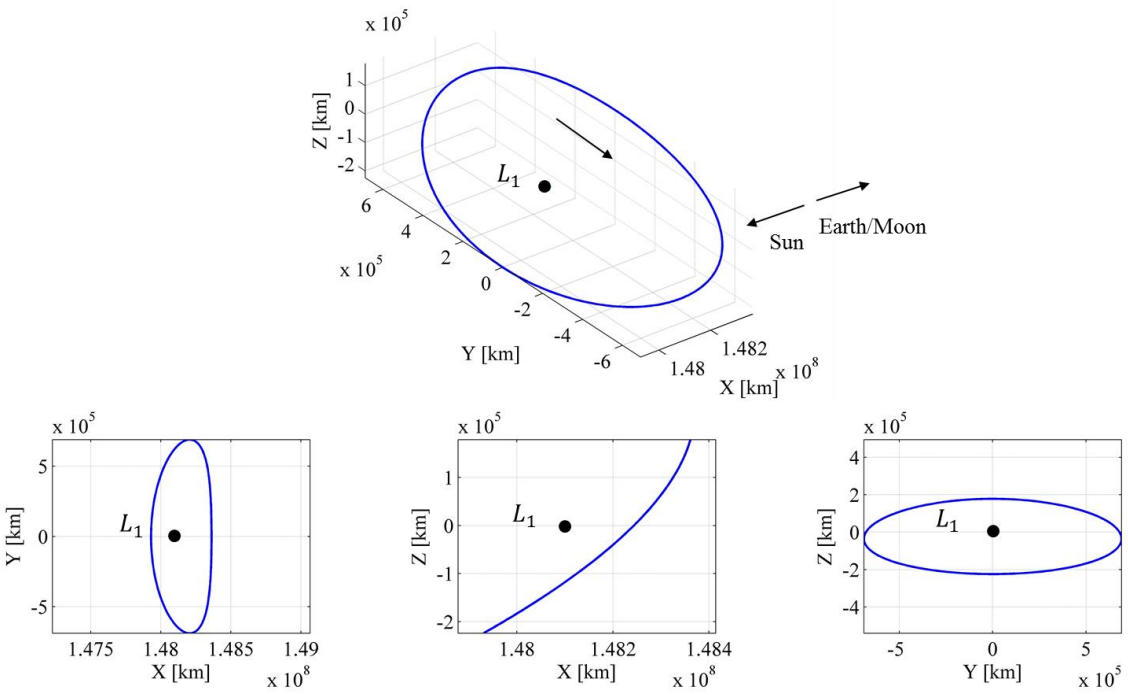


*Figure 3.1. Nominal Orbit*

are expected to occur in the execution of this maneuver which would result in an imperfect orbital injection. In the simulation algorithm, orbital injection errors are mimicked by perturbing the spacecraft's initial state on the nominal orbit through a random perturbation. In this study, a random orbital injection error in position and velocity with variances of 1 km and 1 cm/s, respectively, is employed [15, 20].

Spacecraft's orbital tracking data, which are computed by Earth-based tracking stations, are also influenced by various sources of errors [15, 22]. Thus these errors must be included in the station-keeping simulation algorithm, and a successful station-keeping control strategy must operate effectively under these errors. Similar to injection errors, orbital tracking errors are introduced in the simulation algorithm through random 1-$\sigma$ error of 1 km and 1 cm/s in position and velocity, respectively [15, 20].

Another important source of operation errors comes from inaccuracies of the propulsion system that implements the corrective maneuvers. Due to these inaccuracies, thrusters on-board a spacecraft cannot implement a precise corrective maneuver based on the command

of the control system. Therefore, an effective station-keeping control strategy must also be capable of handling such maneuver execution errors. To include these errors in the station-keeping simulation algorithm, a calculated corrective maneuver is randomly perturbed by a 1-$\sigma$ error of 1% of the maneuver [20].

## 3.4. Mission Design Constraints

In each mission, there are certain design constraints that restrict the implementation of corrective maneuvers. One such constraint is regulated by the minimum time required to obtain accurate post-burn orbit determination data, and/or the minimum time requirement for scientific operations. This constraint restricts the time between two successive impulsive maneuvers, or in the case of a continuous controller, it restricts the time elapsed until the continuous controller could be updated. In this study, this minimum time interval is denoted as $\Delta t_{min}$, and its value is chosen to be 3 weeks which corresponds to the value of $\Delta t_{min}$ for the DSCOVR mission [19].

Another design constraint is the minimum allowable maneuver magnitude that can be implemented by the on-board propulsion system. In the simulation algorithm, if the magnitude of the calculated maneuver is less than a certain threshold, then the applied maneuver is set to zero. For an impulsive thruster, the minimum allowable maneuver magnitude is characterized by $\left|\Delta\vec{V}\right|_{min}$ which has a magnitude of 0.025 m/s, chosen based on ISEE-3 mission data [15]. For a continuous thruster, the minimum allowable maneuver magnitude is characterized by the minimum thrust level which has a magnitude of 0.3 mN. This minimum thrust level is chosen based on an RIT-10 ionic propulsion system, and assumes a total mass of 1000 kg for the spacecraft [18].

The last constraint is based on the rate of change of the magnitude of spacecraft's position error vector relative to the nominal orbit. To avoid implementation of an unnecessary corrective maneuver, the magnitude of position error must be increasing between successive orbit tracking intervals. In the simulation algorithm, a corrective maneuver will be implemented only if all three constraints are simultaneously satisfied.

## 3.5. Monte Carlo Simulation

Since the simulated operation errors are random perturbations, station-keeping result from one trail does not have a high statistical significance as it represents only one outcome from infinitely many station-keeping outcomes. To have a more representative solution space, station-keeping results must be presented as an average of multiple trials. The performance of a station-keeping control strategy is examined by the total amount of fuel consumption or $\Delta V_T$, and a Monte Carlo simulation is conducted to take the average of $\Delta V_T$ over multiple station-keeping trails. The sample size for the Monte Carlo simulation is chosen such that the moving average of $\Delta V_T$ stays constant or does not change significantly for further number of trails.

In this study two types of control strategies, impulsive and continuous, are examined. $\Delta V_T$ for an impulsive control strategy is calculated as,

$$\Delta V_T = \sum_{k=1}^{m} |\Delta \vec{V}_k| \tag{3.1}$$

Where $|\Delta \vec{V}_k|$ is the magnitude of an impulsive corrective maneuver velocity vector, and $m$ the number of maneuvers. For a continuous control strategy, $\Delta V_T$ is calculated as follows,

$$\Delta V_T = \int_0^t |\vec{u}(\tau)|\, d\tau \tag{3.1}$$

Where $|\vec{u}|$ is the magnitude of a continuous corrective maneuver acceleration vector, and $t$ is the duration of the mission.

# 4. IMPULSIVE FLOQUET MODE (FM) STATION-KEEPING STRATEGY

The Floquet Mode (FM) control strategy is an instantaneous or impulsive state-feedback control law that exploits the natural dynamical characteristic of the phase space near periodic orbits. This controller utilizes the Invariant Manifold Theorem to compute the corrective maneuvers. Floquet Modes are used to compute the unstable components of the state error vector, by using the eigenstructure of the STM after one period (i.e. the monodromy matrix). A corrective maneuver is then calculated that aims to cancel the unstable component of the state error vector, and places the spacecraft in a bounded and quasi-periodic motion around the nominal trajectory. Such control strategy has applications in formation flight of spacecraft and interferometry imaging which would benefit from the spiral-like and bounded motion provided by the controller. In this chapter, the mathematical formulation of the Floquet Mode controller is presented. Next, a modified formulation for this controller is derived that incorporates feasible maneuver direction constraints into the design of the controller. Lastly, the modified Floquet Mode controller is applied for station-keeping around the nominal halo orbit, presented in chapter 3, under mission design constraint and operation errors.

## 4.1. FM Controller Formulation

As discussed in section 2.3.2, by using the Floque Thoery the state transition matrix of a time-varying periodic linear system can be decomposed as follows,

$$\Phi(t,0) = E(t)e^{Jt}E^{-1}(0) \tag{4.1}$$

Where $E(t)$ is the periodic Floquet Modal matrix, $J$ is a constant diagonal matrix in which the diagonal entries are the Poincare exponents, and $E(0)$ is the matrix of eigenvecotrs of the monodromy matrix, $\Phi(T,0)$. Furthermore, columns of $E(t)$, $\vec{e}_j$, form a six dimensional, non-orthogonal basis that are defined as Floquet modes. At any point along the nominal orbit, the state error vector, $\delta\vec{X}(t)$, can be expressed in terms of the Floquet mode basis as follows,

$$\delta\vec{X}(t) = \sum_{j=1}^{6} c_j(t)\vec{e}_j(t) \tag{4.2}$$

$$\delta\vec{X}(t) = \delta\vec{X}_1 + \delta\vec{X}_2 + \delta\vec{X}_3 + \delta\vec{X}_4 + \delta\vec{X}_5 + \delta\vec{X}_6 \tag{4.3}$$

Where $\delta\vec{X}_1$ and $\delta\vec{X}_2$ are the components of $\delta\vec{X}(t)$ along the stable and unstable Floquet modes, respectively. $\delta\vec{X}_3$ through $\delta\vec{X}_6$ are the components along the oscillatory Floquet modes. The coefficients $c_j(t)$ are the elements of vector $\vec{c}(t)$ defined as,

$$\vec{c}(t) = E^{-1}(t)\delta\vec{X}(t) \tag{4.4}$$

In the FM controller, a corrective maneuver in the form of $\Delta\vec{V} = [0,0,0,\Delta V_x,\Delta V_y,\Delta V_z]^T$ is implemented that aims to remove the unstable component of the error vector. That is,

$$\delta\vec{X}(t) + \Delta\vec{V} = \alpha_2\delta\vec{X}_2 + \alpha_3\delta\vec{X}_3 + \cdots + \alpha_6\delta\vec{X}_6 \tag{4.5}$$

Where $\alpha_i$'s are the coefficients of $\delta\vec{X}_i$'s once the corrective maneuver is applied. (4.5) is a system of six linear equations with eight unknowns. The unknowns of (4.5) are $\Delta V_x$, $\Delta V_y$, $\Delta V_z$, and $\alpha_i$'s ($i$ = 2,3,…6). This underdetermined system of equations does not possess a unique solution. In [15], Keeter solves for the required $\Delta\vec{V}$ maneuver through a minimum norm solution. The fact that these equations do not have an exact solution provides an

opportunity that allows additional implementation of constraints on the corrective maneuver.

## 4.2. Incorporation of Feasible Maneuver Directions in the FM Controller Design

Often, requirements of scientific instruments or the spacecraft's manufacturing design, constraints the directions that a corrective maneuver can be executed. Therefore, a suitable station-keeping control strategy must be capable of handling the added constraint of a feasible maneuver direction to ensure the success of the mission. An example of a mission with such constraints on the maneuver direction is the ARTEMIS (Acceleration Reconnection and Turbulence and Electrodynamics of the Moon's Interaction with the Sun) mission. The ARTEMIS spacecraft are spin stabilized vehicles and the thrusters in these spacecraft are mounted in such a way that corrective maneuvers can only be implemented along the spin axis toward the south ecliptic pole direction, or in the plane perpendicular to the spin axis [20].

By exploiting the non-unique solution space of the FM controller, additional constraints on the direction of the corrective maneuvers can be implemented which enables station-keeping for mission scenarios such as the ARTEMIS. In this study two constraint scenarios will be addressed: 1) plane constraint, where all maneuvers are implemented in a desired plane, 2) line constraint, where all maneuvers are along a desired axis.

### 4.2.1. Plane Constraint

To constrain a corrective maneuvers in a desired plane, the following equation must hold,

$$\Delta V_x \times N_x + \Delta V_y \times N_y + \Delta V_z \times N_z = 0 \tag{4.6}$$

Where $\vec{N} = \left[N_x, N_y, N_z\right]^T$ is the plane normal. For example, in the case of the ARTEMIS mission the plane normal is defined as the spin axis of the spacecraft. To solve for a

corrective maneuver using the FM controller, equation (4.5) is augmented with equation (4.6),

$$\begin{aligned} \delta\vec{X}(t) + \Delta\vec{V} &= \alpha_2\delta\vec{X}_2 + \alpha_3\delta\vec{X}_3 + \cdots + \alpha_6\delta\vec{X}_6 \\ \Delta V_x \times N_x + \Delta V_y \times N_y + \Delta V_z \times N_z &= 0 \end{aligned} \tag{4.7}$$

System of equations in (4.7), consists of seven linear equations with eight unknown. A minimum norm solution to these equations can be found through a simple Newton-Raphson algorithm. MATLAB's fsolve command can also be used to provide a solution.

### 4.2.2. Line Constraint

To constrain a corrective maneuvers along a desired axis, the following equations must hold,

$$\frac{L_x - \Delta V_x}{L_x} = \frac{L_y - \Delta V_y}{L_y} \tag{4.8}$$

$$\frac{L_x - \Delta V_x}{L_x} = \frac{L_z - \Delta V_z}{L_z} \tag{4.9}$$

Where $\vec{L} = [L_x, L_y, L_z]^T$ is the desired axis along which the corrective maneuver is constrained. In the case of the ARTEMIS mission, $\vec{L}$ is defined as the spin axis. To solve for a corrective maneuver using the FM controller, equation (4.5) is augmented with equations (4.8) and (4.9),

$$\begin{aligned} \delta\vec{X}(t) + \Delta\vec{V} &= \alpha_2\delta\vec{X}_2 + \alpha_3\delta\vec{X}_3 + \cdots + \alpha_6\delta\vec{X}_6 \\ \frac{L_x - \Delta V_x}{L_x} &= \frac{L_y - \Delta V_y}{L_y} \\ \frac{L_x - \Delta V_x}{L_x} &= \frac{L_z - \Delta V_z}{L_z} \end{aligned} \tag{4.10}$$

System of equations in (4.10), consists of eight linear equations with eight unknown which holds an exact solution that can be easily solved through a Newton-Raphson method or MATLAB's fsolve command.

## 4.3. Simulation Results

In this section, the FM controller is applied for station-keeping in the non-linear dynamics around the nominal $L_1$ halo orbit introduced in section 3.2. Orbital station-keeping for spin-stabilized spacecraft with two types of maneuver constraints are studied: 1) spin-stabilized spacecraft with only tangential thrusters, 2) spin-stabilized spacecraft with only axial thrusters. In each scenario the spin axis is defined by vector $\vec{V}_s$ which is characterized by an in-plane angle $\gamma$, and an out-of-plane angle $\phi$, as shown in figure 4.1. Moreover, the spin axis, $\vec{V}_s$, can be fixed in either the rotating frame or the inertial frame. Next, the modified FM controllers, derived in equations (4.7) and (4.10), will be applied for station-keeping, and the performance of the modified controllers are assessed under the mission design constrains, and operation errors introduced in chapter 3. Table 4.1 summarizes mission specifications, design constraints, and operation errors that are used in this analysis.

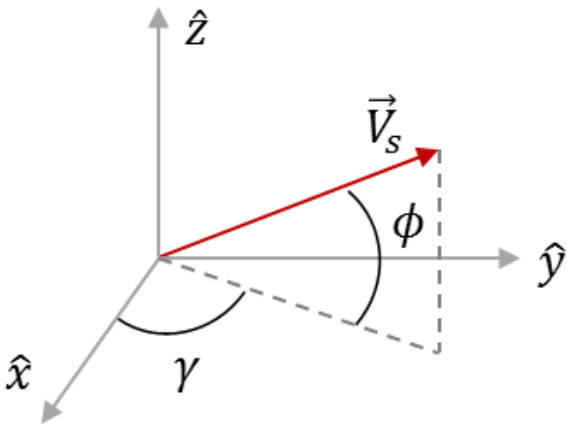


*Figure 4.1. Spin Stabilization Axis*

*Table 4.1. Mission Specifications, Design Constraints, and Operation Errors for the FM Controller*

| | |
|---|---|
| Mission Specifications | - Nominal orbit: $L_1$ southern halo orbit ($A_z$ ~ 223,992 km)<br>- Mission duration: 10 revolutions (~ 5 years)<br>- Spin axis: fixed in the rotating/inertial frame |
| Mission Design Constraints | - Minimum Thrust Level: 0.3 mN<br>- $\Delta t_{min}$: 3 weeks<br>- No corrective maneuver if magnitude of position error vector is decreasing |
| Operation Errors | - Orbit injection and tracking errors: 1-σ errors of 1 km and 1 cm/s<br>- Maneuver execution error: 1-σ error of %1 |

### 4.3.1. Orbital Station-Keeping for a Spin-Stabilized Spacecraft with Tangential Thrusters

The FM controller augmented with a plane constraint on the direction of the corrective maneuvers, as presented in (4.7), can be applied for station-keeping of a spin stabilized spacecraft that is only equipped with tangential thrusters. Such spacecraft can only produce thrust directions that are in a perpendicular plane to the spacecraft's spin axis, $\vec{V}_s$, as illustrated in figure 4.2. For this analysis, the spin axis is assumed to have an in-plane angle, $\gamma$, equal to 57 degrees, and an out-of-plane angle, $\phi$, equal to 15 degrees. These angles are chosen arbitrarily and for demonstration purposes. Additionally, two scenarios are considered where the spin axis, $\vec{V}_s$, is either fixed in the rotating frame, or it is fixed in the inertial frame.

To evaluate the performance of the FM controller in (4.7), a Monte Carlo simulation is conducted and the average station-keeping cost for 10 revolutions of the nominal orbit is calculated. A sample size of 300 trails proves to be sufficient as additional trails do not change the average station-keeping cost significantly. Figure 4.3 shows station-keeping costs for the Monte Carlo simulation conducted for the spin stabilized spacecraft in figure 4.2, with the spin axis fixed in the rotating frame. The blue dots denote the station-keeping

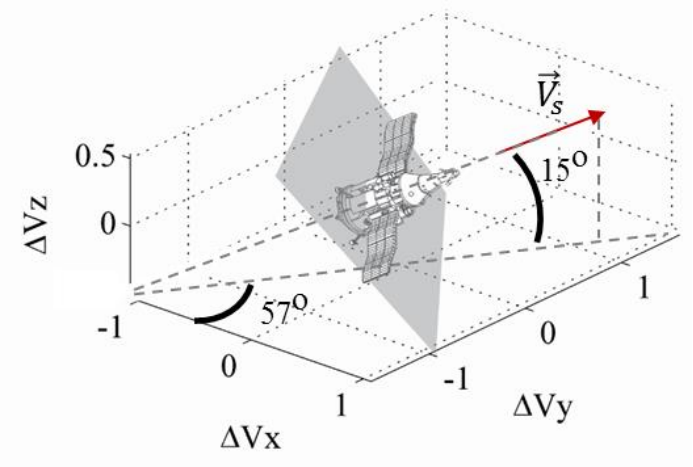


*Figure 4.2. Spin Axis Direction for a Spin Stabilized Spacecraft with Tangential Thrusters*

cost for each individual trails, and the red asterisks denote the moving average of the data up to that point in the simulation. Based on figure 4.3, there is minimal change in the moving average by the end of the 300$^{th}$ trail.

Station-keeping results for a spin stabilized spacecraft with only tangential thrusters and a fixed spin axis in the rotating frame as well as the inertial frame are presented in table 4.2. This table includes the average station-keeping cost, $\Delta\bar{V}_T$, over 10 revolutions around the nominal orbit, and the average cost over one year. An average divergence rate is also calculated which is the slope of a linear curve fit to the time history of the magnitude of the position error vector of the spacecraft relative to the nominal orbit, as illustrated in figure 4.4. The average linear divergence rate indicates whether or not the spacecraft is deviating from the nominal orbit, and how much the deviating rate is per period of the nominal trajectory. The station-keeping results, presented in table 4.2, show no significant differences between the performances of the FM controller with a fixed spin axis in the rotating frame compared to that the inertial frame. The station-keeping costs are roughly in agreement with other published results [11, 12, 15, 18]. However, a meaningful comparison cannot be made as these references do not include the same mission design constraints and operation errors. Furthermore, table 4.4 indicates that the spacecraft may not stay indefinitely around the nominal orbit as the value of the average linear divergence

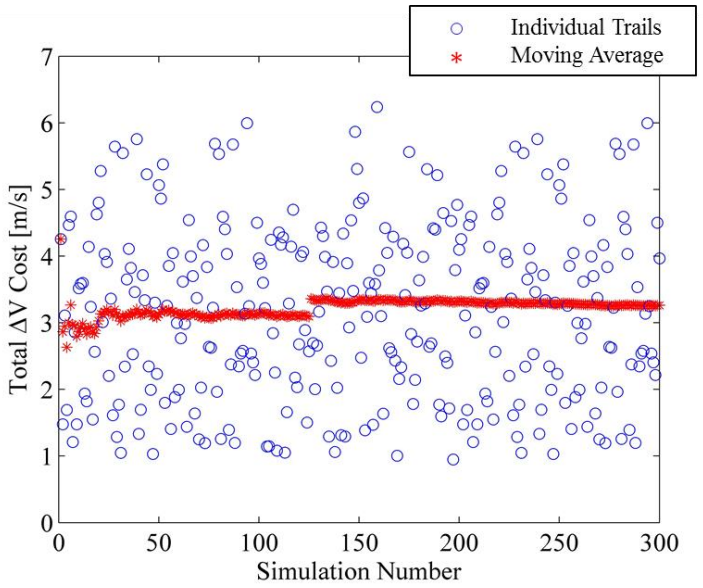


*Figure 4.3. Monte Carlo Simulation (300 Trials)*

rate is positive in both scenarios. In [15], Keeter, too, observed a positive deviation rate using the FM controller, which he associated with the fact that the error vector is calculated based on an isochronous correspondence, and the positive slope of divergence could merely represent a shift along the nominal orbit. This positive divergence rate is further explored in Appendix A by examining the performance of the FM controller with and without operation errors and and mission design constraints. The results from Appendix A indicate that the deviation of the spacecraft is mostly related to the addition of operation errors and mission design constraints on the minimum allowable thrust and $\Delta t_{min}$. These results also suggest that operation errors influence the divergence rate more adversely than the mission design constraints.

For purposes of illustration, figures 4.5 and 4.6 show representative station-keeping trails from the Monte Carlo simulation for a spin stabilized spacecraft with tangential thrusters, with a fixed spin axis in the rotating frame as well as the inertial frame, respectively. This figure includes the controlled trajectory in the rotating frame, the motion relative to the nominal orbit expressed in the three position components as well as the direction and magnitude of the corrective maneuvers.

*Table 4.2. Station-Keeping Performance for a Spin Stabilized Spacecraft with only Tangential Thrusters*

| $\vec{V}_S$ fixed in | $\Delta\bar{V}_T$ for 10 revolutions [m/s] | $\Delta\bar{V}_T$/ year [m/s] | Average Linear Divergence Rate [km/rev] |
|---|---|---|---|
| Rotating Frame | 7.2611 | 1.4237 | +0.0219 |
| Inertial Frame | 7.0682 | 1.3859 | +0.0379 |

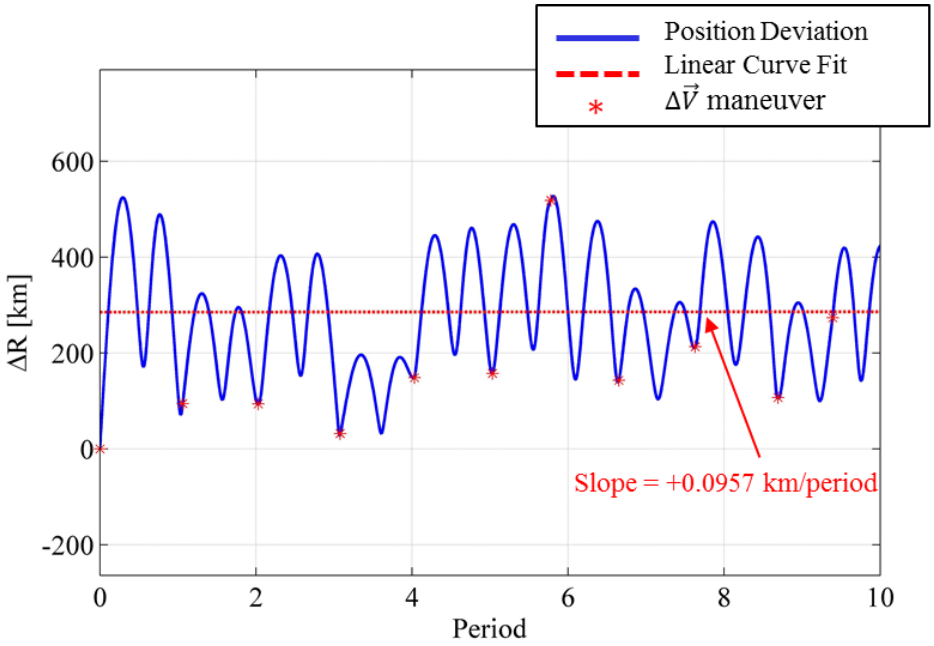


*Figure 4.4. Time History of the Spacecraft's Position Deviation with Respect to the Nominal Orbit (Controlled by FM Controller with a Plane Constraint Fixed in the Inertial Frame)*

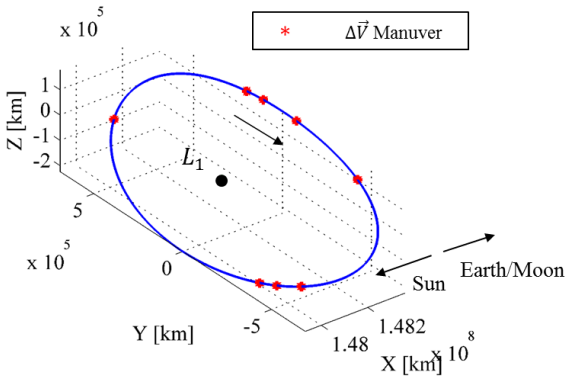


*(a) Controlled $L_1$ Halo Orbit Using the Impulsive FM Controller with a Plane Constraint on $\Delta\vec{V}$*

*(b) Motion Relative to the Reference $L_1$ Halo Orbit*

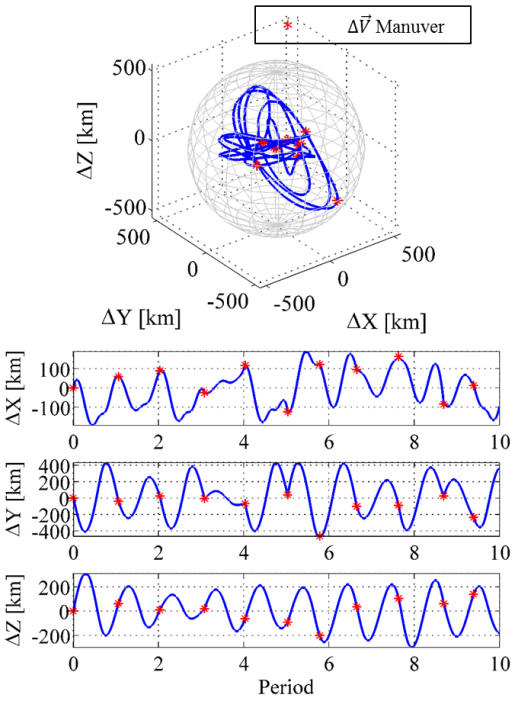


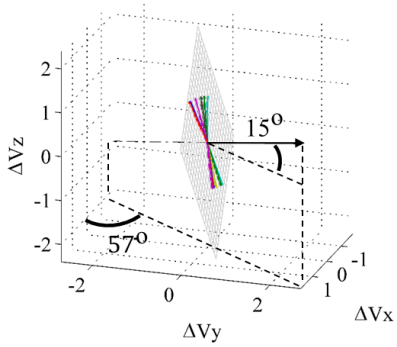


*(c) Directions of $\Delta\vec{V}$ Maneuvers*

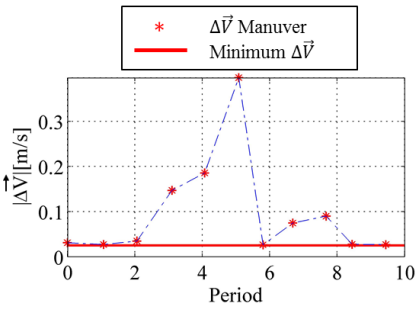


*(d) Magnitude of $\Delta\vec{V}$ Maneuvers*

*Figure 4.5. Orbital Station-Keeping for the Nominal $L_1$ Halo Orbit Using the FM controller for a Spin Stabilized Spacecraft with Tangential Thrusters and a Fixed Spin Axis in the Rotating Frame*

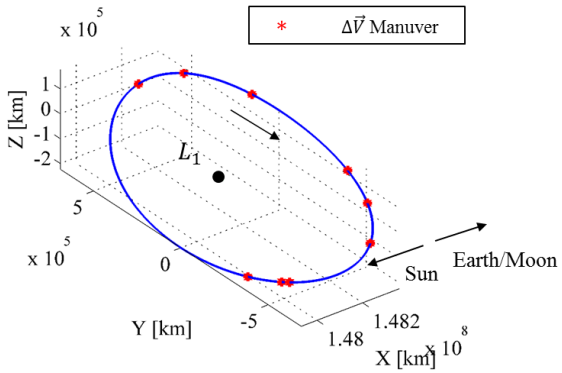


*(a) Controlled $L_1$ Halo Orbit Using the Impulsive FM Controller with a Plane Constraint on $\Delta\vec{V}$*

*(b) Motion Relative to the Reference $L_1$ Halo Orbit*

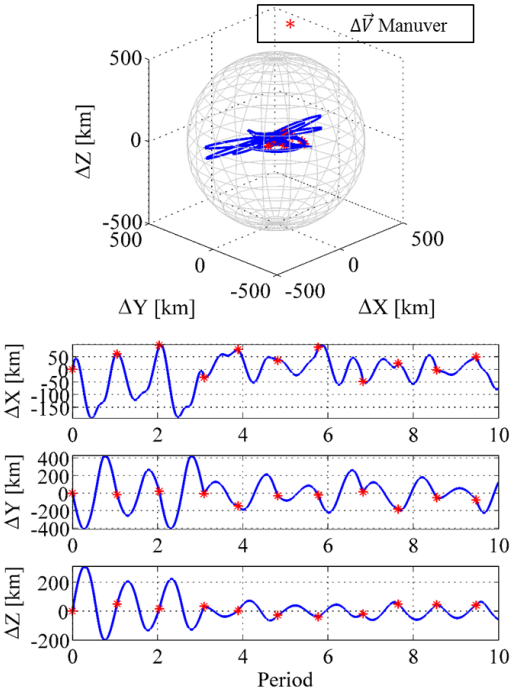


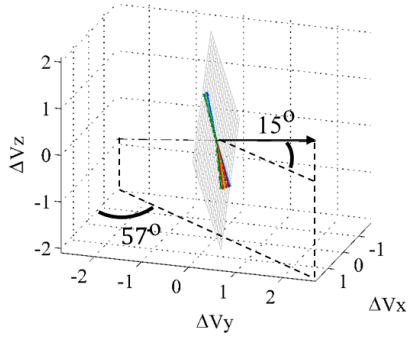


*(c) Directions of $\Delta\vec{V}$ Maneuvers*

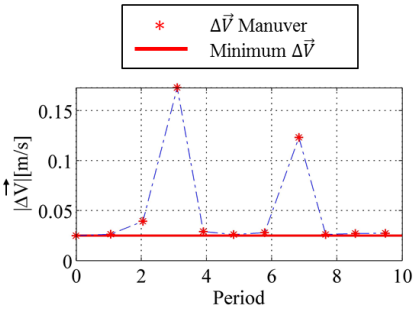


*(d) Magnitude of $\Delta\vec{V}$ Maneuvers*

*Figure 4.6 Orbital Station-Keeping for the Nominal $L_1$ Halo Orbit Using the FM controller for a Spin Stabilized Spacecraft with Tangential Thrusters and a Fixed Spin Axis in the Inertial Frame*

### 4.3.2. Orbital Station-Keeping for a Spin-Stabilized Spacecraft with Axial Thrusters

The FM controller augmented with a line constraint on the direction of the corrective maneuver, as presented in (4.10), can be applied for station-keeping of a spin stabilized spacecraft that is only equipped with axial thrusters. Such spacecraft can only produce thrust directions that are aligned with the spacecraft's spin axis, $\vec{V}_s$, as illustrated in figure 4.7. As in the previous section, the spin axis is assumed to have an in-plane angle, $\gamma$, equal to 57 degrees, and an out-of-plane angle, $\phi$, equal to 15 degrees. Similarly, two scenarios are considered where the spin axis, $\vec{V}_s$, is either fixed in the rotating frame, or it is fixed in the inertial frame. To evaluate the performance of the FM controller in (4.10), a Monte Carlo simulation is conducted and the average station-keeping cost for 10 revolutions of the nominal orbit is calculated. For this simulation, a sample size of 300 trails would also provide a stable moving average of the station-keeping costs.

Table 4.3 summarizes the station-keeping results for a spin stabilized spacecraft with only axial thrusters and a fixed spin axis in the rotating frame as well as the inertial frame.

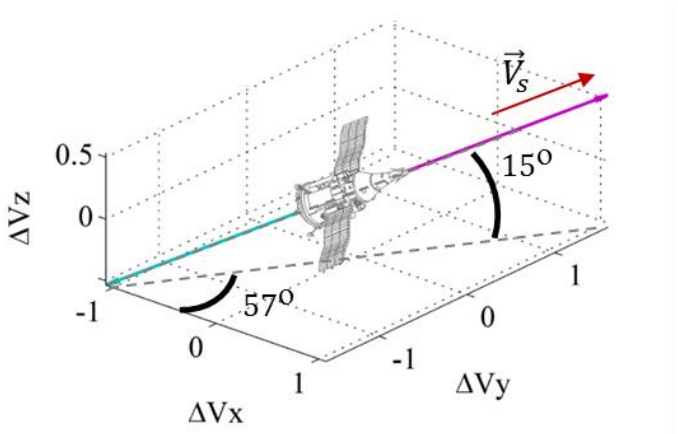


*Figure 4.7. Spin Axis Direction for a Spin Stabilized Spacecraft with Tangential Thrusters*

As in the previous section, the results from this table indicate no significant difference between the station-keeping performances of the FM in the rotating frame compared to the inertial frame. A small positive divergence rate still exists which is mostly related to the

incorporation of operation errors and mission design constraint, as explained in Appendix A. Moreover, the results from tables 4.2 and 4.3, indicate that the average station-keeping cost increases when the corrective maneuvers are constrained to a line compared to the case when they are constrained to a plane. This observation is analogous to the published results by Keeter in [15], where an increase in the total station-keeping cost was observed for an x-axis FM controller compared to a three-axis FM controller. Both results in this study and in [15], suggest that the station-keeping cost of the FM controller increases as more constrained are applied to the corrective maneuvers. Furthermore, comparison between tables 4.2 and 4.3 also shows a slight increase in the spacecraft's divergence rate for a line-constrained FM controller. For purposes of illustration, figures 4.8 and 4.9 show representative station-keeping trails for a spin stabilized spacecraft with tangential thrusters, with a fixed spin axis in the rotating frame as well as the inertial frame, respectively.

*Table 4.3. Station-Keeping Performance for a Spin Stabilized Spacecraft with only Axial Thrusters*

| $\vec{V}_S$ fixed in | $\Delta\bar{V}_T$ for 10 revolutions [m/s] | $\Delta\bar{V}_T$/ year [m/s] | Average Linear Divergence Rate [km/rev] |
|---|---|---|---|
| Rotating Frame | 9.0365 | 1.7718 | +0.2067 |
| Inertial Frame | 8.7457 | 1.7148 | +0.1674 |

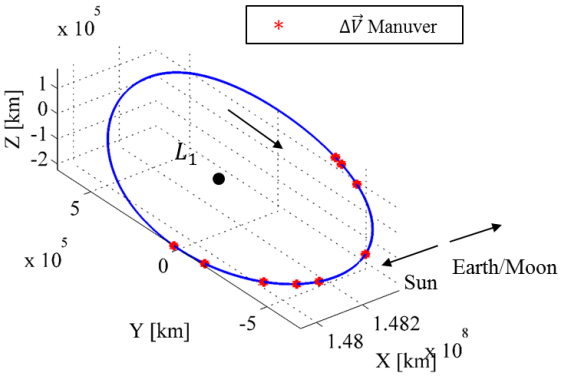


*(a) Controlled $L_1$ Halo Orbit Using the Impulsive FM Controller with a Line Constraint on $\Delta\vec{V}$*

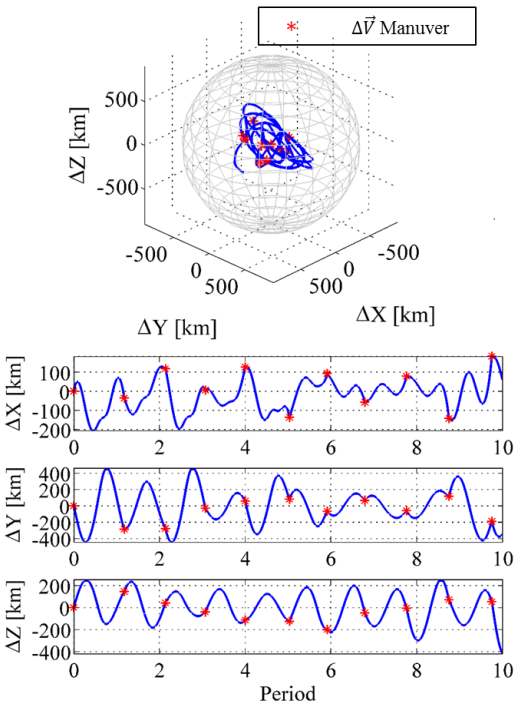


*(b) Motion Relative to the Reference $L_1$ Halo Orbit*

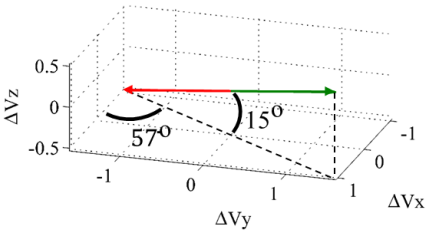


*(c) Directions of $\Delta\vec{V}$ Maneuvers*

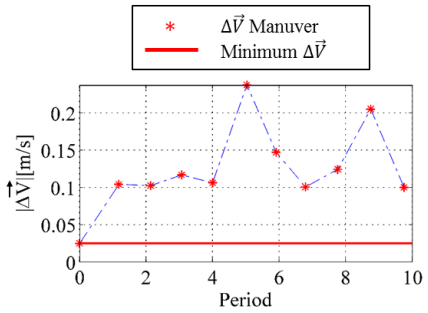


*(d) Magnitude of $\Delta\vec{V}$ Maneuvers*

*Figure 4.8. Orbital Station-Keeping for the Nominal $L_1$ Halo Orbit Using the FM controller for a Spin Stabilized Spacecraft with Axial Thrusters and a Fixed Spin Axis in the Rotating Frame*

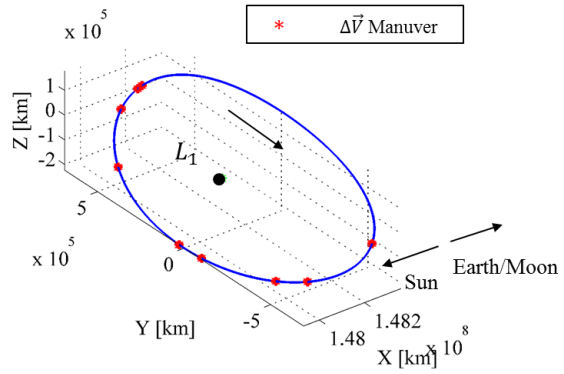


*(a) Controlled $L_1$ Halo Orbit Using the Impulsive FM Controller with a Line Constraint on $\Delta\vec{V}$*

*(b) Motion Relative to the Reference $L_1$ Halo Orbit*

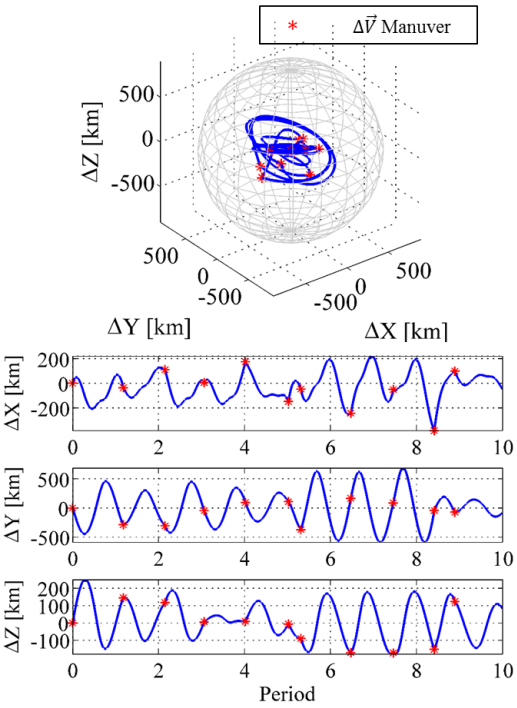


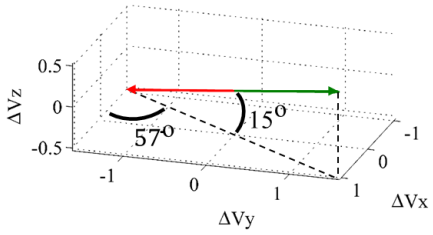


*(c) Directions of $\Delta\vec{V}$ Maneuvers*

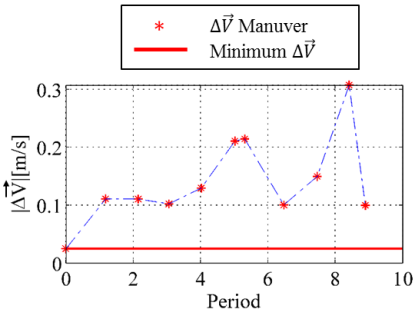


*(d) Magnitude of $\Delta\vec{V}$ Maneuvers*

*Figure 4.9. Orbital Station-Keeping for the Nominal $L_1$ Halo Orbit Using the FM controller for a Spin Stabilized Spacecraft with Axial Thrusters and a Fixed Spin Axis in the Inertial Frame*

# 5. CONTINUOUS HAMILTONIAN STRUCTURE-PRESERVING (HSP) STATION-KEEPING STRATEGY

The Hamiltonian Structure-Preserving (HSP) controller is a state feedback control law that aims to place a spacecraft in an oscillatory motion about a nominal trajectory. Similar to the FM controller, the HSP control strategy is also applicable for formation flight of spacecraft and interferometry imaging. Due to a continuous and low acceleration level produced by this controller, low-thrust propulsion systems can be used for implementation of this controller. In this chapter, the original formulation of the HSP controller is presented, and its limitations are identified. Next, modifications to the original formulation are proposed that are capable of overcoming the identified limitations. A stability analysis, using the Floquet theory, is conducted to assess the stability of the proposed modified HSP controller. Lastly, the modified controller is applied to the nominal halo orbit, presented in chapter 3, and the motion of the spacecraft is simulated in the non-linear dynamics under mission design constraints and operation errors.

## 5.1. HSP Controller Formulation

The HSP control strategy is a state feedback control law that uses the subspaces of the linearized variational equations of motion (i.e. the eigenstructure of $A(t)$ in equation (2.33)). This controller projects the state position error vector along the directions of stable and unstable eigenvectors of $A(t)$. The aim of this controller is to place the poles of the linearized variational equations along the imaginary axis, and create an artificial center manifold that places the spacecraft in an oscillatory motion about the nominal orbit. In [16], Scheeres argues that the proposed HSP controller creates a local bounded stability

that impacts the periodic orbit stability by changing the eigenvalues of the monodromy matrix.

The original HSP controller was proposed for planar periodic orbits. The linearized dynamics relative to a planar periodic trajectory is given by,

$$\dot{\delta\vec{X}}(t) = A(t)\delta\vec{X}(t) = \begin{bmatrix} 0 & I \\ U^*_{RR} & 2K \end{bmatrix}\delta\vec{X}(t) \tag{5.1}$$

Where $K = \begin{bmatrix} 0 & 1 \\ -1 & 0 \end{bmatrix}$, $U^*_{RR} = \begin{bmatrix} U^*_{xx} & U^*_{xy} \\ U^*_{xy} & U^*_{yy} \end{bmatrix}$, and $\delta\vec{X}(t) = \left[\delta\vec{r}\ \dot{\delta\vec{r}}\right]^T$. The poles of the linearized dynamics are given by the characteristic polynomial of $A(t)$,

$$|A(t) - \lambda I| = \lambda^4 + b\lambda^2 + c = \Lambda^2 + b\Lambda + c = 0 \tag{5.2}$$

And the general solutions to the characteristic equation are,

$$\Lambda_1 = \lambda^2_{1,2} = \frac{-b+\sqrt{\Delta}}{2}, \quad \Lambda_2 = \lambda^2_{3,4} = \frac{-b-\sqrt{\Delta}}{2} \tag{5.3}$$

Where $b = 4 - U^*_{xx} - U^*_{yy}, \Delta = b^2 - 4c$, and $c = U^*_{xx}U^*_{yy} - U^{*2}_{xy}$. The original HSP controller was proposed for planar periodic orbits with hyperbolic instability i.e. $\Delta > 0$. These are trajectories in which $A(t)$ possesses couples of real and pure imaginary eigenvalues.

The aim of the HSP controller is to modify the coefficients $b$ and $c$ to ensure that the roots of the characteristic equation (5.2) are placed on the imaginary axis. This will create a locally bounded stable motion, which will also impact onto the periodic orbit stability [16, 18]. The HSP controller is constructed by projecting the position component of the error vector along the directions of both stable and unstable eigenvectors of $A(t)$. Therefore, the control acceleration has the following formulation,

$$\vec{u}(t) = (-\sigma^2 g[\vec{v}_1\vec{v}_1^T + \vec{v}_2\vec{v}_2^T])\delta\vec{r} \tag{5.4}$$

Where $\sigma$ is the unstable eigenvalue of $A(t)$, $g$ is a constant gain parameter, and $\vec{v}_1$ and $\vec{v}_2$ are position components of the unstable and stable eigenvectors of $A(t)$, respectively. $\delta\vec{r}$ is the position component of the error vector between the controlled trajectory and the nominal orbit. Additionally, the controller presented in (5.4) is for a hyperbolic two-dimensional periodic trajectory in which $A(t)$ possesses one real pair and one complex conjugate pair of eigenvalues (i.e. $\Delta > 0$). In [18], Soldini extends this controller for the case when $\Delta < 0$.

Implementing the HSP controller has the effect of modifying the linearized dynamics by changing the Jacobian matrix of the potential acceleration, or $U^*_{RR}$, as follows,

$$\dot{\delta\vec{X}}(t) = A(t)\delta\vec{X}(t) + B\vec{u}(t) \tag{5.5}$$

$$\dot{\delta\vec{X}}(t) = \begin{bmatrix} 0 & I \\ U^*_{RR} - \sigma^2 g[\vec{v}_1\vec{v}_1^T + \vec{v}_2\vec{v}_2^T] & 2K \end{bmatrix}\delta\vec{X}(t) \tag{5.6}$$

$$\dot{\delta\vec{X}}(t) = \begin{bmatrix} 0 & I \\ \widetilde{U}^*_{RR} & 2K \end{bmatrix}\delta\vec{X}(t) = \tilde{A}(t)\delta\vec{X}(t) \tag{5.7}$$

Where $B = \begin{bmatrix} 0 & 0 & 1 & 0 \\ 0 & 0 & 0 & 1 \end{bmatrix}^T$, and $\widetilde{U}^*_{RR} = \begin{bmatrix} \widetilde{U}^*_{xx} & \widetilde{U}^*_{xy} \\ \widetilde{U}^*_{xy} & \widetilde{U}^*_{yy} \end{bmatrix}$. Thus, the characteristic polynomial for the modified dynamics is given by,

$$\left|\tilde{A}(t) - \lambda I\right| = \lambda^4 + \tilde{b}\lambda^2 + \tilde{c} = \Lambda^2 + \tilde{b}\Lambda + \tilde{c} = 0 \tag{5.8}$$

In order for the modified characteristic equation (5.8) to have pure imaginary roots, the following three conditions must hold,

$$\tilde{b}(g,t) = 4 - \widetilde{U}^*_{xx} - \widetilde{U}^*_{yy} > 0 \tag{5.9}$$

$$\tilde{c}(g,t) = \widetilde{U}^*_{xx}\widetilde{U}^*_{yy} - \widetilde{U}^{*2}_{xy} > 0 \tag{5.10}$$

$$\tilde{\Delta}(g,t) = \tilde{b}^2 - 4\tilde{c} > 0 \tag{5.11}$$

These are sufficient conditions for local bounded stability of a planar periodic trajectory with hyperbolic instability. In [16, 17, 18], it is demonstrated that for large enough control gain $g$, conditions (5.9)-(5.11) are satisfied. Lastly, in Appendix B, it is shown that due to the symmetric formulation of this controller, the modified dynamical environment stays an autonomous and Hamiltonian system once the HSP controller is applied. Hence the choice for the name of this controller.

## 5.2. Identifying Limitations of the HSP Controller

The aim of this section is to identify limitations of the HSP controller proposed by Scheeres in [16], and set a groundwork for developing modifications to overcome those limitations. As previously mentioned in section 5.1, the original HSP controller was proposed for station-keeping about planar periodic trajectories with hyperbolic instability, where the eigenstructure of the linearized variational equations of motion in (5.1) possesses couples of real and pure imaginary eigenvalues. Another possibility for the eigenstructure of (5.1) is the case where the eigenvalues are two couples of complex and conjugates pairs. In [18], Soldini has extended the original HSP controller for planar periodic trajectories with such eigenstructure.

Nevertheless, the HSP controllers proposed by previous authors are designed only based on the linearized variational equations for a planar periodic trajectory. These controllers do not guarantee the same stability results for general three dimensional orbits. This is evident by the fact that the characteristic polynomial for the linearized variational equations for a three dimensional periodic trajectory is different from that of a planar trajectory. Therefore, the local bounded stability conditions presented in (5.9)-(5.11) may not be sufficient for achieving local bounded stability in the three dimensional case. In this research effort, a modified HSP controller is proposed that is designed based on the linearized variational equations for a three dimensional periodic trajectory. A new set of conditions are derived to place the poles of the three dimensional linearized variational equations on the imaginary axis.

Additionally, in equation (5.4), the control gain $g$ is assumed to be constant. Under this assumption, the control gain has to be large enough to ensure that equations (5.9)-(5.11) are satisfied throughout the orbit. This will have an adverse effect on the total station-keeping cost due to an unnecessarily high acceleration level produced by the controller. Therefore, a methodology needs to be developed to calculate a time-varying control gain based on the location of the spacecraft around the nominal orbit. A variable-gain HSP controller is expected to have a lower and more efficient total station-keeping cost.

Lastly, previously proposed HSP controllers are designed based on the assumption that the spacecraft is provided with continuous orbital determination information, or that the spacecraft can perform the corrective maneuvers at any time. As explained in section 3.4, there is often a minimum time requirement between station-keeping maneuvers due to scientific observations, or due to the minimum time to achieve an accurate post-burn orbital determination [19]. Under these constraints, the dynamical model is no longer continuous in time, rather it is a discrete-time dynamical model. Therefore, a new HSP controller must be designed for the discretized variational equations of motion.

## 5.3. Modified HSP (MHSP) Controller: Application to 3-D Orbits

Previously proposed HSP controllers were designed based on the linearized variational equations for a planar periodic trajectory. However, the majority of the trajectories used for missions around libration points are three dimensional orbits with out-of-plane excursions. Therefore, the original HSP controller must be extended and modified to be applicable to three dimensional equations of motion.

In this section, a modified HSP controller (MHSP) is proposed that aims to place the poles of the three dimensional linearized variational equations along the imaginary axis. The linearized dynamics relative to a three-dimensional periodic trajectory is given by,

$$\dot{\delta\vec{X}}(t) = A(t)\delta\vec{X}(t) = \begin{bmatrix} 0 & I \\ U^*_{RR} & 2K \end{bmatrix}\delta\vec{X}(t) \tag{5.12}$$

Where $K = \begin{bmatrix} 0 & 1 & 0 \\ -1 & 0 & 0 \\ 0 & 0 & 0 \end{bmatrix}$, $U_{RR}^* = \begin{bmatrix} U_{xx}^* & U_{xy}^* & U^*{}_{xz} \\ U_{xy}^* & U_{yy}^* & U^*{}_{yz} \\ U_{xz}^* & U_{yz}^* & U_{zz}^* \end{bmatrix}$, and $\delta\vec{X}(t) = \left[\delta\vec{r}\ \delta\dot{\vec{r}}\right]^T$. The poles of the linearized dynamics are given by the characteristic polynomial of $A(t)$,

$$|A(t) - \lambda I| = \lambda^6 + b\lambda^4 + c\lambda^2 + d = \Lambda^3 + b\Lambda^2 + c\Lambda + d = 0 \tag{5.13}$$

In order for equation (5.13) to have pure imaginary roots, the following three conditions must hold,

$$b = 4 - U_{xx}^* - U_{yy}^* - U_{zz}^* > 0 \tag{5.14}$$

$$d = |U_{RR}^*| > 0 \tag{5.15}$$

$$\begin{aligned} bc - d = &\left(4 - U_{xx}^* - U_{yy}^* - U_{zz}^*\right) \times \\ &\left(-U^{*2}_{xy} - U^{*2}_{xz} + U_{xx}^* U_{yy}^* - U^{*2}_{yz} - 4U_{zz}^* + U_{xx}^* U_{zz}^* + U_{yy}^* U_{zz}^*\right) \\ &- |U_{RR}^*| > 0 \end{aligned} \tag{5.16}$$

The aim of the MHSP controller is to alter the coefficients of the characteristic polynomial given in (5.13) such that equations (5.14)-(5.16) are satisfied. Following a similar methodology as in the formulation of the original HSP controller, the MHSP controller is designed to be a state feedback control law that projects the position component of the error vector along the directions of the eigenvectors of $A(t)$. However, in the MHSP controller, in addition to projecting the position error vector along the stable and unstable eigenvectors, it is projected along the center subspace eigenvectors as well. In this investigation, the MHSP controller is designed for periodic trajectories in which $A(t)$ possesses two real eigenvalues, two imaginary eigenvalues, and two complex and conjugate eigenvalues. The extension of this controller to other eigenstuctures has not been included in this analysis and is left for future investigations.

Therefore, the control acceleration produced by the MHSP controller has the following formulation:

$$\vec{u}(t) = \left(-\sigma^2 g[\vec{v}_1 v_1^T + \vec{v}_2 \vec{v}_2^T] - \gamma^2 g_c\left[\vec{v}_c \vec{v}_c^T + \vec{\bar{v}}_c \vec{\bar{v}}_c^T\right]\right)\delta\vec{r} \tag{5.17}$$

Where $\gamma$ is the eigenvalue and $\vec{v}_c$ is the position component of the associated eigenvector for one of the center subspaces of $A(t)$. $\vec{\bar{v}}_c$ is the complex conjugate vector of $\vec{v}_c$. $g_c$ is a gain parameter for the center subspace projection tensor.

As in the original HSP controller, implementation of the MHSP controller has the effect of modifying the linearized dynamics by changing the Jacobian matrix of the potential acceleration, $U_{RR}^*$, which impacts the coefficients of the characteristic polynomial in (5.13). This effect is as follows,

$$\delta\dot{\vec{X}}(t) = A(t)\delta\vec{X}(t) + B\vec{u}(t) \tag{5.18}$$

$$\delta\dot{\vec{X}}(t) = \begin{bmatrix} 0 & I \\ U_{RR}^* - \sigma^2 g[\vec{v}_1 v_1^T + \vec{v}_2 \vec{v}_2^T] - \gamma^2 g_c\left[\vec{v}_c \vec{v}_c^T + \vec{\bar{v}}_c \vec{\bar{v}}_c^T\right] & 2K \end{bmatrix}\delta\vec{X}(t) \tag{5.19}$$

$$\delta\dot{\vec{X}}(t) = \begin{bmatrix} 0 & I \\ \widetilde{U}^*{}_{RR} & 2K \end{bmatrix}\delta\vec{X}(t) = \tilde{A}(t)\delta\vec{X}(t) \tag{5.20}$$

Where $= [0_{3\times3} \quad I_{3\times3}]\ \widetilde{U}^*{}_{RR} = \begin{bmatrix} \widetilde{U}_{xx}^* & \widetilde{U}_{xy}^* & \widetilde{U}^*{}_{xz} \\ \widetilde{U}_{xy}^* & \widetilde{U}_{yy}^* & \widetilde{U}^*{}_{yz} \\ \widetilde{U}_{xz}^* & \widetilde{U}_{yz}^* & \widetilde{U}_{zz}^* \end{bmatrix}$. Thus, the characteristic polynomial for the modified dynamics is given by,

$$|A(t) - \lambda I| = \lambda^6 + \tilde{b}\lambda^4 + \tilde{c}\lambda^2 + \tilde{d} = \Lambda^3 + \tilde{b}\Lambda^2 + \tilde{c}\Lambda + \tilde{d} = 0 \tag{5.21}$$

Similar to equations (5.14)-(5.16), in order for equation (5.21) to have pure imaginary roots, the following three conditions must hold for $\tilde{b}$, $\tilde{c}$, and $\tilde{d}$,

$$\tilde{b}(G, G_c, t) = 4 - \widetilde{U}^*_{xx} - \widetilde{U}^*_{yy} - \widetilde{U}^*_{zz} > 0 \tag{5.22}$$

$$\tilde{c}(G, G_c, t) = |\widetilde{U}^*_{RR}| > 0 \tag{5.23}$$

$$\begin{aligned}\tilde{b}\tilde{c} - \tilde{d}(G, G_c, t) = \left(4 - \widetilde{U}^*_{xx} - \widetilde{U}^*_{yy} - \widetilde{U}^*_{zz}\right) \times \ldots \\ \left(-\widetilde{U}^{*2}_{xy} - \widetilde{U}^{*2}_{xz} + \widetilde{U}^*_{xx}\widetilde{U}^*_{yy} - \widetilde{U}^{*2}_{yz} - 4\widetilde{U}^*_{zz} + \widetilde{U}^*_{xx}\widetilde{U}^*_{zz} + \widetilde{U}^*_{yy}\widetilde{U}^*_{zz}\right) \\ - |\widetilde{U}^*_{RR}| > 0\end{aligned} \tag{5.24}$$

In Appendix C, it is demonstrated that equations (5.22)-(5.24) are always satisfied for large enough control gains $g$ and $g_c$.

### 5.3.1. Methodology for Variable-Gain MHSP Controller

Equations (5.22)-(5.24) can also be re-written in terms of $G$ and $G_c$ as follows,

$$g + g_c > \frac{\left(U^*_{xx} + U^*_{yy} + U^*_{zz} - 4\right)}{2} \tag{5.25}$$

$$g_c > \alpha(t)g \tag{5.26}$$

$$g_c > \beta(t)g \tag{5.27}$$

Where $\alpha(t)$ and $\beta(t)$ are time varying, periodic coefficient. The derivation for these equations are presented in Appendix C. Equations (5.25)-(5.27) provide sufficient conditions on the minimum values of the control gains to ensure local bounded stability. Since these conditions are functions of time, they provide a basis for a variable-gain MHSP controller where the control gains $g$ and $g_c$ are chosen based on the location of the spacecraft around the nominal orbit.

### 5.3.2. Performance Comparison between HSP and MHSP Controllers

In this section the station-keeping performance of the original HSP and the MHSP controller are compared. In [16], the original HSP controller is applied for station-keeping around a northern $L_2$ halo orbit. However, as previously mentioned in section 5.2, this controller does not necessarily guarantee the local bounded stability conditions for a three dimensional periodic trajectory, given in (5.22)-(5.24). This can be seen in figure 5.1, where the local bounded stability conditions are assessed after applying the original HSP controller to some members of the northern $L_2$ halo family. It is also important to note that all the halo orbits presented in this figure are hyperbolically unstable i.e. $A(t)$ possesses one real pair of eigenvalues and two imaginary and conjugate pairs. In figure 5.1.(a), blue dots indicate regions where the original HSP controller is capable of satisfying equations (5.22)-(5.24), and therefore local bounded stability is achieved. Moreover, in this figure, the $L_2$ halo orbit presented in [16] is one of the lower $A_z$ amplitude orbits, where the bounded stability conditions are satisfied throughout the entire orbit. Red dots, on the other hand, indicate regions where the original HSP controller does not satisfy the bounded stability conditions. From figure 5.1, these regions of instability occur around the maximum z-excursion of the higher amplitude halo orbits. In figure 5.1.(b), the station-keeping result is shown for the highest amplitude member of the $L_2$ halo family in 5.1.(a). This simulation is done using the non-linear dynamics, under an initial random perturbation (1-$\sigma$ error of 1km and 1 cm/s in position and velocity), and propagated for approximately two revolutions about the nominal orbit. As predicted by the linear stability analysis in 5.1.(a), the original HSP controller is not able to maintain the motion of the spacecraft in the vicinity of this high amplitude nominal orbit.

A similar set of analyses is conducted for the MHSP controller. In figure 5.2.(a), the local bounded stability conditions in (5.22)-(5.24) are assessed under the implementation of the MHSP controller. Figure 5.2.(a) shows that this controller is capable of satisfying equations (5.22)-(5.24) throughout the presented members of the $L_2$ halo family. In figure 5.2.(b), the MHSP controller is applied to the same halo orbit as in 5.1.(b), for 10 revolutions around the nominal orbit, and under the same random initial perturbation. The

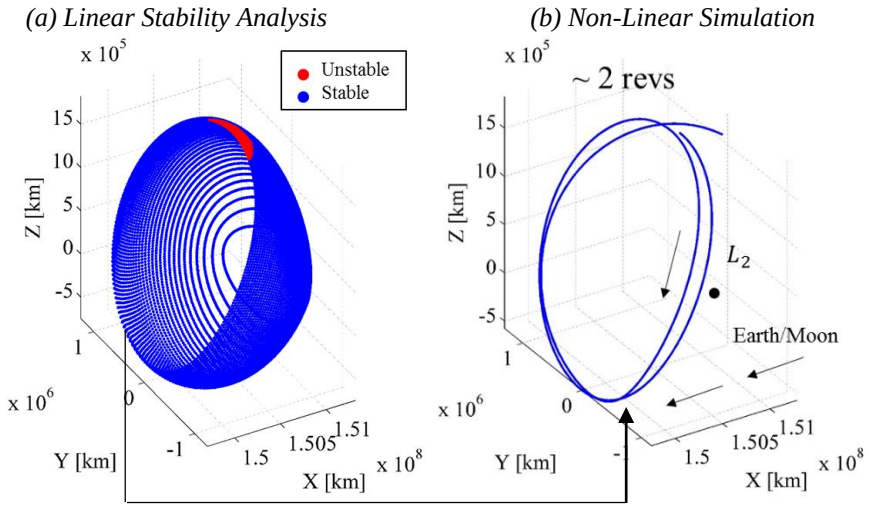


*Figure 5.1. Station-Keeping Performance of the Original HSP Controller Using Linear Stability Analysis and Non-Linear Simulation*

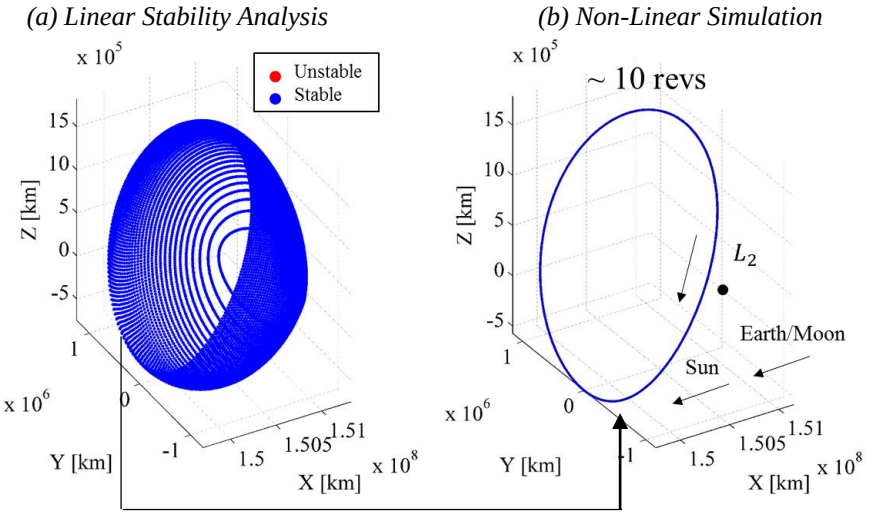


*Figure 5.2. Station-Keeping Performance of the MHSP Controller Using Linear Stability Analysis and Non-Linear Simulation*

control gains $g$ and $g_c$ are chosen to be constant and equal to 20 and 100, respectively. This non-linear simulation shows that the modified controller improves the performance of the original HSP controller, and is successful in maintaining the spacecraft in the vicinity of the high amplitude nominal orbit throughout the duration of the simulation.

### 5.3.3. Performance Comparison between Constant-Gain HSP and Variable-Gain MHSP Controllers

Equations (5.25)-(5.27) are sufficient conditions on the minimum values of the control gains $g$ and $g_c$ to provide local bounded stability in the linearized dynamics. Using these conditions a time-varying, periodic set of control gains can be obtained. The station-keeping performance for the variable-gain MHSP controller is then compared with the constant-gain MHSP controller. For this comparison, nominal orbit is chosen to be the same high amplitude $L_2$ halo orbit used in the previous section as in figures 5.1 and 5.2.

Applying equations (5.25)-(5.27) to this nominal orbit, will result in a minimum boundary for the values of the control gains $g$ and $g_c$. Figure 5.3 shows the calculated minimum boundary on the control gains for the nominal halo orbit. Values of $g$ and $g_c$ chosen above the minimum boundary curves will guarantee that local bounded stability conditions, given in equations (5.22)-(5.24), are satisfied. Note that equations (5.25)-(5.27) are time-periodic, and they can be calculated for only one period and used for the duration of the simulation. In figure 5.3, dashed lines indicate the lower boundary on the control gains, and the solid lines indicate the chosen values for the control gains. To compare the station-keeping performance under a constant and a variable-gain MHSP controller, total station-keeping cost for 10 revolutions (~ 5 years) around the nominal orbit is calculated using both control strategies. For the constant-gain MHSP controller, control gains $g$ and $g_c$ are chosen to be equal to 5 and 20, respectively. Compared with figure 5.3, these constant control gains are large enough to ensure that the local bounded stability conditions are satisfied throughout the orbit. In this comparison, an initial random injection error is applied, which is a 1-$\sigma$ error of 1 km and 1 cm/s in position and velocity, respectively. Mission design constraint and other operation errors are not included in this comparison, as the aim is to understand the influence of a time-varying control gain on the station-keeping performance of the MHSP controller. Furthermore, since a random injection error is used, a Monte Carlo simulation of 300 trials is conducted to take the average of the overall station-keeping cost for both controllers. In this Monte Carlo simulation, 300 trails

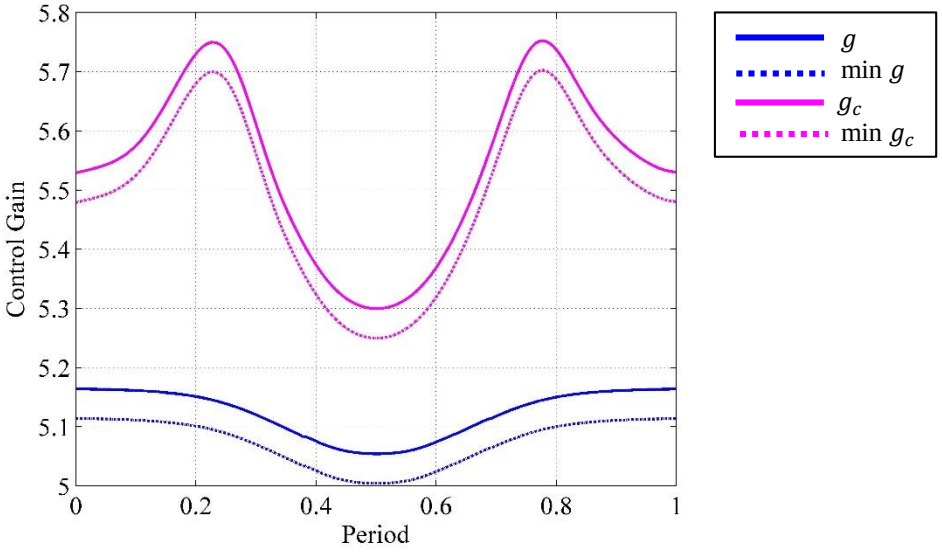


Figure 5.3. Variable Control Gains for the MHSP Controller

will provide a suitable sample size as it ensures a minimal change in the moving average of the total station-keeping cost. Table 5.1, shows the station-keeping performance for the constant-gain and the variable-gain MHSP controllers. This table includes the average total station-keeping cost, $\Delta\bar{V}_T$, over 10 revolutions around the nominal orbit, as well as the average cost over one year. The average linear divergence rate is also included. The linear divergence rate is calculated based on the slope of a linear fit to the spacecraft's position error vector relative to the nominal orbit. According to the results shown in table 5.1, a variable-gain MHSP controller has a more fuel efficient total station-keeping cost. This is most likely due to the fact that the chosen constant control gains for a constant-gain MHSP controller would need to be large enough to ensure that equations (5.22)-(5.24) are satisfied throughout the entire nominal orbit. Consequently, the larger the control gains the higher the control acceleration, which will effectively increase the overall station-keeping cost. Furthermore, table 5.1 shows that both control strategies have a small positive linear divergence rate, which is in the order of meters per revolution. This positive slope of deviation indicates that the spacecraft may not stay indefinitely in the vicinity of the nominal orbit. As further explored in Appendix A, the underlying reason for this deviation

*Table 5.1. Station-Keeping Performance Comparison for the Constant and Variable-Gain MHSP Controllers (300 trials)*

| | $\Delta\bar{V}_T$ for 10 revolutions [m/s] | $\Delta\bar{V}_T$/ year [m/s] | Average Linear Divergence Rate [km/rev] |
|---|---|---|---|
| Constant-Gain MHSP Controller | 47.7301 | 9.3588 | +0.0031 |
| Variable-Gain MHSP Controller | 31.8948 | 6.2538 | +0.0024 |

is most likely due to the fact that the HSP controller aims to achieve local bounded stability in the linearized dynamics, which does not necessarily guarantee a bounded stability in the non-linear dynamics. This diverging behaviour was also acknowledged by Scheeres [16] and Soldini [17]. Nevertheless, by using an HSP controller the decay of the spacecraft is no longer exponential, as in an uncontrolled motion, rather the spacecraft undergoes a slow polynomial decay.

## 5.4. Discrete-Time MHSP Controller

So far, the dynamical system under consideration has been continuous in time. In reality the spacecraft operates in a discrete-time dynamical environment due to the minimum time constraint to obtain an accurate orbit determination, or due to the time requirements for scientific operations. Therefore, the MHSP controller must be re-designed for a discrete-time dynamical system. However, a direct approach does not exist to design the discrete-time controller as the MHSP controller was never derived, rather it was proposed. Therefore, the discrete-time MHSP controller will be designed based on an approximation from the continuous-time controller.

The discrete-time variational equations relative to a reference trajectory is given by,

$$\delta\vec{X}_{k+1} = A_{D_k}\delta\vec{X}_k \tag{5.28}$$

Where $\delta\vec{X}_k$ is the state error vector at time $t_k$, and,

$$A_{D_k} = e^{\int_{t_k}^{t_{k+1}} A(\tau)d\tau} = \Phi(t_{k+1}, t_k) \tag{5.29}$$

Where $t_{k+1} = t_k + \Delta t_k$, and $\Delta t_k$ is the discretization time step or the sampling time in the discrete-time system. The poles of the discrete-time linearized dynamics are given by the roots of the characteristic polynomial,

$$\left|A_{D_k} - \omega I\right| = \omega^6 + b\omega^5 + c\omega^4 + d\omega^3 + e\omega^2 + \omega + g = 0 \tag{5.30}$$

To design an MHSP controller for the discrete-time system, the same methodologies will be used as in the continuous-time system. Therefore, the discrete-time controller aims to achieve local bounded stability by placing the poles of the discrete-time linearized variational equations, i.e. the roots of equation (5.30), on the unitary circle of the complex plane. The discrete-time MHSP controller is also constructed by projecting the position component of the error vector along the directions of the eigenvectors of $A_{D_k}$. Furthermore, due to the fact that the discrete-time dynamics converges to the continuous-time dynamics as the discretization time step, $\Delta t_k$, approaches zero; the discrete-time controller must also converge to the continuous-time controller as $\Delta t_k$ approaches zero. That is,

$$\lim_{\Delta t_k \to 0} \vec{u}_k = \vec{u}(t) \tag{5.31}$$

To ensure that (5.31) holds, the following relationships between the eigenstructure of $A_{D_k}$ and $A(t)$ are exploited to construct the discrete-time MHSP controller. These relationships are derived from a first order Taylor series expansion of equation (5.29),

$$\lim_{\Delta t_k \to 0} eigenvectors\left(A_{D_k}\right) = eigenvectors\left(A(t)\right) \tag{5.32}$$

$$\lim_{\Delta t_k \to 0} \frac{ln(\omega_i)}{\Delta t_k} = \lambda_i \tag{5.33}$$

Where $\omega_i$ is an eigenvalue of $A_{D_k}$, and $\lambda_i$ is an eigenvalue of $A(t)$. By using equations (5.31), (5.32) and (5.33), the following is proposed as the discrete-time MHSP controller,

$$\vec{u}_k = \left(-\sigma_k^2 g\left[\vec{v}_{1_k}\vec{v}_{1_k}^T + v_{2_k}\vec{v}_{2_k}^T\right] - \gamma_k^2 g_c\left[\vec{v}_{c_k}\vec{v}_{c_k}^T + \vec{\bar{v}}_{c_k}\vec{\bar{v}}_{c_k}^T\right]\right)\delta\overrightarrow{r_k} \tag{5.34}$$

Where $\sigma_k = \frac{ln(\omega_1)}{\Delta t_k}$ and $\omega_1$ is the unstable eigenvalue of $A_{D_k}$. $\vec{v}_{1_k}$ and $\vec{v}_{2_k}$ are position components of the unstable and stable eigenvectors of $A_{D_k}$, respectively. $\gamma_k = \frac{ln(\omega_c)}{\Delta t_k}$ where $\omega_c$ is one of the center eigenvalues of $A_{D_k}$, and $\vec{v}_c$ is the associated eigenvector.

As in the continuous-time MHSP controller, implementation of the discrete-time controller impacts the coefficients of the characteristic polynomial in (5.30). This effect is as follows,

$$\delta\vec{X}_{k+1} = A_{D_k}\delta\vec{X}_k + B_{D_k}\vec{u}_k \tag{5.35}$$

$$\delta\vec{X}_{k+1} = (A_{D_k} + \cdots \tag{5.36}$$
$$B_{D_k}\left(\left[\left(-\sigma_k^2 g\left[\vec{v}_{1_k}\vec{v}_{1_k}^T + v_{2_k}\vec{v}_{2_k}^T\right] - \gamma_k^2 g_c\left[\vec{v}_{c_k}\vec{v}_{c_k}^T + \vec{\bar{v}}_{c_k}\vec{\bar{v}}_{c_k}^T\right]\right) 0_{3\times 3}\right]\right)\delta\vec{X}_k$$

$$\delta\vec{X}_{k+1} = \widetilde{A_{D_k}}\delta\vec{X}_k \tag{5.37}$$

Where $B_D = \int_{t_k}^{t_{k+1}} \Phi(t_{k+1},\tau)\, B d\tau$. Then, the characteristic polynomial for the modified dynamics is given by,

$$\left|\widetilde{A_{D_k}} - \omega I\right| = \omega^6 + \tilde{b}\omega^5 + \tilde{c}\omega + \tilde{d}\omega^3 + \tilde{e}\omega^2 + \tilde{f}\omega + \tilde{g} = 0 \tag{5.38}$$

In order for the discrete-time MHSP controller to achieve local bounded stability, control gains $g$ and $g_c$ must be chosen such that all the roots of equation (5.38) are placed on the unitary circle. The following equations governs the choice of $g$ and $g_c$,

$$f_i:\ \omega_i\bar{\omega}_i(g, g_c, t_k, \Delta t_k) - 1 = 0, \qquad i = 1,2,..,6 \tag{5.39}$$

By solving equations (5.39) at each time $t_k$ and step size $\Delta t_k$, a set of control gains $(g, g_c)$ can be determined to ensure that all the roots of the characteristic polynomial (5.38) have a magnitude equal to one. Equations (5.39) are also periodic in time and the resultant control gains will be periodic as well.

## 5.5. Stability of the Controlled Linear System

In this section a methodology is presented to assess the impact of the MHSP controller on the stability of the periodic orbit. Under the hypothesis of Floquet theory, a time-varying periodic linearized dynamics, such as equation (5.1), can be transformed to a time-invariant linear system with constant coefficients [29]. Through the following linear transformation,

$$\vec{\eta}(t) = E^{-1}(t)\delta\vec{X}(t) \tag{5.40}$$

the linearized time-varying system,

$$\delta\dot{\vec{X}}(t) = A(t)\delta\vec{X}(t) \tag{5.41}$$

is transformed to the following linear time-invariant system,

$$\dot{\vec{\eta}}(t) = J\vec{\eta}(t) \tag{5.42}$$

Where $E(t)$ is the periodic Flouqet modal matrix. $J$ is a diagonal matrix containing the Poincare exponents as its diagonal entries. Poincare exponents include the stability information associated with the periodic trajectory in the linearized sense. By applying the linear transformation in (5.40) to the following state feedback controlled linear system,

$$\delta\dot{\vec{X}}(t) = A(t)\delta\vec{X}(t) + B\vec{u}(t) = [A(t) + BK(t)]\delta\vec{X}(t) \tag{5.43}$$

equation (5.43) will transform to the following linear system,

$$\dot{\vec{\eta}}(t) = [J + E^{-1}(t)BK(t)]\vec{\eta}(t) \tag{5.44}$$

Where the eigenvalues of $[J + E^{-1}(t)BK(t)]$, i.e. the modified Poincare exponents, will contain stability information associated with the controlled linear system.

## 5.6. Simulation Results

In this section, the discrete-time MHSP controller, proposed in section 5.4, is applied for station-keeping in the non-linear dynamics around the nominal $L_1$ halo orbit. The goal of this analysis is to assess the station-keeping performance for the discrete-time MHSP controller under the mission design constraints and operation errors introduced in chapter 3. Table 5.2 summarizes mission specifications, design constraints, and operation errors that is tended to be used for this simulation.

Firstly, suitable control gains must be selected that would ensure the discrete-time local bounded stability conditions in (5.39) are satisfied. System of equations in (5.39) is a non-linear over-constrained set of equations which can be solved through a least squares optimization as follows,

*Table 5.2. Mission Specifications, Design Constraints, and Operation Errors for the MHSP Controller*

| | |
|---|---|
| Mission Specifications | - Nominal orbit: $L_1$ southern halo orbit ($A_z$ ~ 223,992 km)<br>- Mission duration: 10 revolutions (~ 5 years) |
| Mission Design Constraints | - Minimum Thrust Level: 0.3 mN<br>- $\Delta t_{min}$: 3 weeks<br>- No corrective maneuver if magnitude of position error vector is decreasing |
| Operation Errors | - Orbit injection and tracking errors: 1-σ errors of 1 km and 1 cm/s<br>- Maneuver execution error: 1-σ error of %1 |

$$\vec{F} = \begin{bmatrix} f_1: \ \omega_1\bar{\omega}_1(g, g_c, t_k, \Delta t_k) - 1 \\ f_2: \ \omega_2\bar{\omega}_2(g, g_c, t_k, \Delta t_k) - 1 \\ f_2: \ \omega_3\bar{\omega}_3(g, g_c, t_k, \Delta t_k) - 1 \\ f_3: \ \omega_4\bar{\omega}_4(g, g_c, t_k, \Delta t_k) - 1 \\ f_4: \ \omega_5\bar{\omega}_5(g, g_c, t_k, \Delta t_k) - 1 \\ f_5: \ \omega_6\bar{\omega}_6(g, g_c, t_k, \Delta t_k) - 1 \end{bmatrix} \tag{5.45}$$

At each time $t_k$ and for a step size $\Delta t_k$, control gains $g$ and $g_c$ are chosen such that the 2-norm of $\vec{F}$ is minimized. That is,

$$\min_{g, g_c} || \vec{F}||_2^2 = \min_{g, g_c}(f_1^2 + f_2^2 + \cdots + f_6^2) \tag{5.46}$$

The desired outcome of this optimization problem is the choice of $g$ and $g_c$ that would result in $|| \vec{F}||_2^2 = 0$, regardless of the values of $t_k$ and $\Delta t_k$. Nevertheless, this may not always be the outcome. Without loss of generality $t_k$ is set to $t_0$, as illustrated in the figure 5.4. The optimization problem (5.46) is then solved for different values of $\Delta t_k$. Figure 5.5 shows the minimum value of $|| \vec{F}||_2^2$ at $t_k = t_0$ for increasing values of $\Delta t_k$. This figure suggests that for small discretization time steps (less than 2 hours), the discrete-time MHSP controller is capable of satisfying the discrete-time local bounded stability conditions at $t_k = t_0$, since $|| \vec{F}||_2^2 = 0$ (with numerical tolerance of $10^{-12}$). However, for $\Delta t_k$ values larger than 2 hours, the minimum value of $|| \vec{F}||_2^2$ increases which indicates that the discrete-time controller does not satisfy the local bounded stability conditions anymore. Despite of this limitation, it is still possible to find an optimal set of control gains by solving the optimization problem (5.46) that does not necessarily satisfy the discrete-time local bounded stability conditions in (5.39), but it does offer an improvement on the stability of the nominal orbit. This effect can be seen by analyzing the stability of the controlled linear dynamics using the method developed in section 5.5.

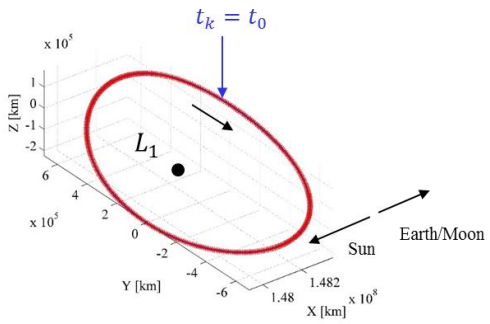


*Figure 5.4. Location of $t_0$ on the nominal orbit*

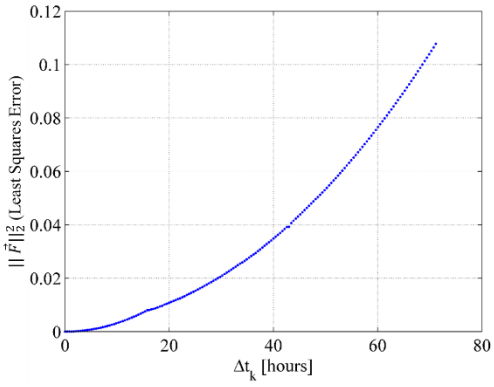


*Figure 5.5. $||\vec{F}||_2^2$ at $t_0$ as a function of discretization step size*

By solving the optimization problem (5.46) throughout the orbit and for a specified step size $\Delta t_k$, optimal sets of control gains $g$ and $g_c$ are computed for the entire orbit. Using these optimal control gains in the discrete-time MHSP controller, the stability of the controlled linear system can then be analyzed by evaluating the modified Poincare exponents from equation (5.44). Figure 5.6 shows the values of the optimal control gains calculated for a discretization step size, $\Delta t_k$, equal to 1 hour. Poincare exponents of the nominal orbit as well as the modified Poincare exponents are plotted in figure 5.7. From this figure, the nominal orbit possesses two pairs of pure real and imaginary Poincare exponents as well as two pairs of zero Poincare exponents, which are shown in red dots. The existence of the real and positive Poincare exponent indicates that the nominal orbit is unstable. On the other hand, the modified Poincare exponents by the discrete-time MHSP controller are all located on the imaginary axis which are shown in blue. Therefore, the modified linear system is bounded stable which is the aim of the MHSP controller. However, as discretization step size increases the discrete-time controller is no longer able to place the Poincare exponents on the imaginary axis, which corresponds to the fact that the discrete-time controller is not able to satisfy the local bounded stability conditions when $\Delta t_k$ is larger than 1 hour. Figures 5.8 and 5.10 show the optimal control gains for the discrete-time MHSP controller calculated for $\Delta t_k$ equal to 48 hours and 3 weeks, respectively. Figures 5.9 and 5.11 show the associated modified Poincare exponents by the

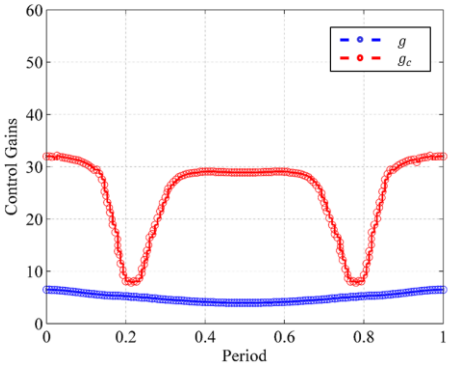


*Figure 5.6. Optimal Control Gains for $\Delta t_k$ = 1 hour*

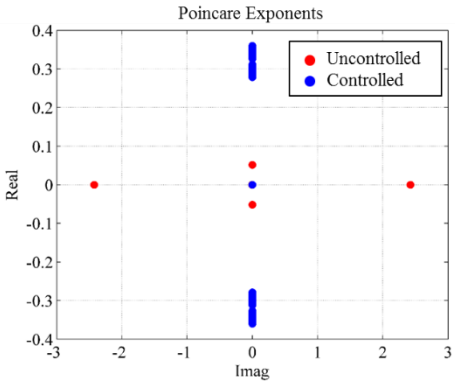


*Figure 5.7. Poincare Exponents of the Controlled and Uncontrolled Linear System ($\Delta t_k$ = 1 hour)*

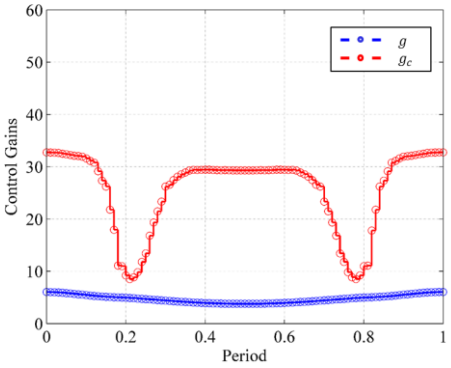


*Figure 5.8. Optimal Control Gains for $\Delta t_k$ = 48 hours*

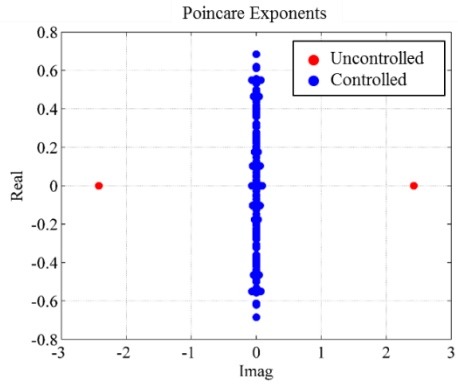


*Figure 5.9. Poincare Exponents of the Controlled and Uncontrolled Linear System ($\Delta t_k$ = 48 hours)*

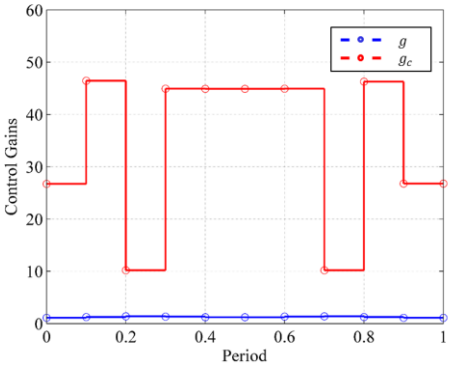


*Figure 5.10. Optimal Control Gains for $\Delta t_k$ = 3 weeks*

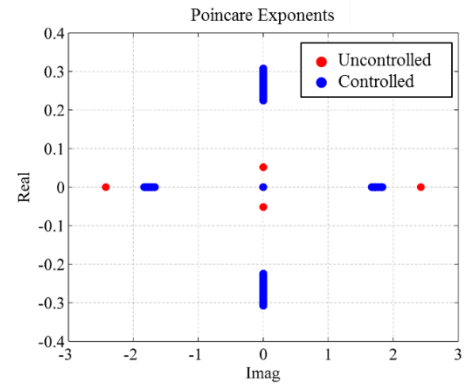


*Figure 5.11. Poincare Exponents of the Controlled and Uncontrolled Linear System ($\Delta t_k$ = 3 weeks)*

discrete-time MHSP controller. These figures indicate that although the discrete-time controller is not able to place the Poincare exponents on the imaginary axis, the stability of the orbit has improved in the linear sense as the magnitude of the positive Poincare exponent has decreased. Such improvement in the linear stability can also be verified by non-linear simulations.

The discrete-time MSHP controller is then applied for station-keeping around the nominal $L_1$ halo orbit. The simulations are done in the non-linear dynamics, using mission specifications, design constraints and operation errors listed in table 5.2. As in the linear stability analysis, the station-keeping performance for three discretization step sizes are evaluated: $\Delta t_k$ = 1 hour, $\Delta t_k$ = 48 hours, and $\Delta t_k$ = 3 weeks. For each case, control gains are chosen based on the optimal values plotted in figures 5.6, 5.8 and 5.10, respectively. A Monte Carlo simulation of 300 trials is conducted to evaluate the average station-keeping costs. A sample size of 300 is sufficient to ensure that there is minimal change in the moving average of the total station-keeping costs.

The average station-keeping cost for 10 revolutions of the nominal orbit and the average cost per year as well as the linear divergence rate from the nominal orbit for $\Delta t_k$ equal to 1 hour and $\Delta t_k$ equal to 48 hours are presented in table 5.3. For purposes of illustration, figures 5.12 and 5.13 show representative station-keeping trails from the Monte Carlo simulations for $\Delta t_k$ equal to 1 hour and $\Delta t_k$ equal to 48 hours, respectively. These figures include the controlled nominal orbit in the rotating frame, the acceleration history of the discrete-time MHSP controller, and the motion relative to the nominal orbit expressed in the three position components as well as the distance between the spacecraft

*Table 5.3. Station-Keeping Performance for the Discrete-Time MHSP Controller with $\Delta t_k$ = 1 hour and $\Delta t_k$ = 48 hours (300 trials)*

| | $\Delta \bar{V}_T$ for 10 revolutions [m/s] | $\Delta \bar{V}_T$/ year [m/s] | Average Linear Divergence Rate [km/rev] |
|---|---|---|---|
| $\Delta t_k$ = 1 hour | 8.6127 | 2.6381 | +2.5991 |
| $\Delta t_k$ = 48 hours | 29.1516 | 3.0126 | +14.6609 |

and the nominal orbit over time. In figures 5.12(a) and 5.13(a), blue lines indicate parts of the trajectory where the controller is on, and magenta lines correspond to parts of the trajectory where controller is turned off since either the mission design constraints (minimum thrust level and $\Delta t_{min}$) are not satisfied, or the magnitude of the position error vector is not increasing.

These results show that the total station-keeping cost and the linear divergence rate increase as discretization step size, $\Delta t_k$, increases from 1 hour to 48 hours. These results are also in agreement with the predications from the linear stability analysis in figures 5.7 and 5.9. Additionally, although the linear stability analysis in figure 5.7 indicates that the modified linearized system with $\Delta t_k$ equal to 1 hour is bounded stable, the average linear divergence rate is positive. As explained in Appendix A, this positive slope of divergence is due to the following two reasons. One contributing factor is that local bounded stability in the linearized dynamics does not guarantee bounded stability in the non-linear dynamics. Another contributing factor is the incorporation of operation errors and mission constraints which seem to accelerate the deviation rate. However, despite of the deviation of the spacecraft, the MHSP controller is able maintain the spacecraft in the vicinity of the nominal orbit for the duration of the mission, and create a spiral-like motion around the nominal trajectory which has variety applications in formation flight of spacecraft and interferometry imaging.

A Monte Carlo simulation was also conducted for station-keeping with discretization step size of 3 weeks. However, in none of the 300 trials the discrete-time MHSP controller was able to maintain the spacecraft in the vicinity of the nominal orbit for 10 revolutions. Instead, for these trails the average divergence time was calculated and compared with the average divergence time of the uncontrolled motion under an initial random injection error. In this analysis, divergence time is defined as the time that the magnitude of the position error vector of the spacecraft relative to the nominal orbit reaches 10,000 km. These results are shown in table 5.4. Figure 5.14 is a representative simulation out of the 300 conducted trials. In this figure, the red line shows the deviation of the uncontrolled motion which has an exponential growth. The blue and magenta line shows the controlled motion under the discrete-time MHSP controller with $\Delta t_k$ equal to 3 weeks, where blue lines indicate regions

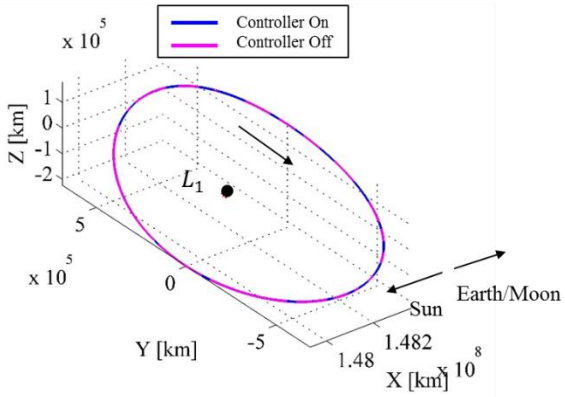


*(a) Controlled $L_1$ Halo Orbit Using the Discrete-time MHSP Controller*

*(b) Motion Relative to the Reference $L_1$ Halo Orbit*

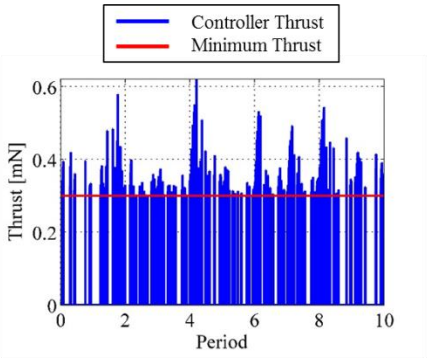


*(c) Thrust Acceleration History by the Discrete-time MHSP.*

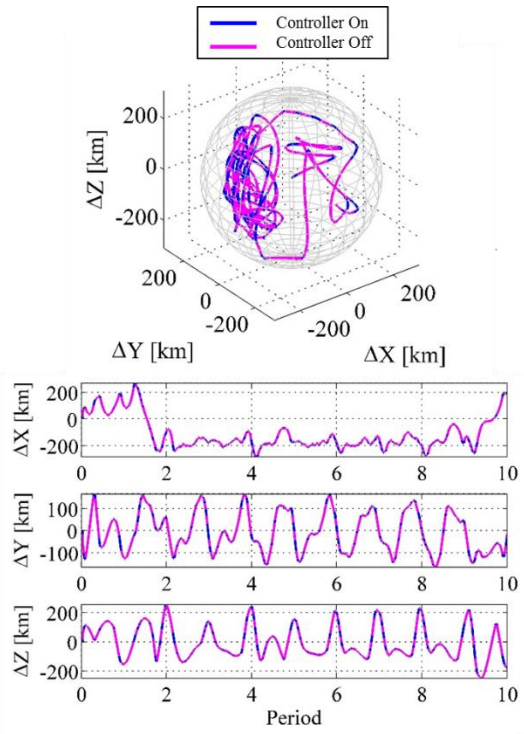


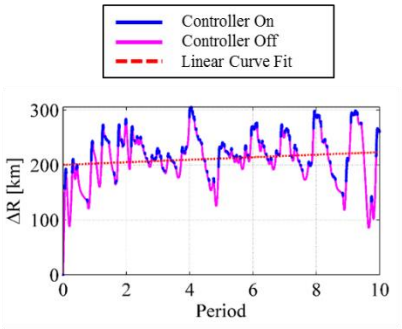


*(d) Magnitude of the Position Error Vector*

*Figure 5.12. Orbital Station-Keeping for the Nominal $L_1$ Halo Orbit Using the Discrete-time MHSP Controller ($\Delta t_k$ = 1 hour)*

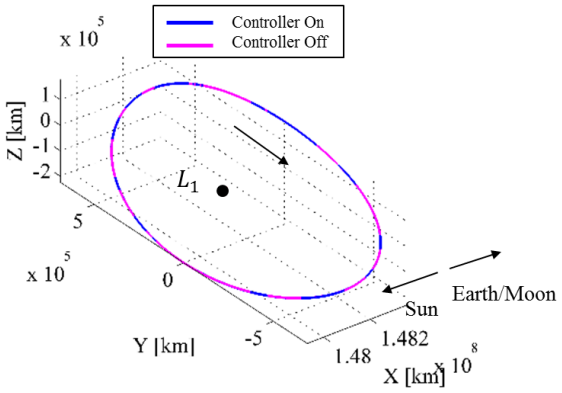


*(a) Controlled $L_1$ Halo Orbit Using the Discrete-time MHSP Controller*

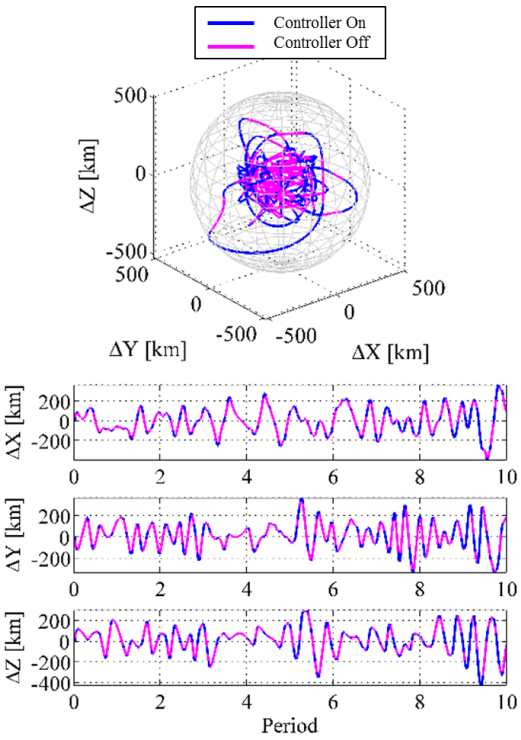


*(b) Motion Relative to the Reference $L_1$ Halo Orbit*

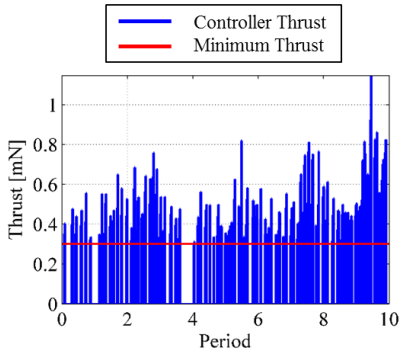


*(c) Thrust Acceleration History by the Discrete-time MHSP.*

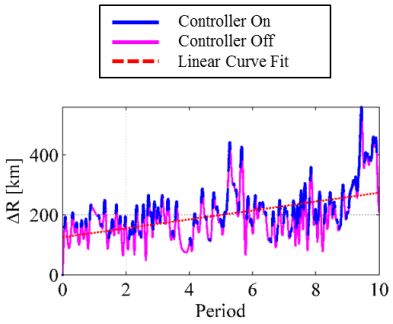


*(d) Magnitude of the Position Error Vector*

*Figure 5.13. Orbital Station-Keeping for the Nominal $L_1$ Halo Orbit Using the Discrete-time MHSP Controller ($\Delta t_k$ = 48 hours)*

where the spacecraft is thrusting and magenta lines indicate regions where the controller is off as the mission design constraints are not satisfied. Based on table 5.4 and figure 5.14, although the discrete-time controller is not able to indefinitely maintain the spacecraft in the vicinity of the orbit, it does, however, prolong the divergence time of the spacecraft by approximately 76%. These results are also in agreement with the linear stability analysis in figure 5.11, which indicates that the controlled trajectory under the discrete-time MHSP controller with $\Delta t_k$ equal to 3 weeks, is able to improve the stability of the nominal orbit by decreasing the value of the orbit's positive Poincare exponent.

*Table 5.4. Station-Keeping Performance of the Discrete-time MHSP controller with $\Delta t_k$ = 3 weeks*

| | $\Delta \bar{V}_T$ [m/s] | Average Divergence Time | |
|---|---|---|---|
| | | [revs] | [months] |
| Controlled Motion ($\Delta t_k$ = 3 weeks) | 147.9052 | 1.772 | 10.5090 |
| Uncontrolled Motion | - | 1.0061 | 5.9621 |

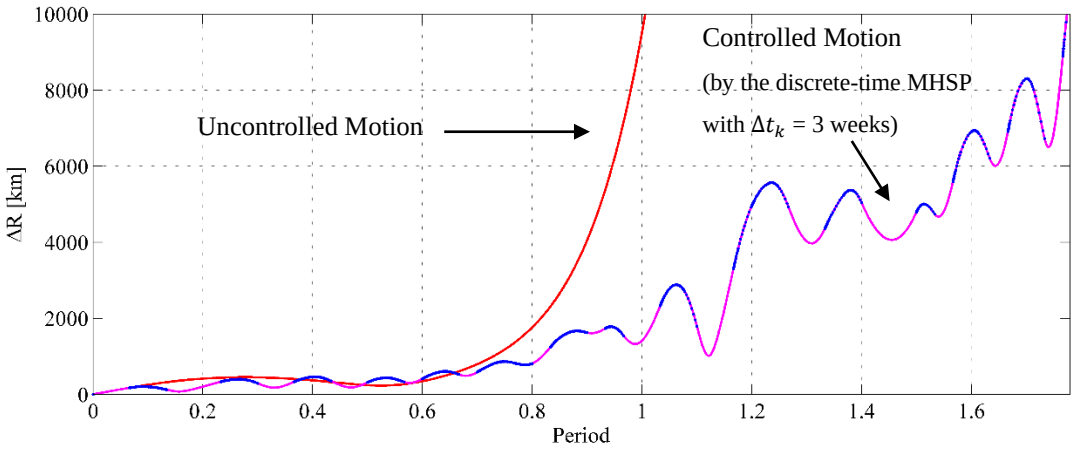


*Figure 5.14. Uncontrolled vs Controlled Position Error Vector Using the Discrete-time MHSP Controller with $\Delta t_k$ = 3 weeks*

# 6. SUMMARY AND RECOMMENDATIONS

## 6.1. Summary

In this investigation, orbital maintenance strategies for unstable libration point orbits are examined under the influence of real-world mission design constraints and operation errors. The control strategies studied in this investigation exploit the natural dynamical characteristics of the phase space surrounding the nominal orbit in the CR3BP in order to maintain the spacecraft in the vicinity of the desired nominal trajectory. In this study, two control strategies are studied and further developed: the impulsive Floquet Mode (FM) controller and the continuous Hamiltonian Structure-Preserving (HSP) controller. The FM controller is modified to accommodate feasible maneuver directions that are constrained to a plane or a line. This controller is shown to be applicable for orbital station-keeping of spin stabilized spacecraft that are only equipped with either tangential thrusters or axial thrusters. The continuous HSP controller, originally designed for planar trajectories, is extended for application to three-dimensional libration point orbits with hyperbolic instability. The HSP controller is then discretized to account for the minimum time required to obtain accurate post-burn orbit determination data, and/or the minimum time requirement for scientific operations. Both controllers, the FM controller and HSP controller, are applied to an unstable $L_1$ Halo orbit in the Sun-Earth/Moon system and the performances of these controllers are examined for 10 orbital periods (approximately 5 years), under the impacts of the spacecraft's operation errors and mission design constraints. The operation errors used in this analysis include orbit injection error, orbit tracking error, and maneuver execution error. The mission design constraints incorporated in this study include the minimum time constraint for orbit determination and/or scientific operations, the minimum allowable maneuver magnitude, and a constraint that only

implements corrective maneuvers if the magnitude of spacecraft's position error vector is increasing between two successive orbit tracking intervals. The main conclusions of this investigation are as follow:

(i) The FM controller, augmented with feasible maneuver direction constraints, and the Modified HSP (MHSP) controller are capable of successfully improving the stability of an unstable libration point orbit.

(ii) This work emphasizes the importance of incorporation of mission design constraints in station-keeping simulation algorithms, which has led to fundamental modifications to the design of the original controllers studied in this investigation.

(iii) Each of the controllers presented in this investigating, offers unique mission capabilities that is applicable to a specific flight hardware.

## 6.2. Recommendations for Future Work

Orbital maintenance control strategies developed in this research investigation provide groundwork for next generation of spacecraft control systems to accommodate increasingly complex space missions. Potential areas for future research development are as follows:

(i) Higher fidelity force models may be applied to the simulation algorithm. In this investigation, the orbital maintenance control strategies are simulated under the assumptions of the CR3BP. This simplified force model provides useful insights into the performance of the control strategies; however, the spacecraft's motion is not only subjected to the forces modeled by the CR3BP. It is of interest to examine the controllers' performance under additional perturbations such as the solar radiation pressure and additional attracting bodies.

(ii) In this study, the MHSP controller is proposed for libration point orbits with hyperbolic instability. Such orbits consist of one stable subspace, one unstable subspace, and four center subspaces. It may be of interest to extend this controller for other types of libration point orbits.

(iii) Methods to optimize the station-keeping fuel consumption are of interest. The two control strategies employed in this investigation result in encouraging low fuel consumptions, although no claim can be made that the results are optimal. Previous studies by Keeter [15] suggest that the location of corrective maneuvers on the nominal orbit and the timing between them impact the station-keeping fuel cost. For future studies, it may be of interest to investigate optimal timing and orbital locations to implement maneuvers in order to minimize station-keeping fuel consumption. In the MHSP controller the choice of the control gains also has an impact on the fuel cost. Optimization methods may be investigated to choose an optimal set of control gains.

# APPENDICES

## A. Trajectory Deviation in FM and MHSP Control Strategy

Results from chapters 4 and 5 showed that the motion of the spacecraft, controlled by the FM controller and the MHSP controller, undergoes a deviation from the nominal trajectory. To better understand the underlying reasons for this deviation, the station-keeping performance for each controller is examined under the following four scenarios:

*Table A.1. Simulation Scenarios for the FM and MHSP controllers*

| | | Scenario (1) | Scenario (2) | Scenario (3) | Scenario (4) |
|---|---|---|---|---|---|
| Operation Errors | Orbit injection error: (1-σ error of 1 km and 1 cm/s) | ✓ | ✓ | – | ✓ |
| | Orbit tracking error: (1-σ error of 1 km and 1 cm/s) | – | ✓ | – | ✓ |
| | Maneuver execution error: (1-σ error of %1) | – | ✓ | – | ✓ |
| Mission Design Constraints | Minimum Thrust Level: (FM: 0.025 m/s, MHSP: 0.3 mN) | – | – | ✓ | ✓ |
| | $\Delta t_{min}$: (FM: 3 weeks, MHSP: 1 hour) | – | – | ✓ | ✓ |
| | Controller Off: (if magnitude of position error vector is decreasing) | – | – | ✓ | ✓ |

In scenario (1), station-keeping simulations are propagated with only an initial orbit injection error. In scenario (2), all operation errors all included in the trails, but no mission design constraints are included. In scenario (3), only mission design constraints are included. Lastly, in scenario (4), all operation errors and mission design constraints are included in the trails. To assess the station-keeping performance in each scenario, the average linear divergence rate over 10 revolutions around the nominal orbit, as well as the average divergence time is evaluated. These measurements are averaged over a 300-trail Monte Carlo simulation. As defined in chapter 5, the divergence time is defined as the time

that the magnitude of the position error vector of the spacecraft relative to the nominal orbit exceeds 10,000 km.

## A.I. Trajectory Deviation under FM Controller

To better understand the position deviation of a spacecraft controlled by the FM control law, the station-keeping performance for the FM controller is assessed under the four scenarios given in table A.1. The FM controller used for this analysis is consistence with equation (4.7) in which the maneuvers are constrained to a plane fixed in the rotating frame. Similar results should hold for the FM controller with a line constraint. Table A.2 summarizes the station-keeping results, presented in terms of the average linear divergence rate for 10 revolutions around the nominal orbit, as well as the average divergence time.

*Table A.2. Station-keeping Performance for the FM Controller*

| | Scenario (1) | Scenario (2) | Scenario (3) | Scenario (4) |
|---|---|---|---|---|
| Average Linear Divergence Rate [km/rev] (divergence rate over 10 revolutions) | ~ 0 | +0.0167 | +0.0093 | +0.0219 |
| Average Divergence Time [rev] | >100 | 56.7182 | 83.6471 | 47.9146 |

The results from scenario (1) shows no deviation from the nominal orbit as the average linear divergence rate is approximately zero within numerical tolerance and the spacecraft stays in the vicinity of the nominal trajectory for more than 100 periods. In scenario (2), the addition of operation errors appears to cause the spacecraft to deviate with a positive rate of 0.0167 km/rev, and the divergence time in this case is about 56.7 revolutions around the nominal orbit. Scenario (3) indicates that incorporation of mission design constraints also results in position deviation. A comparison between scenario (2) and scenario (3) shows that incorporation of operation errors affects the position deviation more adversely than incorporation of mission design constraints. Lastly, scenario (4) shows that the

combination of both operation errors and mission design constraints will cause the spacecraft to diverge more rapidly when compared to scenarios (2) and (3).

In [15], Keeter suggested that the reason for such divergence is because the position deviations are measured based on an isochronous correspondence, and the deviation could merely represent a shift along the nominal orbit. To assess this effect further, station-keeping results are analyzed by examining the Poincare map of the controlled motion for a one-sided hypersurface fixed in the $\hat{x} - \hat{y}$ plane. Such Poincare map is defined by intersection of the controlled motion with the hypersurface when $z$ component of the flow changes from positive to negative. The pattern of the return points on this map will contain clues on the behavior of the controlled motion in the non-linear dynamics. For instance, if all the return points coincide at exactly one point on the map, this indicates that the controlled motion is a periodic trajectory. If the return points form a closed curve on the map, this is an indication that the controlled motion is quasi-periodic. Lastly, if they from an outward spiral pattern, this is an indication that the controlled motion is unstable and is deviation from the nominal orbit. The benefit of analyzing Poincare maps is that the relative controlled motion is no longer measured based on an isochronous correspondence.

Figures A.1 and A.3 are the representative Poincare maps generated for scenarios (1) and (4). Figures A.2 and A.4 are the corresponding position deviation history for figures A.1 and A.3, respectively. The Poincare map in figure A.1 is propagate for 100 revolutions of the nominal orbit, and it indicates a quasi-periodic controlled trajectory as the return points form a closed curve on the map. On the other hand, the Poincare map in figure A.3 shows that the return points are spiraling outward, which indicates that the spacecraft is in fact deviating from the nominal orbit.

Consequently, a spacecraft controlled by the FM controller may not stay indefinitely around the nominal orbit due to the incorporation of operation errors and mission design constraints. Nevertheless, the FM controller is able to maintain the spacecraft in the vicinity of the nominal orbit over a short time span of about 10 revolutions, which is still an acceptable duration for the majority of mission applications.

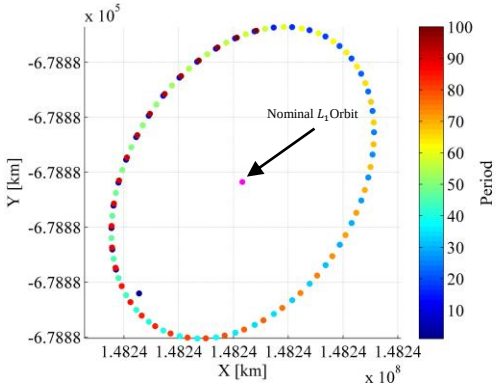


*Figure A.1. Poincare Map (X-Y Hyperplane) for the FM Controller (Scenario (1))*

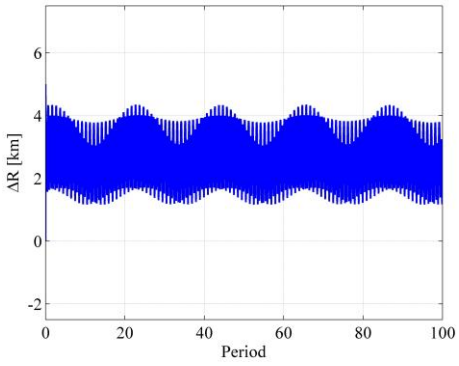


*Figure A.2. Spacecraft's Position Deviation with respect to the Nominal Orbit for the FM Controller (Scenario (1))*

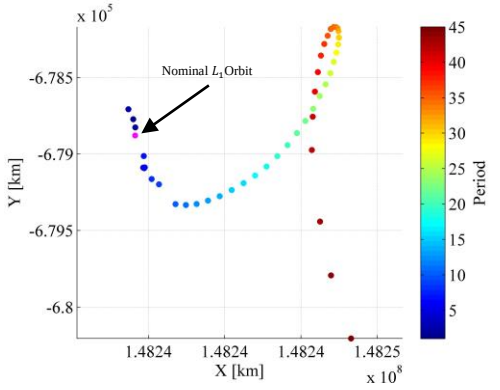


*Figure A.3. Poincare Map (X-Y Hyperplane) for the FM Controller (Scenario (4))*

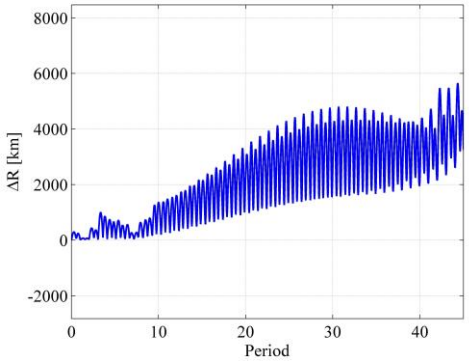


*Figure A.4. Spacecraft's Position Deviation with respect to the Nominal Orbit for the FM Controller (Scenario (4))*

## A.II. Trajectory Deviation under MHSP Controller

The station-keeping performance of the MSHP controller is examined under the four scenarios given in table A.1. For this analysis, a discrete-time MSHP controller with a discretization step size, $\Delta t_k$, equal to 1 hour is used. Table A.3 summarizes the station-keeping results, presented in terms of the average linear divergence rate for 10 revolutions around the nominal orbit, as well as the average divergence time.

*Table A.3. Station-keeping Performance for the MHSP Controller*

| | Scenario (1) | Scenario (2) | Scenario (3) | Scenario (4) |
|---|---|---|---|---|
| Average Linear Divergence Rate [km/rev] (divergence rate over 10 revolutions) | +0.0040 | +1.7125 | +0.1581 | +2.5991 |
| Average Divergence Time [rev] | 95.5121 | 44.3710 | 76.7112 | 24.6800 |

The results from scenario (1) shows that the spacecraft undergoes a gradual divergence with a small average divergence rate of 0.004 km/rev, measured over 10 revolutions of the nominal orbit. The spacecraft will eventually escape the vicinity of the orbit after 95.5 revolutions. This divergence is most likely due to the fact that the MHSP controller aims to achieve local bounded stability in the linearized dynamics, which does not guarantee bounded stability in the non-linear dynamics. As in the FM controller, when operation errors and mission design constraints are included in the simulation, the spacecraft will diverge more rapidly than in scenario (1). Comparison between scenarios (2) and (3) also suggests that incorporation of operation errors results in a higher divergence rate than the incorporation of mission design constraints. Figures A.5 and A.7 are the representative Poincare maps generated for scenarios (1) and (4). Figures A.6 and A.8 are the corresponding position deviation history for figures A.1 and A.3, respectively. These plots show that a spacecraft controlled by the MHSP controller will eventually diverge from the vicinity of the nominal orbit, and the divergence rate becomes faster when operation errors and mission design constraint are included in the simulation.

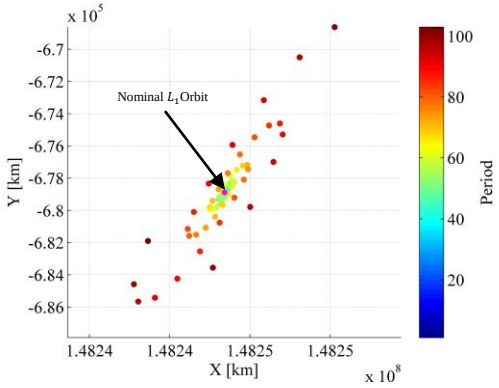


*Figure A.5. Poincare Map (X-Y Hyperplane) for the MHSP Controller (Scenario (1))*

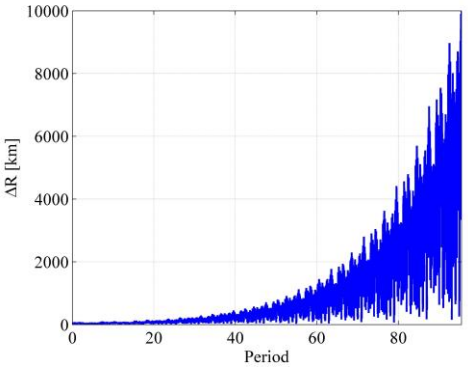


*Figure A.6. Spacecraft's Position Deviation with respect to the Nominal Orbit for the MHSP Controller (Scenario (1))*

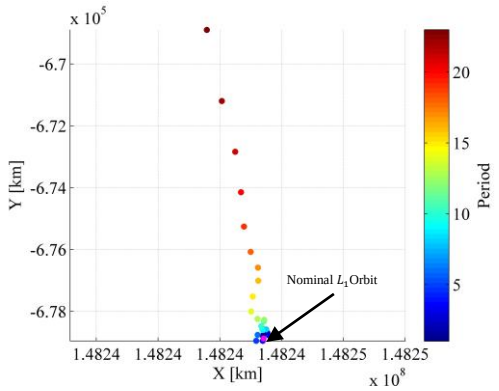


*Figure A.7. Poincare Map (X-Y Hyperplane) for the MHSP Controller (Scenario (4))*

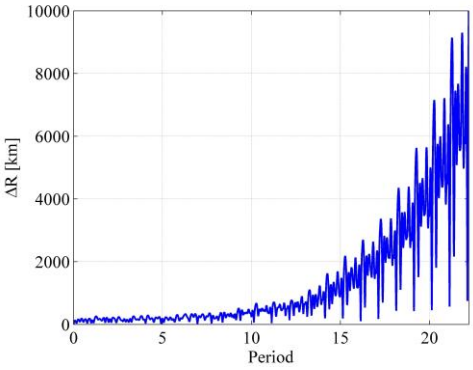


*Figure A.8. Spacecraft's Position Deviation with respect to the Nominal Orbit for the MHSP Controller (Scenario (4))*

## B. Effect of MHSP Control Strategy on the Hamiltonian

By definition, a Hamiltonian system is the set of $2n$ ordinary differential equations written as,

$$\dot{\vec{Z}} = K\frac{\partial H}{\partial \vec{Z}} \tag{B.1}$$

Where equations in (B.1) are known as the Hamilton's equations of motion. $K = \begin{bmatrix} 0 & I_n \\ -I_n & 0 \end{bmatrix}$, and $H$ is the Hamiltonian of the dynamical system.

The CR3BP is a Hamiltonian system as the equations of motion of a spacecraft in this dynamical environment can be represented in the form of the Hamilton's equations of motion in (B.1). In this appendix, the derivation of the non-dimensional Hamilton's equations of motion in the CR3BP is presented. Then the effect of the MHSP controller on the Hamiltonian is examined.

The derivation of the non-dimensional Hamilton's equations of motion is as follows. First, the kinetic energy associated with the spacecraft is given by,

$$T = \frac{1}{2}\dot{\vec{\rho}}.\dot{\vec{\rho}} \tag{B.2}$$

Where $(\,.\,)$ operator is the dot product. The expression for $\dot{\vec{\rho}}$ is given in equation (2.15). By substituting the kinematic expression from (2.15) into (B.2), the kinetic energy of the spacecraft can be written in the following form,

$$T = \frac{1}{2}((\dot{x} - y)^2 + (\dot{y} + x)^2 + \dot{z}^2) \tag{B.3}$$

Next, the potential energy of a spacecraft in the CR3BP is expressed,

$$U = -\frac{1-\mu}{d_1} - \frac{\mu}{d_2} \tag{B.4}$$

Given the kinetic and the potential energy, the Lagrangian $L$ is defined as follows [25],

$$L = T - U \tag{B.5}$$

In a general sense, the Lagrangian can be expressed in terms of the generalized coordinate vectors $\vec{q}$ and $\dot{\vec{q}}$, which are defined as,

$$\vec{q} = (q_1, q_2, q_3)^T \equiv (x, y, z) \tag{B.6}$$

$$\dot{\vec{q}} = (\dot{q}_1, \dot{q}_2, \dot{q}_3)^T \equiv (\dot{x}, \dot{y}, \dot{z}) \tag{B.7}$$

By using (B.6) and (B.7), the Lagranginan in (B.5) can be written as,

$$L(\vec{q}, \dot{\vec{q}}) = \frac{1}{2}\left((\dot{q}_1 - q_2)^2 + (\dot{q}_2 + q_1)^2 + {\dot{q}_3}^2\right) + \frac{1-\mu}{d_1} + \frac{\mu}{d_2} \tag{B.8}$$

Next, a generalized momentum vector $\vec{p}$ is defined,

$$\vec{p} = (p_1, p_2, p_3)^T \tag{B.9}$$

Such that,

$$\vec{p} = \frac{\partial L}{\partial \dot{\vec{q}}} \tag{B.10}$$

By substituting the Lagrangian $L$ into (B.10), the following relationships between $p_i$, $q_i$, and $\dot{q}_1$ can be derived for the application in the CR3BP,

$$\dot{q}_1 = p_1 + q_2 \tag{B.11}$$

$$\dot{q}_2 = p_2 - q_1 \tag{B.12}$$

$$\dot{q}_3 = p_3 \tag{B.13}$$

In general, the Hamiltonian $H$ is defined as [25],

$$H\left(\vec{q}, \dot{\vec{q}}, \tau^*\right) = \vec{p}.\dot{\vec{q}} - L\left(\vec{q}, \dot{\vec{q}}, \tau^*\right) \tag{B.14}$$

By applying equations (B.11)-(B.13), as well as substituting the expression for the Lagrangian from (B.8) into (B.14), the Hamiltonian in the CR3BP can be written as,

$$H(\vec{q}, \vec{p}) = \frac{1}{2}(p_1^2 + p_2^2 + p_3^2) + p_1 q_2 - p_2 q_1 - U(\vec{q}) \tag{B.15}$$

Therefore the Hamilton's equations of motion for the CR3BP are expressed as follows [25],

$$\dot{\vec{q}}^T = \frac{\partial H}{\partial \vec{p}} \tag{B.16}$$

$$\dot{\vec{p}}^T = -\frac{\partial H}{\partial \vec{q}} \tag{B.17}$$

The expression for the Hamiltonian in (B.15) is not an explicit function of time, and thus $H$ is time-invariant. This indicates that the CR3BP is an autonomous Hamiltonian system.

The effect of the MHSP controller on the Hamiltonian of the CR3BP can be examined by re-deriving the Hamiltonian from the equations of motion of the spacecraft augmented by the MHSP controller. From chapter 5, the expression for the continuous-time MHSP controller is given by,

$$\vec{u}(t) = \left(-\sigma^2 G[\vec{v}_1 \vec{v}_1^T + \vec{v}_2 \vec{v}_2^T] - \gamma^2 G_c\left[\vec{u}_c \vec{u}_c^T + \vec{\bar{u}}_c \vec{\bar{u}}_c^T\right]\right)\delta\vec{r} \tag{B.18}$$

$$\vec{u}(t) = T_c \delta \vec{r} \tag{B.19}$$

Where,

$$T_c = \begin{bmatrix} T_{11} & T_{12} & T_{13} \\ T_{21} & T_{22} & T_{23} \\ T_{31} & T_{32} & T_{33} \end{bmatrix} \tag{B.20}$$

From equation (B.18) it is clear that $T_c$ is a symmetric matrix, which means that,

$$T_{12} = T_{21} \tag{B.21}$$

$$T_{13} = T_{31} \tag{B.22}$$

$$T_{23} = T_{32} \tag{B.23}$$

It should be noted that the same results holds for the discrete-time MHSP controller.

By applying the MHSP controller to the equations of motion of a spacecraft in the CR3BP, as derived in chapter 2 in equations (2.26)-(2.28), the modified equations of motions can be written as follows,

$$\ddot{x} - 2\dot{y} = \frac{\partial U^*}{\partial x} + T_{11}\delta x + T_{12}\delta y + T_{13}\delta z \tag{B.24}$$

$$\ddot{y} + 2\dot{x} = \frac{\partial U^*}{\partial y} + T_{21}\delta x + T_{22}\delta y + T_{23}\delta z \tag{B.25}$$

$$\ddot{z} = \frac{\partial U^*}{\partial z} + T_{31}\delta x + T_{32}\delta y + T_{33}\delta z \tag{B.26}$$

Next, through the following coordinate transformation,

$$x = q_1 \tag{B.27}$$

$$y = q_2 \tag{B.28}$$

$$z = q_3 \tag{B.29}$$

$$\dot{x} = p_1 + q_2 \tag{B.30}$$

$$\dot{y} = p_2 - q_1 \tag{B.31}$$

$$\dot{z} = p_3 \tag{B.32}$$

the equations of motion in (B.24)-(B.26) can be expressed as 6 ordinary differential equations in terms of the generalized coordinate vectors ($\vec{p}, \vec{q}$),

$$\dot{q}_1 = p_1 + q_2 \tag{B.30}$$

$$\dot{q}_2 = p_2 - q_1 \tag{B.31}$$

$$\dot{q}_3 = p_3 \tag{B.32}$$

$$\dot{p}_1 = p_2 + \frac{\partial U^*}{\partial q_1} + T_{11}\delta q_1 + T_{12}\delta q_2 + T_{13}\delta q_3 \tag{B.33}$$

$$\dot{p}_2 = -p_1 + \frac{\partial U^*}{\partial q_2} + T_{21}\delta q_1 + T_{22}\delta q_2 + T_{23}\delta q_3 \tag{B.34}$$

$$\dot{p}_3 = p_3 + T_{31}\delta q_1 + T_{32}\delta q_2 + T_{33}\delta q_3 \tag{B.35}$$

In order for the equations of motion in (B.30)-(B.35) to represent a Hamiltonian system, a modified Hamiltonian $\widetilde{H}$ must exist such that,

$$\dot{\vec{q}}^T = \frac{\partial \widetilde{H}}{\partial \vec{p}} \tag{B.36}$$

$$\dot{\vec{p}}^T = -\frac{\partial \widetilde{H}}{\partial \vec{q}} \tag{B.37}$$

By equating (B.30)-(B.35) with (B.36)-(B.37), the modified Hamiltonian $\widetilde{H}$ must satisfy the following conditions,

$$\frac{\partial \widetilde{H}}{\partial p_1} = p_1 + q_2 \tag{B.38}$$

$$\frac{\partial \widetilde{H}}{\partial p_2} = p_2 - q_1 \tag{B.39}$$

$$\frac{\partial \widetilde{H}}{\partial p_3} = p_3 \tag{B.40}$$

$$\frac{\partial \widetilde{H}}{\partial q_1} = -p_2 - \frac{\partial U^*}{\partial q_1} - T_{11}\delta q_1 - T_{12}\delta q_2 - T_{13}\delta q_3 \tag{B.41}$$

$$\frac{\partial \widetilde{H}}{\partial q_2} = p_1 - \frac{\partial U^*}{\partial q_2} - T_{21}\delta q_1 - T_{22}\delta q_2 - T_{23}\delta q_3 \tag{B.42}$$

$$\frac{\partial \widetilde{H}}{\partial q_3} = -p_3 - T_{31}\delta q_1 - T_{32}\delta q_2 - T_{33}\delta q_3 \tag{B.43}$$

After some algebra, it is trivial to show that in order for $\widetilde{H}$ to exist the following three conditions must hold,

$$T_{12} = T_{21} \tag{B.44}$$

$$T_{13} = T_{31} \tag{B.45}$$

$$T_{23} = T_{32} \tag{B.46}$$

These three conditions are automatically satisfied by the MHSP controller since $T_c$ is a symmetric matrix. The modified Hamiltonian $\widetilde{H}$ is derived from equations (B.38)-(B.43) and is equal to,

$$\widetilde{H}\,(\vec{q},\vec{p}) = \frac{1}{2}(p_1^2 + p_2^2 + p_3^2) + p_1 q_2 - p_2 q_1 - U(\vec{q}) - \frac{1}{2}\delta\vec{q}T_c\delta\vec{q} \tag{B.47}$$

Note that $\widetilde{H}$ is not an explicit function of time. Therefore the modified dynamics by the MHSP controllers remains an autonomous and Hamiltonian system as the CR3BP. Hence it is called a Hamiltonian Structure-Preserving Controller.

## C. MHSP Control Strategy to Stabilize Hyperbolic Periodic Systems

In chapter 5 the Modified Hamiltonian Structure-Preserving (MHSP) controller is proposed which aims to place the roots of the characteristic polynomial for a three-dimensional hyperbolic periodic system on the imaginary axis. Three conditions are derived for the coefficients of the characteristic polynomial in (5.21) to ensure that the roots are purely imaginary. These three conditions are presented below and must be satisfied by the MHSP controller,

$$\tilde{b}(g, g_c, t) = 4 - \widetilde{U}^*_{xx} - \widetilde{U}^*_{yy} - \widetilde{U}^*_{zz} > 0 \tag{C.1}$$

$$\tilde{d}(g, g_c, t) = |\widetilde{U}^*_{RR}| > 0 \tag{C.2}$$

$$\begin{aligned} \tilde{b}\tilde{c} - \tilde{d}(g, g, t) = &\left(4 - \widetilde{U}^*_{xx} - \widetilde{U}^*_{yy} - \widetilde{U}^*_{zz}\right) \times \ldots \\ &\left(-\widetilde{U}^{*2}_{xy} - \widetilde{U}^{*2}_{xz} + \widetilde{U}^*_{xx}\widetilde{U}^*_{yy} - \widetilde{U}^{*2}_{yz} - 4\widetilde{U}^*_{zz} + \widetilde{U}^*_{xx}\widetilde{U}^*_{zz} + \widetilde{U}^*_{yy}\widetilde{U}^*_{zz}\right) \\ &- |\widetilde{U}^*_{RR}| > 0 \end{aligned} \tag{C.3}$$

Where $\widetilde{U}^*{}_{RR} = U^*_{RR} - \sigma^2 g[\vec{v}_u\vec{v}_u^T + \vec{v}_s\vec{v}_s^T] - \gamma^2 g_c\left[\vec{v}_c\vec{v}_c^T + \vec{\bar{v}}_c\vec{\bar{v}}_c^T\right] = \begin{bmatrix} \widetilde{U}^*_{xx} & \widetilde{U}^*_{xy} & \widetilde{U}^*{}_{xz} \\ \widetilde{U}^*_{xy} & \widetilde{U}^*_{yy} & \widetilde{U}^*{}_{yz} \\ \widetilde{U}^*_{xz} & \widetilde{U}^*_{yz} & \widetilde{U}^*_{zz} \end{bmatrix}$.

Without loss of generality, the position component eigenvectors $\vec{v}_u$, $\vec{v}_s$, and $\vec{v}_c$ can be written as the following unit vectors,

$$\vec{v}_u = (1/\sqrt{1 + v_{u1}^2 + v_{u2}^2}) \begin{bmatrix} 1 \\ v_{u1} \\ v_{u2} \end{bmatrix} \tag{C.4}$$

$$\vec{v}_s = (1/\sqrt{1 + v_{s1}^2 + v_{s2}^2}) \begin{bmatrix} 1 \\ v_{s1} \\ v_{s2} \end{bmatrix} \tag{C.5}$$

$$\vec{v}_c = (1/\sqrt{1 + v_{c1}\overline{v_{c1}} + v_{c2}\overline{v_{c2}}}) \begin{bmatrix} 1 \\ v_{c1} \\ v_{c2} \end{bmatrix}; \tag{C.6}$$

Where $v_{c1}$ and $v_{c2}$ are complex numbers written as,

$$v_{c1} = a_{c1} + ib_{c1} \tag{C.7}$$

$$v_{c2} = a_{c2} + ib_{c2} \tag{C.8}$$

Next, equation (C.1) can be expanded as a polynomial function of $g$ and $g_c$ as follows,

$$\tilde{b}(g, g_c, t) = 2g + 2g_c - \left(U_{xx}^* + U_{yy}^* + U_{zz}^* - 4\right) \tag{C.9}$$

From equation (C.9) it is clear that for large enough control gains $g$ and $g_c$, $\tilde{b}$ will be positive. In order for equation (C.9) to be always positive, the following conditions must hold for $g$ and $g_c$,

$$g + g_c > \frac{\left(U_{xx}^* + U_{yy}^* + U_{zz}^* - 4\right)}{2} \tag{C.10}$$

Next, equation (C.2) is also expanded as a polynomial function of $g$ and $g_c$ as follows,

$$\begin{aligned} \tilde{d}(g, g_c, t) = {} & g^3\left(\alpha_{3c0}(t)\right) + g_c^3\left(\alpha_{0c3}(t)\right) + \cdots \\ & g g_c^2\left(\alpha_{1c2}(t)\right) + \cdots \\ & g^2 g_c(\alpha_{2c1}(t)) + \cdots \\ & g_c g(\alpha_{1c1}(t)) + g(\alpha_{1c0}(t)) + \cdots \\ & g_c(\alpha_{0c1}(t)) + \alpha_{0c0}(t) \end{aligned} \tag{C.11}$$

In equation (C.11), the coefficients $\alpha_{icj}$ are functions of the time varying elements of $\widetilde{U}_{RR}^*$. Additionally, $\alpha_{0c3}(t)$ and $\alpha_{1c2}(t)$ are,

$$\alpha_{0c3}(t) = 0 \tag{C.12}$$

$$\alpha_{1c2}(\mathrm{t}) = \frac{\left(a_{c1}b_{c2} - a_{c2}b_{c1} - b_{c2}v_{11} + b_{c1}v_{12}\right)^2}{\left|\left|\vec{v}_c\right|\right|^4\left|\left|\vec{v}_u\right|\right|^2} + \cdots \quad \text{(C.13)}$$

$$\frac{\left(a_{c1}b_{c2} - a_{c2}b_{c1} - b_{c2}v_{21} + b_{c1}v_{22}\right)^2}{\left|\left|\vec{v}_c\right|\right|^4\left|\left|\vec{v}_u\right|\right|^2}$$

Note that in (C.13), $\alpha_{1c2}(\mathrm{t})$, which is the coefficient of $gg_c^2$ term, is always positive. Therefore, to ensure that $\tilde{d}$ is always greater than zero, $g$ and $g_c$ must be chosen such that,

$$gg_c^2\left(\alpha_{1c2}(t)\right) > |g^3\left(\alpha_{3c0}(t)\right) + g^2 g_c(\alpha_{2c1}(t)) + \ldots \quad \text{(C.14)}$$
$$g_c g\left(\alpha_{1c1}(t)\right) + g\left(\alpha_{1c0}(t)\right) + \cdots$$
$$g_c(\alpha_{0c1}(t)) + \alpha_{0c0}(t)|$$

Furthermore, from equation (C.14) a sufficient condition can be written for the minimum value of $g_c$ as a function of $g$ to ensure that $\tilde{d}$ is always positive,

$$g_c > \left(\frac{|\alpha_{3c0}| + |\alpha_{2c1}(t)| + |\alpha_{1c1}(t)| + |\alpha_{1c0}(t)| + |\alpha_{0c1}(t)| + |\alpha_{0c0}(t)|)}{\alpha_{1c2}(t)}\right)g \quad \text{(C.15)}$$

Next, equation (C.3) is expanded as a polynomial function of $g$ and $g_c$ as follows,

$$\tilde{b}\tilde{c} - \tilde{d}(g, g, t) = g^3\left(\beta_{3c0}(t)\right) + g_c^3\left(\beta_{0c3}(t)\right) + \cdots \quad \text{(C.16)}$$
$$gg_c^2\left(\beta_{1c2}(t)\right) + \cdots$$
$$g^2 g_c(\beta_{2c1}(t)) + \cdots$$
$$g_c g(\beta_{1c1}(t)) + g(\beta_{1c0}(t)) + \cdots$$
$$g_c(\beta_{0c1}(t)) + \beta_{0c0}(t)$$

In equation (C.16), the coefficients $\alpha_{icj}$ are functions of the time varying elements of $\widetilde{U}_{RR}^*$. Additionally, $\beta_{0c3}(t)$ is given by,

$$\beta_{0c3}(t) = \frac{4(a_{c1}b_{c2} + a_{c2}b_{c1})^2 + 4b_{c1}^2 + 4b_{c2}^2}{\left||u_c|\right|^6} \tag{C.17}$$

Note that in (C.17), $\beta_{0c3}(t)$, which is the coefficient of $g_c^3$ term, is always positive. Therefore, to ensure that $\tilde{b}\tilde{c} - \tilde{d}$ is always greater than zero, $g$ and $g_c$ must be chosen such that,

$$\begin{aligned} g_c^3\left(\beta_{0c3}(t)\right) > |g^3\left(\beta_{3c0}(t)\right) + g g_c^2\left(\beta_{1c2}(t)\right) + \ldots \\ g^2 G_c\left(\beta_{2c1}(t)\right) + G_c G\left(\beta_{1c1}(t)\right) + \ldots \\ g(\beta_{1c0}(t)) + g_c(\beta_{0c1}(t)) + \beta_{0c0}(t)| \end{aligned} \tag{C.18}$$

From equation (C.18) a sufficient condition can be written for the minimum value of $g_c$ as a function of $g$ to ensure that $\tilde{b}\tilde{c} - \tilde{d}$ is always positive,

$$g_c > \left(\frac{|\beta_{3c0}(t)| + |\beta_{2c1}(t)| + |\beta_{2c1}(t)| + |\beta_{1c1}(t)| + |\beta_{1c0}(t)| + |\beta_{0c1}(t)| + |\beta_{0c0}(t)|)}{\beta_{0c3}(t)}\right) g \tag{C.16}$$

## D. Application of FM and MHSP controllers to NRO

In this section, the FM controller and the discrete-time MHSP controller are applied for station-keeping around a Near Rectilinear Orbit (NRO) in the Earth-Moon system. NROs are relatively stable liberation point orbits as they generally possess small unstable Poincare exponents. In recent years, these trajectories are becoming attractive candidates for variety of space applications around the Moon [30]. Nevertheless, due to the existence of a positive Poincare exponent, an orbiting spacecraft will eventually diverge from the unstable NROs. Therefore, orbital station-keeping strategies must be implemented. In this section, an $L_2$ NRO in the Earth-Moon system is considered as a baseline for station-keeping. This particular NRO, shown in figure D.1, has an orbital period of about 7 days and a lunar periapsis of 2000 km.

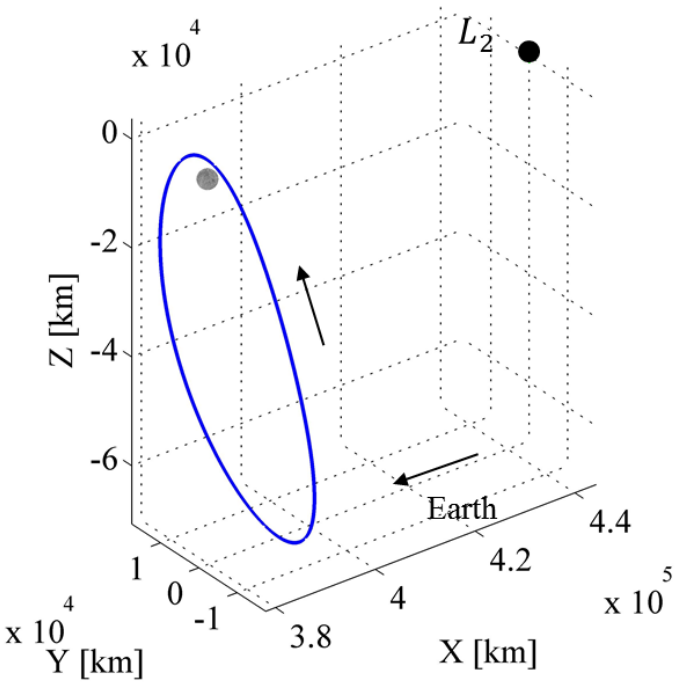


*Figure D.9. Nominal $L_2$ NRO*

## D.1. NRO Station-Keeping under FM controller

For demonstration purposes, the FM controller augmented with a plane constraint, as presented in equation (4.7), is applied for station-keeping of a spin stabilized spacecraft that is only equipped with tangential thrusters. For this analysis, it is assumed that the spin axis is fixed in the rotating frame and the spacecraft has a similar configuration as in figure 4.2. Table D.1 summarizes mission specifications, design constraints, and operation errors that are used in this analysis.

*Table D.4. Mission Specifications, Design Constraints, and Operation Errors for the FM Controller*

| | |
|---|---|
| Mission Specifications | - Nominal orbit: $L_2$ southern NRO in Earth-Moon system<br>- Mission duration: 10 revolutions (~ 2 months)<br>- Spin axis: fixed in the rotating |
| Mission Design Constraints | - Minimum $\|\Delta\vec{V}\|$: 0.025 m/s<br>- $\Delta t_{min}$: 48 hours<br>- No corrective maneuver if magnitude of position error vector is decreasing |
| Operation Errors | - Orbit injection and tracking errors: 1-σ errors of 1 km and 1 cm/s<br>- Maneuver execution error: 1-σ error of %1 |

Figure D.2 shows representative simulation plots for station-keeping around the nominal NRO using the FM controller. According to plots D.2.(a) and D.2.(b), the FM controller is able to maintain the motion of the spacecraft in the vicinity of the nominal orbit for the duration of the simulation. It is interesting to see that all the corrective maneuvers are implemented near the lunar periapsis. This is due to the fact that over each lunar passage the spacecraft undergoes sudden position fluctuation from the nominal orbit. The control algorithm is able to detect these fluctuations and implement a corrective maneuver when necessary. Based on plot D.2.(c), all the directions of corrective maneuvers

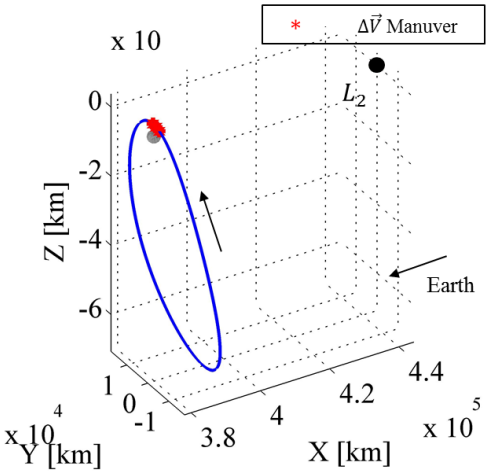


*(a) Controlled $L_2$ NRO Using the Impulsive FM Controller with a Plane Constraint on $\Delta\vec{V}$*

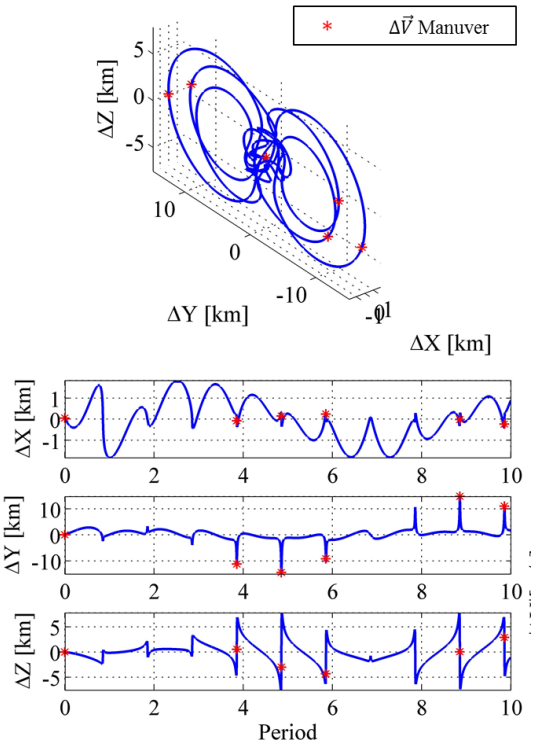


*(b) Motion Relative to the Reference $L_2$ NRO*

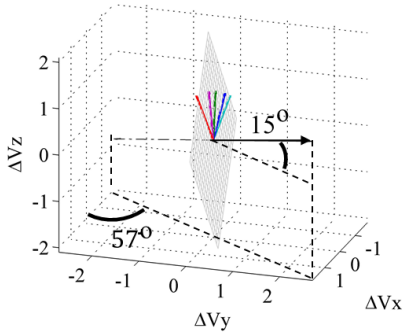


*(c) Directions of $\Delta\vec{V}$ Maneuvers*

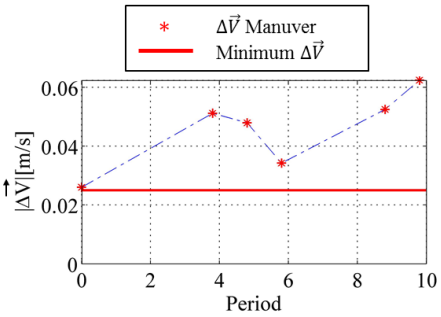


*(d) Magnitude of $\Delta\vec{V}$ Maneuvers*

*Figure D.10. Orbital Station-Keeping for the Nominal $L_2$ NRO Using the FM controller for a Spin Stabilized Spacecraft with Tangential Thrusters and a Fixed Spin Axis in the Rotating Frame*

are constrained to the plane perpendicular to the spacecraft's spin axis. Moreover, plot D.2.(d) shows that the magnitudes of all the corrective maneuvers satisfy the minimum allowable $\Delta\vec{V}$ magnitude. Table D.2 summarizes Monte Carlo simulations results. This table includes the average station-keeping cost over 10 orbital periods, the average cost over month, as well as the linear divergence rate from the nominal NRO.

*Table D.5. Station-Keeping Performance for the FM Controller around an $L_2$ NRO*

| Thrusters on-board | $\vec{V}_s$ fixed in | $\Delta\bar{V}_T$ for 10 revolutions [m/s] | $\Delta\bar{V}_T$/ month [m/s] | Average Linear Divergence Rate [km/rev] |
|---|---|---|---|---|
| Tangential | Rotating Frame | 2.1294 | 0.9549 | +0.1346 |

D.2. NRO Station-Keeping under Discrete-time MHSP controller

The discrete-time MSHP controller, developed in chapter 5, is applied for station-keeping around the nominal $L_2$ NRO. For demonstration purposes, the discretization step size is set to 48 hours. Table D.1 summarizes mission specifications, design constraints, and operation errors that are used in this analysis.

*Table D.6. Mission Specifications, Design Constraints, and Operation Errors for the Discrete-time MHSP Controller*

| | |
|---|---|
| Mission Specifications | - Nominal orbit: $L_2$ southern NRO in Earth-Moon system<br>- Mission duration: 10 revolutions (~ 2 months)<br>- Spin axis: fixed in the rotating |
| Mission Design Constraints | - Minimum Thrust: 0.3 mN<br>- $\Delta t_{min}$: 48 hours<br>- No corrective maneuver if magnitude of position error vector is decreasing |
| Operation Errors | - Orbit injection and tracking errors: 1-σ errors of 1 km and 1 cm/s<br>- Maneuver execution error: 1-σ error of %1 |

Figure D.3 shows representative simulation plots for station-keeping around the nominal NRO using the discreet-time MHSP controller. According to this figure, the controller is able to improve the stability of the nominal orbit as the divergence rate of the controlled motion is smaller than the uncontrolled motion. Plot D.3.(b) also shows that the controller is able to reduce the amplitude of the position fluctuations caused at lunar periapsis. Table D.2 summarizes Monte Carlo simulations results. This table includes the average station-keeping cost over 10 orbital periods, the average cost over month, as well as the linear divergence rate from the nominal NRO.

*Table D.7. Station-Keeping Performance for the Discrete-time MHSP Controller around an $L_2$ NRO*

| $\Delta\bar{V}_T$ for 10 revolutions [m/s] | $\Delta\bar{V}_T$/ month [m/s] | Average Linear Divergence Rate [km/rev] |
|---|---|---|
| 33.1009 | 14.8434 | +18.2891 |

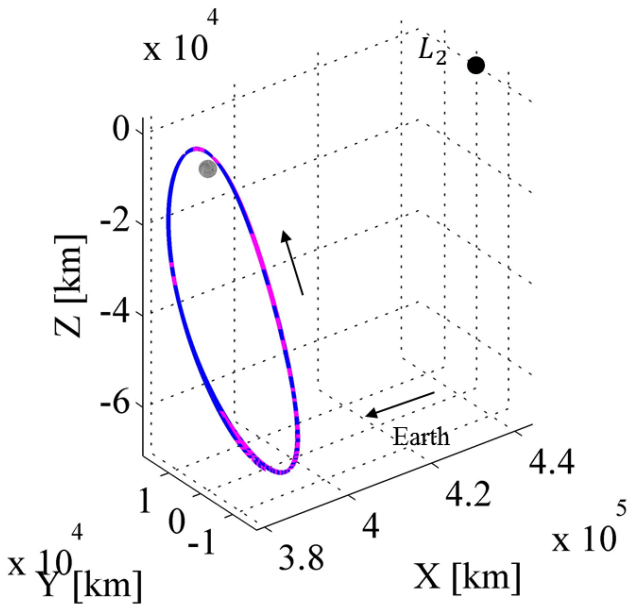


*(a) Controlled $L_2$ NRO Using the Discrete-time MHSP Controller*

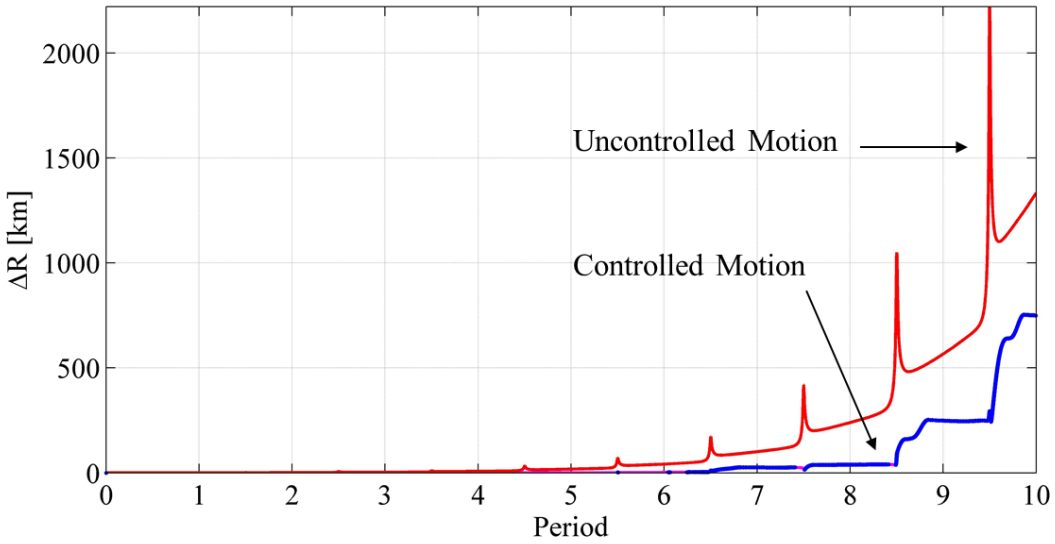


*(b) Position Deviation Relative to the Nominal Orbit*

*Figure D.11. Orbital Station-Keeping for the Nominal $L_2$ NRO Using the Discrete-time MHSP Controller ($\Delta t_k$ = 48 hours)*

# LIST OF REFERENCES

# LIST OF REFERENCES

[1] Farquhar, R.W., “The Flight of ISEE-3/ICE: Origins, Mission history, and a Legacy" Paper No. AIAA-1998-4464, AIAA/AAS Astrodynamics Specialist Conference and Exhibit, Boston, Massachusetts, August 10-12, 1998.

[2] Roberts, C.E. and Short, R., “Injection Contingency Recovery Strategies for Halo Orbit Transfer Trajectories," Paper No. AIAA-1996-3600, AIAA/AAS Astrodynamics Conference, San Diego, California, July 29-31, 1996.

[3] Sharer, P. and Harrington, T., “Trajectory optimization for the ACE Halo Orbit Mission," Paper No. AIAA-1996-3601, AIAA/AAS Astrodynamics Conference, San Diego, California, July 29-31, 1996.

[4] Lo, M.W., Williams, B.G., Bollman, W.E., Han, D., Hahn, Y., Bell, J.L., Hirst, E.A., Corwin, R.A., Hong, P.E., Howell, K.C., Barden, B.T., and Wilson, R.S., “Genesis Mission Design," Paper No. AIAA-1998-4468, AIAA/AAS Astrodynamics Specialist Conference and Exhibit, Boston, Massachusetts, August 10-12, 1998.

[5] Markley, F., Andrews, S., O'Donnell, J., and Ward, D., “The Microwave Anisotropy Probe (MAP) Mission," Paper No. AIAA-2002-4578, AIAA Guidance, Navigation, and Control Conference and Exhibit, Monterey, California, August 5-8, 2002.

[6] Mather, J., “James Webb Space Telescope," Paper No. AIAA-2004-5985, Space 2004 Conference and Exhibit, San Diego, California, September 28-30, 2004.

[7] Newton, I., "The Principia: The Mathematical Principles of Natural Philosophy" (1687). Berkeley, California: University of California Press, 1999. Translation by Cohen I.B. and Whitman A.

[8] Szebehely, V., "Theory of Orbits: The Restricted Problem of Three Bodies". New York: Academic Press, 1967.

[9] Jacobi, C.G.J., "Sur le Mouvement d'un Point etsur un casParticulier duProbleme des Trois Corps," ComptesRendus de l'Acadmie des Sciences de Paris,vol. 3, pp. 59-61, 1836.

[10] Howell, K.C. and Farquhar, R.W., “John Breakwell, The Restricted Problem, And Halo Orbits”, Acta Astronautica, Vol. 29, No. 6, pp. 485-488, 1993.

[11] Gomez, G., Llibre, J., Mart´ınez, R. and Sim´o, C., “Dynamics and mission design near Libration points Vol. I: Fundamentals: the case of collinear Libration points”, World Scientific Monograph Series in Mathematics, Vol. 2, 2001.

[12] Simo, C., G´omez, G., Llibre, J., Matinez, R. and Rodriguez, J., “On the optimal station keeping control of halo orbits”, Acta Astronautica, Vol. 15, pp. 391-397, 1987.

[13] Howell, K.C., Pernicka, H.J., “Stationkeeping method for Libration point trajectories”, Journal of Guidance, Control, and Dynamics, Vol. 16, pp. 115-159, 1993.

[14] Howell, K., and Gordon, S., "Orbit Determination Error Analysis and a Station-Keeping Strategy for Sun-Earth L1 Libration Point Orbits," Journal of the Astronautical Sciences, Vol. 42, No. 2, April-June 1994, pp. 207-228.

[15] Keeter, M., “Station-keeping strategies for Libration point orbits: target points and Floqu´et mode approaches”, Purdue University, MSc Thesis, August, 1994.

[16] Scheeres, D.J., Hsiao, F.-Y. and Vinh, N.X., “Stabilizing motion relative to an unstable orbit: applications to spacecraft formation flight”, Journal of Guidance, Control and Dynamics, Vol. 26, No. 1, pp. 62-73, Jan. 2003.

[17] Xu, M. and Xu, S., “Structure-preserving stabilization for Hamiltonian system and its applications in Solar Sail”, American Institute of Aeronautics and Astronautics, Vol. 32, No. 3, pp. 997-1004 , May-June 2009.

[18] Soldini, S., Colombo, C., Walker, S.J., "Comparison of Hamiltonian structure-preserving and Floquét mode station-keeping for Libration-point orbits." Paper No. AIAA-2014-4118, Proceedings of the AIAA/AAS Astrodynamics Specialist Conference, San Diego, California, August 4-7, 2014. American Institute of Aeronautics and Astronautics, 2014.

[19] Roberts, C., Case, C.S., Reagoso, J., "Lissajous Orbit Control for the Deep Space Climate Observatory Sun-Earth L1 Libration Point Mission" Paper No. AAS 15-611, American Institute of Aeronautics and Astronautics Conference, AIAA/AAS Astrodynamics Specialist Conference, Vail, CO, August 2015.

[20] Folta, D., Pavlak, T., Howell, K., Woodard, M., Woodfork, D., "Stationkeeping of Lissajous Trajectories in the Earth-Moon System with Applications to ARTEMIS" Paper No. AAS 10-113, 20th AAS/AIAA Space Flight Mechanics Meeting, San Diego, California, February 2010.

[21] Marchand, B.G., "Spacecraft Formation Keeping Near the Libration Points of the Sun-Earth/Moon System", Ph.D. thesis, Purdue University, 2004.

[22] Gordon, S.C., "Orbit Determination Error Analysis and Station-keeping for Libration Point Trajectories", Ph.D. thesis, Purdue University, 1991.

[23] Farquhar, R.W., "The Control and Use of Libration Point Satellites", PhD thesis, Stanford University, 1968.

[24] Howell, K.C., "Three-Dimensional, Periodic, 'Halo' Orbits," Celestial Mechanics, vol. 32, pp. 53–71, 1984.

[25] Lanczos, C., "The Variational Principles of Mechanics", Dover Publications, Inc., New York, 4th ed., 1970.

[26] Millard, L., "Control of Satellite Imaging Arrays in Multi-Body Regimes", Ph.D. thesis, Purdue University, 2008.

[27] Wiggins, S., "Introduction to Applied Nonlinear Dynamical Systems and Chaos", New York: Springer-Verlag, 1990.

[28] Haapala, A.F., “Trajectory Design in the Spatial Circular Restricted Three-Body Problem Exploiting Higher Dimensional Poincare Maps”, Ph.D. thesis, Purdue University, 2014.

[29] Perko, L., “Differential Equations of Dynamical Systems”, New York: Springer-Verlag, second Edition, 1996.

[30] Jesick, M., “Abort Options for Human Missions to Earth-Moon Halo Orbits”, Paper No. AAS 11-452, 23rd AAS/AIAA Space Flight Mechanics Meeting, Kauai, Hawaii, February 2013.